Dissertation

submitted to the

Combined Faculty of Mathematics, Engineering and Natural Sciences

of Heidelberg University, Germany

for the degree of

Doctor of Natural Sciences

Put forward by

Tim Dullweber

born in: Lohne (Oldenburg)

Oral examination: 30th April 2025

Feedback dynamics in mechanochemical matter

Referees: Dr. Anna Erzberger

Prof. Dr. Ulrich Schwarz

Feedback dynamics in mechanochemical matter

Referees: Dr. Anna Erzberger

Prof. Dr. Ulrich Schwarz

Abstract

Non-equilibrium microscopic processes can drive macroscopic shape changes in soft materials. Feedback arises when such shape changes alter the geometry constraining the microscopic dynamics. Although such feedback is common in living materials, which can actively change their chemical composition in response to environmental signals, the underlying theoretical principles, and the resulting dynamical phenomena are not well understood.

Motivated by biological cells exchanging shape-dependent signals at physical contacts, I investigated incompressible droplets adjusting their interfacial tensions in response to contact-dependent signals. I derived a minimal set of equations governing the macroscopic droplet states controlled by two dimensionless feedback parameters. I discovered that the droplet's adaptive wetting properties give rise to rich dynamical phenomena, including regimes of multistability, symmetry-breaking, excitability, and self-sustained shape oscillations. For some configurations, the topology of the arising phase-space structures is analogous to Hodgkin-Huxley type neuronal models, allowing me to identify parallels between adaptive wetting dynamics and signal processing in neurons.

Applying these theoretical results to experimental shape measurements from imaging data of zebrafish embryos, I found that the critical point arising from a shape multistability promotes the formation of boundaries between different developing tissues. Moreover, using fully data-derived contact-networks, I predicted cellular differentiation patterns driven by contact-dependent signaling in mechanosensory epithelia of zebrafish larvae.

Together, this thesis provides new paradigms for physical signal processing through shape adaptation in soft active materials, and uncovers novel modes of self-organisation in the collective dynamics of biological tissues.

Zusammenfassung

Mikroskopische Nichtgleichgewichtsprozesse können makroskopische Formänderungen in weichen Materialien hervorrufen. Rückkopplungen entstehen, wenn diese Formänderungen die Geometrie verändern, welche die Domäne der mikroskopischen Dynamiken definiert. In lebenden Materialien kommen solche Rückkopplung häufig vor. Biologische Zellen können beispielsweise auf Signale reagieren, indem sie ihre chemische Zusammensetzung aktiv anpassen. Dennoch sind die zugrundeliegenden theoretischen Prinzipien und die daraus resultierenden dynamischen Phänomene bislang unzureichend verstanden.

Motiviert durch biologische Zellen, die bei physischem Kontakt formabhängige Signale austauschen, untersuchte ich inkompressible Tröpfchen, deren Grenzflächenspannungen sich in Abhängigkeit von solchen kontaktvermittelten Signalen adaptiv verändern. Ich leitete einen minimalen Satz von Gleichungen ab, der die makroskopischen Zustände der Tröpfchen beschreibt und durch zwei Rückkopplungsparameter gesteuert wird. Die adaptive Benetzungsdynamik führt zu einer Vielfalt von dynamischen Phänomenen wie Multistabilität, Symmetriebruch und Formoszillationen. Ein Vergleich mit Hodgkin-Huxley-Modellen offenbart Parallelen zur Signalverarbeitung in Neuronen.

Durch Anwendung dieser Gleichungen auf experimentelle Daten von Zebrafischembryonen identifizierte ich, dass mechanochemische Multistabilität die Ausbildung von Gewebsgrenzen während der Embryonalentwicklung fördert. Zudem gelang mithilfe von datenbasierten Zell-Kontakt-Netzwerken die Vorhersage von Zelldifferenzierungsmustern in den mechanosensorischen Epithelien von Zebrafischen, die durch kontaktabhängige Signalgebung zustandekommen.

Diese Arbeit liefert somit neue Paradigmen für die physikalische Signalverarbeitung durch Formanpassung in weichen, aktiven Materialien, und offenbart bisher unbekannte Mechanismen der Selbstorganisation in biologischen Systemen.

Contents

List of Figures and Tables

Chapter 1

Introduction

Living matter is a class of typically soft materials that operate far from thermodynamic equilibrium [1]. Microscopic energy-consuming processes—including biomolecular production and degradation, active transport that drives spatially varying concentration fields, and the generation of active stresses—dynamically shape their material properties. Studying such far-from-equilibrium systems can uncover new physics, where material properties are not defined by thermodynamic equilibrium variables but by gradients, unbalanced kinetic rates, and energy dissipation [2].

Material properties characterize a system's response to external perturbations or stimuli, sometimes described as an input-output relation dictated by the material's intrinsic properties. For instance, a dielectric material responds to an applied electric field (input) with the induction of a dipole moment (output) depending on its electric susceptibility [3]. Near thermal equilibrium, response functions are linked to thermodynamic variables [4, 5]. However, in active materials, input-output relations depend on non-equilibrium properties and can be far more complex [2, 6, 7]. In living systems, where the output often determines a biological function, this process is commonly referred to as *signal processing*. For example, a biological tissue may respond to a chemical field with growth, morphogenetic changes, or the release of biochemical substances [8, 9]. Similarly, electrical fields can induce rhythmic contractions, collective migration, or differentiation into new cell types [10, 11, 12, 13].

Biological signal processing often relies on chemical interactions confined within organelles, cells, or tissues. Reaction-diffusion dynamics depend on the domain geometry and boundary conditions [14, 15, 16], making signal processing inherently geometry-dependent. When chemical reactions induce mechanical changes and deformations, a feedback loop emerges: shape changes in response to signals modify the space in which chemical interactions occur, which in turn influences further signal processing [17]. Such mechanochemical feedback can generate highly nonlinear dynamics with minimal degrees

of freedom.

A striking example is the contact-dependent Notch signaling pathway, where biochemical interactions of membrane-bound molecules across cell-cell interfaces trigger an internal cascade that ultimately alters cellular mechanical properties. These mechanical changes, in turn, regulate the number and geometry of cell-cell contacts, coupling mechanical and biochemical interactions in a self-organizing process. A prominent example are mechanosensory epithelia, where contact-dependent Notch signaling governs cell differentiation accompanied by active mechanical processes inducing shape changes and the global rearrangement of cells. Understanding this mechanochemical feedback is central to the study of tissue organization and developmental processes [17, 18, 19, 20, 21, 22, 23], and emergent properties in active soft matter [24, 25, 26, 27].

In this thesis, I develop a theoretical framework to study shape-dependent feedback dynamics in contact-dependent signaling. Drawing an analogy between cells and droplets, I theoretically examine how droplets can adjust their interfacial tension in response to contact-dependent signals. To provide the necessary background, I first introduce the physics of wetting, following [28]. In particular, I derive an expression for the contact area between interacting droplets, which is used throughout Chapter. 3 and 4. I then discuss efforts to engineer smart materials with adaptive wetting properties and I showcase how biological systems leverage the interplay of signaling and adaptive adhesion to form and maintain structures during development, regeneration, and homeostasis—focusing on examples presented in my published review [17]. Finally, Section 1.3 outlines the key objectives of this thesis in more detail.

1.1 Physics of capillarity and wetting

To this day, capillarity, the study of interfaces between liquids and other solid, fluid or gaseous phases, remains an active field of research [30, 31]. Capillary phenomena are abundant in many scientific disciplines like geo-, climate- or biophysics [32, 33, 34], and they play a crucial role for various industrial manufacturing processes [35, 36].

1.1.1 Laplace's theorem

Liquid interfaces are deformable and undergo shape changes minimizing the surface energy; yet, they can adopt extremely stable shapes when reaching an energy minimum [28]. For instance, oil droplets in water and soap bubbles form stable spheres—the minimal surface configuration given a fixed fluid volume. Liquid interfaces can be treated like

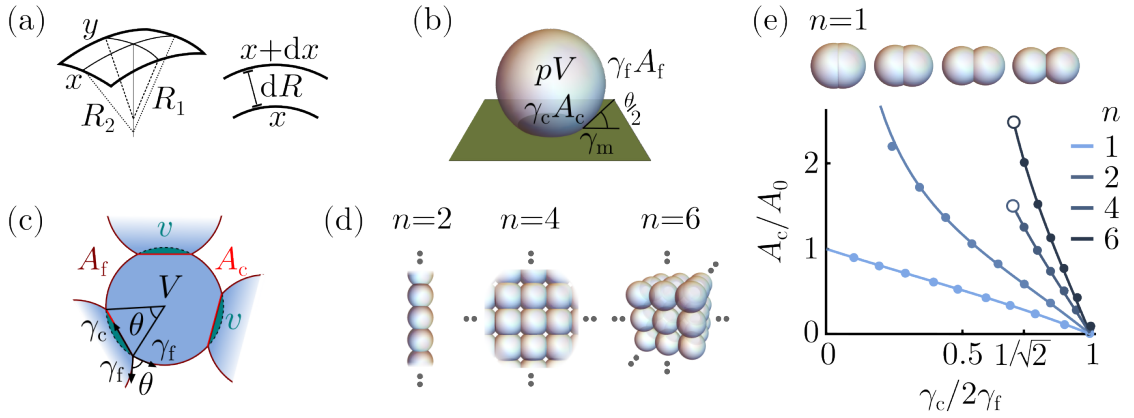

Figure 1.1. Physics of wetting. (a) Schematic of the isotropic expansion of a surface element with area xy and local radii of curvature R_1, R_2. (b) The equilibrium shape of an adhesive droplet—and the contact angle θ—are set by the balance between Laplace pressure p associated with volume V and surface tensions $\gamma_\mathrm{f}, \gamma_\mathrm{c}$ associated with the free and contact surface areas $A_\mathrm{f}, A_\mathrm{c}$, and the tension γ_m at the substrate/medium interface. (c) The balance of surface tensions at the contact and free surfaces defines the equilibrium contact angle θ [Eq. (1.4)] of interacting droplets in a fixed-topology configuration. (d) Droplet configurations for $n = \{2, 4, 6\}$. (e) Droplets with equal conserved volumes in configurations with n contacts and no triple or higher-order junctions form equilibrium configurations in which the total contact area per droplet depends on n and the tension ratio $\gamma_\mathrm{c}/2\gamma_\mathrm{f}$ [Eq. (1.7)] (points: numerical results [Appendix A], [29], empty circles: appearance of higher-order junctions, images for $\gamma_\mathrm{c}/2\gamma_\mathrm{f} = \{0.2, 0.4, 0.6, 0.8\}$).

membranes under a tension that opposes distortions [28]. In simple liquids, this tension arises from the difference in cohesive forces between molecules in the bulk and those exposed to the surface. The thermodynamic work $\delta W_\mathrm{A} = \gamma dA$ required to increase the surface by an amount dA is proportional to the surface tension $\gamma = \left.\dfrac{\partial F}{\partial A}\right|_{T,V,n}$, with F the free energy and T, V, n the constant temperature, volume, and particle number.

The overpressure in the interior of a droplet due to the surface tension, i.e. the pressure increase when traversing the fluid surface, is called the *Laplace pressure* p. At equilibrium, the Laplace pressure balances the surface tension. Consider a surface element of area $A = xy$ as shown in Fig. 1.1(a). The work to isotropically expand the surface element is $\delta W_\mathrm{A} = \gamma(xdy + ydx)$, and the corresponding volume work is $\delta W_\mathrm{V} = pdV = pxydR$, where dR is the change in the local radius of curvature. At equilibrium $\delta W_\mathrm{A} = W_\mathrm{V}$ and with $dx = \frac{x}{R_1}dR, dy = \frac{y}{R_2}dR$ follows Laplace's theorem

$$p = \gamma\left(\frac{1}{R_1} + \frac{1}{R_2}.\right). \tag{1.1}$$

It implies that interfaces, across which the ratio of pressure and surface tension is constant,

have a constant mean curvature $(1/R_1 + 1/R_2)/2$ at equilibrium. This argument neglects the gravitational acceleration g, which is valid depending on a droplet's size. Comparison of the Laplace pressure γ/l_κ and the hydrostatic pressure $\rho g l_\kappa$ at a depth l_κ for a liquid of density ρ defines the capillary length scale $l_\kappa = \sqrt{\gamma/\rho g}$ [28]. It is on the order of a few millimeters for most liquids, thus, gravitational forces can often be neglected on the nano- and micrometer scale [28], where many biological processes take place.

1.1.2 The Young-Dupré relation

When a liquid droplet is placed on a solid substrate, it forms an interface of area A_c that depends on the interfacial forces—a process called *wetting*. From Eq. (1.1) follows that the curvature at the free surface is constant, i.e. the droplet takes the shape of a spherical cap [Fig. 1.1(b)]. Given that γ_c, γ_f and γ_m describe the surface tensions at the droplet-substrate, droplet-medium and substrate-medium interface, respectively, one can distinguish three regimes:

- total wetting: $\gamma_\mathrm{m} > \gamma_\mathrm{c} + \gamma_\mathrm{f}$, droplet spreads completely
- partial wetting: $\gamma_\mathrm{c} - \gamma_\mathrm{f} < \gamma_\mathrm{m} < \gamma_\mathrm{c} + \gamma_\mathrm{f}$, droplet spreads partially
- total dewetting: $\gamma_\mathrm{m} < \gamma_\mathrm{c} - \gamma_\mathrm{f}$, droplet rounds up completely.

The surface tension—an energy per area—has units of $\mathrm{N\,m^{-1}}$ and acts like a force per unit length. In particular, when an adhesive droplet reaches equilibrium, all forces acting on the contact line, i.e. the triple line separating fluid, substrate and surrounding medium, must be balanced. From the projection of the equilibrium forces onto the solid substrate follows the Young-Dupré relation [37]

$$\frac{\gamma_\mathrm{c} - \gamma_\mathrm{m}}{\gamma_\mathrm{f}} = \cos\frac{\theta}{2}, \tag{1.2}$$

in which θ is the *contact angle* between droplet and substrate [Fig. 1.1(b)] [28]. It can only be defined outside the total wetting regime. Measuring shape parameters like the contact angle can thus inform about the relative magnitude of equilibrium forces.
Interestingly, materials can have similar contact angles, but vary greatly in their adhesion energy. For instance, lotus leaves as well as rose pedals are superhydrophobic, however, droplets stay pinned to a rose pedal, while they easily slide off the lotus leaf [38]. The surface tension at solid-liquid interfaces can span several orders of magnitude: ionic or metallic surfaces are considered high energy surfaces with γ_m ∼500–5000 $\mathrm{mN\,m^{-1}}$ in air, allowing nearly any liquid to spread. In contrast, many molecular crystals and plastics are low energy surfaces with chemical binding energies on the order of $k_\mathrm{B}T$, resulting in γ_m ∼10–50 $\mathrm{mN\,m^{-1}}$ [28].

1.1.3 Contact areas between Young-Laplace droplets

The total surface energy of a system of N interacting droplets is

$$E = \sum_{i=1}^{N} \frac{\gamma_c}{2} A_{c,i} + \gamma_f A_{f,i}. \tag{1.3}$$

Consider a configuration in which each droplet has n neighbors, fixed volume V, and no triple or higher-order junctions are present (i.e. no contact-lines separating more than two droplet volumes) [Fig. 1.1(c-e)]. Similar to Eq. (1.2), the ratio of the uniform surface tensions at droplet-droplet interfaces and at the free surface determines the contact angle θ [Fig. 1.1(c)] through the force balance equation

$$\frac{\gamma_c}{2\gamma_f} = \cos\frac{\theta}{2}. \tag{1.4}$$

From Eq. (1.1) follows that in the minimal surface configuration, the droplets take the shape of truncated spheres from which n identical spherical caps were removed [Fig. 1.1(c)], each with a volume

$$v = \frac{A_c^{3/2}}{3\pi^{1/2}} \left(2 + \cos\frac{\theta}{2}\right) \left(1 - \cos\frac{\theta}{2}\right)^2. \tag{1.5}$$

The total contact area can be related to the droplet volume V through

$$A_c = n\left[1 - \cos^2\frac{\theta}{2}\right] \left[\frac{3\pi^{1/2}(V + (n-1)v))}{\left(2 - \cos\frac{\theta}{2}\right)\left(1 + \cos\frac{\theta}{2}\right)^2}\right]^{2/3}, \tag{1.6}$$

using that $V+(n-1)v$ corresponds to the volume of a spherical cap. From Eqs. (1.4)–(1.6) follows for the total contact area per droplet

$$\frac{A_c}{A_0} = n\left[1 - \cos^2\frac{\theta}{2}\right] \left[\frac{2}{\left(2 - \cos\frac{\theta}{2}\right)\left(1 + \cos\frac{\theta}{2}\right)^2 - (n-1)\left(2 + \cos\frac{\theta}{2}\right)\left(1 - \cos\frac{\theta}{2}\right)^2}\right]^{\frac{2}{3}}, \tag{1.7}$$

in which the reference area $A_0 = (3V/2)^{2/3}\pi^{1/3}$ is defined by the conserved droplet volume V [Fig. 1.1(d)]. While Eq. (1.7) holds for doublets within the full stable-contact regime $0 \leq \gamma_c \leq 2\gamma_f$, square ($n = 4$) and cubic ($n = 6$) lattices form higher order junctions when $\gamma_c/2\gamma_f \leq 1/\sqrt{2}$ [Fig. 1.1(d)]. Note that in the case of droplets with four equally spaced contacts, forming a tetrahedral configuration, the corresponding angle is $\theta = 109.5°$, however, tetrahedral arrangements are not space-filling in three dimensions. Equation (1.7) is also true for a single, adherent droplet with $n = 1$ and a contact angle θ set by Eq. (1.2) instead of Eq. (1.4).

1.2 Adaptive wettability and adhesion

The wettability of a surface can be controlled through different chemical and physical parameters [39]. Coating a solid with a molecular layer can turn a high into a low energy surface and vice versa. For instance, human tears deposit hydrophilic biomolecules on the otherwise hydrophobic cornea to stabilize its protective fluid film [40]. Given a surface chemical composition, wettability can also be tuned by changing its topography [41]: increasing surface roughness typically enhances a material's properties, making hydrophilic (hydrophobic) surfaces even more hydrophilic (hydrophobic) [28].

1.2.1 Designing smart materials with switchable wettability

Given the broad range of phenomena that depend on wetting, from biology to industry, there is a long-standing interest to control capillary forces and wettability of substrates in an adaptive manner. To develop multifunctional and intelligent surfaces, many studies concentrate on the design of stimuli-responsive materials, where wettability and adhesion can be switched reversibly, for instance in response to stretching, magnetism, light, electricity or temperature changes, via changes of the surface chemistry, the surface roughness, its nanopore structure, or by creating asymmetric stress fields [38, 42, 43, 44].

1.2.2 Adaptive adhesion in biological systems

Biological systems have mastered the ability to dynamically regulate surface forces in response to external stimuli [45, 46, 47]. For instance, the adhesion of cells is a dynamic process mediated by specialized proteins that enable interactions with both substrates and other cells.

Cells adhere to their surrounding matrix primarily via integrins, specialized transmembrane proteins that form part of large focal adhesion complexes [48, Chapter 19]. These structures couple adhesion sites to the cytoskeleton, a dynamic intracellular polymer network. The focal adhesions not only serve as mechanical anchors, but also act as mechanosensors, allowing cells to probe the stiffness and topology of their environment through contractile forces transmitted by the cytoskeleton [49]. Moreover, the cytoskeletal network itself continuously remodels in response to mechanical inputs and acts like an adaptive material regulating the cell mechanical properties [2].

Similar to substrate adhesion, cell-cell adhesion relies on transmembrane proteins like cadherins binding across the cell-cell interface. They are also coupled to the cytoskeleton and facilitate force transmission across tissues [50]. Cells can actively tune their interfacial properties by modulating the production, degradation and transport of these adhesion

molecules. In particular, cells produce varying types of adhesion molecules that interact in either a homotypic (binding to the same molecule type) or heterotypic (binding to a different molecule type) manner. This diversity forms an *adhesion code* that allows cells to sort spatially based on their differential adhesion properties [51, 52, 53].

1.2.3 Mechanochemical feedback governs signal-dependent adhesion

As outlined above, cells adapt their adhesion and other mechanical properties in response to changing environmental conditions by controlling the concentration and spatial distribution of adhesion molecules, cytoskeletal components, and their regulators [50, 54, 55]. Mechanochemical feedback arises when the coarse-grained material properties in turn control the chemical composition or spatial distribution of molecular constituents [14, 18, 56]. For instance, mechanical stresses can affect the synthesis of new molecules in cells [57], active hydrodynamic flows control the transport of cytoskeletal components and molecular motors [18, 58, 59, 60], and active stresses lead to the disassembly of macro-molecular complexes [61]. Moreover, deformations and shape changes can directly impact the microscopic dynamics by changing the domain on which these processes evolve [15, 62, 63, 64, 65, 66].

1.2.4 Contact signaling-dependent mechanochemical feedback

Environmental signals are often detected through biochemical reactions at the cell surface, for example via binding of external ligand molecules to receptors, which change the bulk concentration of proteins by regulating their production through gene transcription and translation [48, Chapter 15]. A prominent example is the Notch signaling pathway, where direct cell-cell contact is required for ligand-receptor interactions. Notch receptors on one cell bind to ligands such as Delta or Jagged on an adjacent cell. Upon receptor activation, a proteolytic cleavage event releases an intracellular receptor domain, which then translocates to the nucleus to regulate gene expression. Such signaling interactions depend on the geometry and duration of cell-cell contacts in various contexts [17, 72, 73, 74, 75]. For example, when signaling molecules bind to receptors at cell-cell or cell-substrate interfaces, the resulting response can depend on the available contact area.
In many biological contexts, contact-based mechanochemical feedback enables the coordination of signaling-dependent cellular processes with the dynamic spatial arrangement of the cells [Fig. 1.2(b-c)]. For example, Notch signaling regulates the intercalation of cone cells in the developing Drosophila eye [71] [Fig. 1.2(c)]. These cells are engaged in Notch signaling while undergoing a slow T1 transition over approximately 10 hours, in

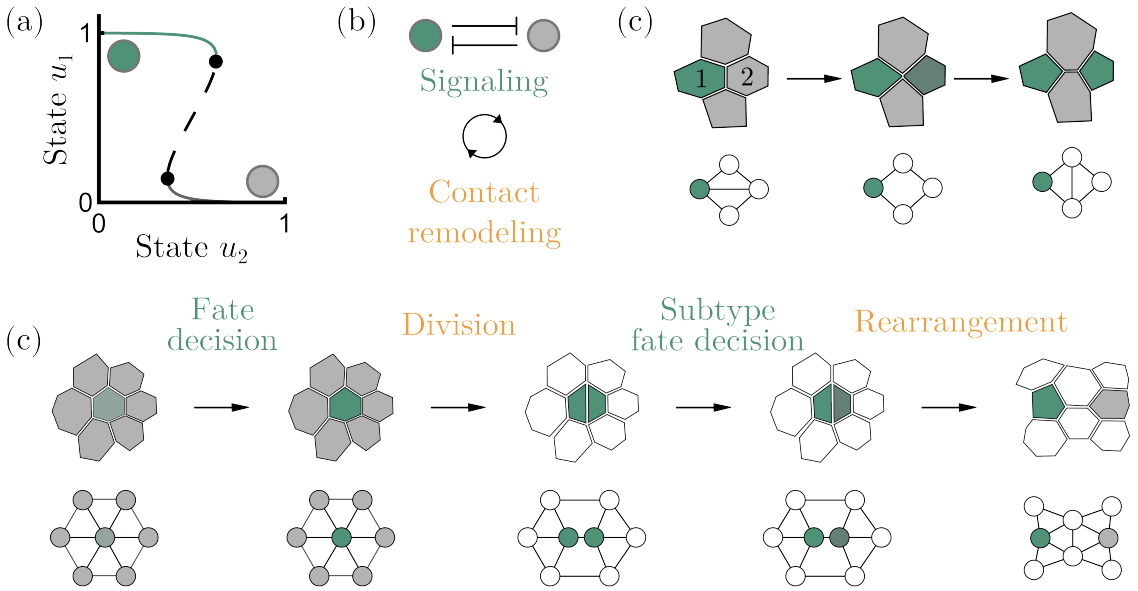

Figure 1.2. Contact-dependent signaling and mechanochemical feedback. (a) A schematic bifurcation diagram for the signaling state of a cell u_1 as a function of the cell state u_2 shows the sending state (green line) and the receiving state (gray line) separated by an unstable state (dashed line) [67, 68]. Such symmetry-breaking of states can arise when the ability of a cell to send a signal is suppressed upon receiving a signal. A common example is the Notch lateral inhibition pathway [69, 70]. (b) Cell-cell signaling upstream or downstream of adhesive or cytoskeletal components that control cellular contact area gives rise to mechanochemical feedback. (c) Schematic representations show a four-cell T1 transition in which a sending cell 1 loses contact with receiving cell 2, which consequently becomes a sending cell. A similar topological transition occurs in *Drosophila* cone cells and couples the timing of the transition to the signaling dynamics [71]. Network schematics show the cell-cell contact changes. (d) Notch-dependent cell-cell contact changes control distinct instances of signaling in zebrafish mechanosensory organs. Notch signaling specifies a sensory progenitor cell (green) amongst supporting cells (gray). This cell divides into two daughter cells that engage in a second instance of signaling to specify opposite polarity fates (green and gray), triggering oppositely oriented cell movements which terminate the signaling interactions by physically separating the cells. Figure adapted from [17].

which the contact area between a signal-sending and a signal-receiving cell decreases and is eventually lost. Blocking the contact-dependent transcription induced by Notch signaling leads to intercalation defects, suggesting that the process is governed by feedback between contact remodeling and signaling, likely through heterotypic adhesion between the diverging cell types.

1.2.5 Mechanochemical feedback drives fate patterning in mechanosensory epithelia

In the context of fate patterning, symmetry breaking describes a process in which two or more initially similar cells acquire different properties, for example, through the amplification of small differences in biochemical composition or from a mechanical instability [Fig. 1.2(a)]. In vertebrate mechanosensory epithelia, fate patterning is facilitated via Notch-dependent lateral inhibition [76]. In these organs, the constituting cells acquire a sensory fate or a supporting cell fate according to the outcome of mutually inhibitory Notch signaling interactions [76, 77, 78], and the two cell types acquire a precise mosaic organization in which each sensory cell is surrounded by non-sensory supporting cells [Fig. 1.2(d), first schematic].

For instance, *in vivo* and explant studies of the developing mouse auditory organ have shown that mechanical processes, including neighbor exchanges, affected by Notch-dependent changes in cellular properties, impact final fate patterns. [79, 80, 81]. Live imaging of explants and simulations suggest that Notch signals create a salt-and-pepper distribution of sensory cells and supporting cells that express heterotypic adhesion molecules and acquire different mechanical properties, which—in interaction with tissue-level shear stresses in the developing organ—facilitate a mechanical sorting process that arranges sensory and supporting cells into a precise mosaic pattern.

In contrast to their mammalian counterparts, mechanosensory epithelia in other vertebrates remain proliferative after patterning and, in some cases, exhibit remarkable regenerative capacity [82, 83]. In the sensory organs of the zebrafish lateral line, for example, live imaging shows high rates of proliferation with cells rearranging and continuously reshaping the contact-network topology throughout development and regeneration [68, 78]. Here, the Notch pathway regulates two interlinked fate decisions that are timed by Notch-dependent contact dynamics [Fig. 1.2(d)]. In the lateral line, two subtypes of sensory cells arise in pairs from the divisions of progenitor cells [84, 85]. One instance of Notch signaling specifies the sensory progenitor cells among the supporting cells [78, 86], while a second instance breaks the symmetry between the daughter cells to produce one of each sensory subtype [68, 87, 88]. Subsequently, the two cells form oppositely

oriented actin protrusions and move away from one another, while supporting cells intercalate, possibly aided by heterotypic adhesion [68]. The two steps are coordinated by the differentiation-induced changes in the topology of cell–cell contacts. First, the progenitor division creates a new interface between the daughter cells through which they engage in lateral inhibition, and then the elicited fate maturation process terminates this contact in a self-coordinated fashion. Thus, the formation and elimination of physical contacts between cells keep the different functions of the same pathway spatiotemporally separate. It will be interesting to explore whether the mechanochemical self-organization of fate decisions in this dynamically rearranging organ facilitates its capacity for regeneration.

1.2.6 Mechanochemical feedback in synthetic biosystems

Within a dynamic environment *in vivo*, cells receive a range of molecular signals that influence each other and are affected by ongoing external processes. It is challenging, for example, to decouple feedback effects between contact-dependent signaling and contact remodeling from the cross-talk with other signaling pathways [89]. Engineering signaling receptors to construct circuit motifs with desired properties facilitates isolating mechanisms of interest and testing predictions [90, 91]. This approach can link contact-mediated signaling to downstream effectors of cellular mechanics directly, that is, independent of other molecular pathways. Synthetic Notch receptors permit the design of custom input and output domains that can be used to program contact-dependent transcription [52, 92, 93]. Indeed, engineering cells in which receptor activation suppresses the expression of the corresponding ligand leads to mutual inhibition that breaks the symmetry and bifurcates cells into two groups of either high or low ligand expression. Moreover, programming the circuits to induce the expression of homophilic adhesion molecules downstream of receptor activation gives rise to the formation of compact structures with a core of receiving cells surrounded by ligand-expressing sending cells [52]. The results demonstrate that a simple feedback between contact-based signaling and contact remodeling can break the symmetry among initially uniform cells and drive spatial organization into distinct layers.

1.2.7 New insights from studying mechanochemical feedbacks

Gaining a formal and predictive understanding of mechanochemical systems is a core goal of theoretical biological physics [27]. It motivates novel combinations of theoretical approaches from cellular biophysics, the collective dynamics of active matter, and the nonlinear dynamics of cell–cell communication [67, 68, 94, 95]. For example, work on communicating active matter outlines how modeling collective motion with signaling

dynamics reveals new principles of multicellular organization [96]. New technologies, especially in the field of live imaging combined with optogenetics and the development of novel *ex vivo* and *in vitro* platforms, allow to monitor and manipulate the spatial dynamics of cells and their signaling states in unprecedented ways [90, 97, 98]. Increasingly complemented by theoretical approaches [81, 99, 100, 101, 102, 103, 104], these advances will reveal patterning regimes and self-organizing motifs specific to mechanochemical systems and improve the targeted manipulation and reconstitution of dynamical multicellular structures.

1.3 Objectives and Goals

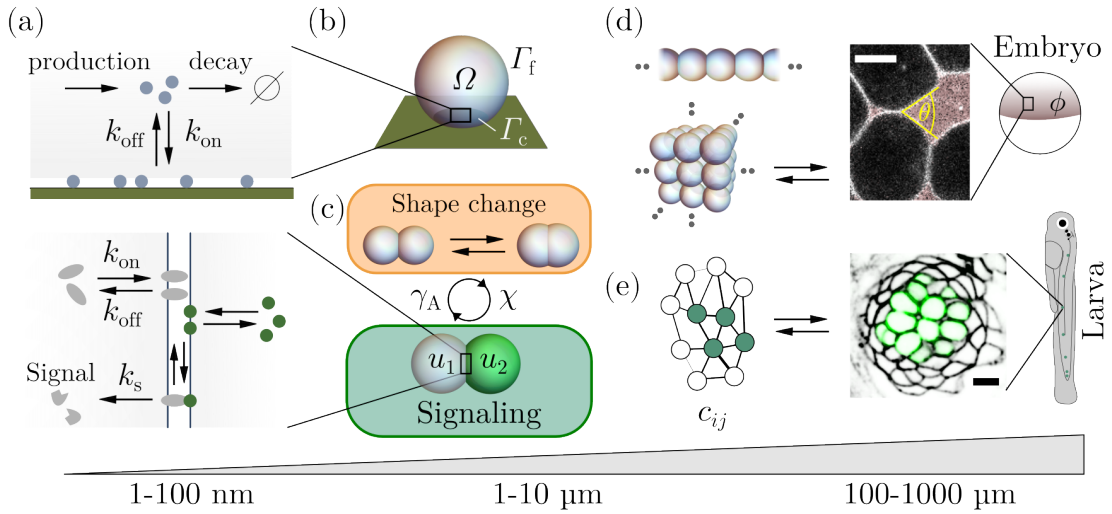

Figure 1.3. Shape-dependent feedback in contact-dependent signaling across length scales. (a) Starting from microscopic equations of contact-dependent signaling and cell adhesion coupling dynamics in the bulk Ω and the free and contact surface domains $\Gamma_{\text{f}}, \Gamma_{\text{c}}$, I derive coarse-grained equations for droplets adjusting their interfacial tensions according to their internal states u_i. (b, c) (Chapter 2), and I analyze the nonlinear dynamical landscape of state and shape dynamics (Chapter 3, 4), governed by two feedback parameters: adaptive tension γ_{A} and signal susceptibility χ. (d) I infer feedback parameters from contact angle measurements θ in microscopy images of foam-like fish embryonic tissues (image: Camilla Autorino, Petridou group, EMBL) (Section 3.7). (e) I analyze data-derived realistic contact networks in developing fish sensory organs to predict cell fate decisions (image: Adrian Jacobo, Biohub SF). Scale bar: (d) 10 µm, (e) 5 µm.

In this thesis, I present a theoretical framework of shape-dependent feedback dynamics considering various length scales, from molecular interactions at cell-cell interfaces to single cells and finally tissue-wide communication networks [Fig. 1.3].

In Chapter 2, I derive and analyze reaction-diffusion equations for signaling and adhesion molecules at cellular contacts, examining how the system's shape governs bulk and surface densities. Using a time-scale separation argument, where feedback dynamics are constrained by molecular production and degradation, I derive a set of coarse-grained equations in which concentration fields determine global state variables associated with each cell. Specifically, using the analogy between cells and droplets, I describe droplets adjusting their interfacial tension in response to exchanged signals, providing a framework with minimal degrees-of-freedom and two intrinsic feedback parameters.
In Chapters 3 and 4, I identify and analyze the dynamical regimes of the reduced equations that describe the adaptive wetting dynamics of signal-processing droplets and wet foams. Using analytical arguments, simulations, and numerical continuation, I show how the feedback between contact dynamics and signaling states drives rich phenomena, including multistability, symmetry-breaking, excitability, and self-sustained oscillations [105, 106]. For specific configurations, I recover bifurcation structures which are topologically equivalent to those found in conductance-based neuronal models of action potential generation. Interestingly however, the corresponding adaptive wetting dynamics are driven by nonlinear terms arising from the system's geometrical and mechanical properties. Collaborating with experimental experts, I apply my theoretical results, and use imaging data from zebrafish embryos to infer the mechanochemical feedback parameters operating in this system. I find that the critical point associated with mechanochemical multistability supports the establishment of the ectoderm-mesendoderm boundary, determining the tissue region which later forms the internal parts of the organism.
Chapter 4 focuses on the collective scale where the topology of the contact network determines the pattern formation of states. The framework is first analyzed in a simplified one-dimensional model showcasing how patterning of states depends on short vs. long-range signaling interactions, how multistability can arises from self-activating state dynamics, and how traveling defects can appear from asymmetric coupling. I then apply the framework to realistic contact network topologies derived from live microscopy data of developing fish embryos, which enables the successful localization of cell differentiation events.

Table 1.1. List of recurring mathematical symbols and bifurcation types

Symbol	**Description**
Ω	Bulk domain
Γ	Surface domain
θ	Contact angle
Continued on next page	

Table 1.1 – Continued from previous page

Symbol	Description
γ_{c}	Contact surface tension
γ_{f}	Free surface tension
γ_{m}	Surface tension at substrate-medium interface
A_{c}	Contact surface area
A_{f}	Free surface area
V	Droplet volume
ρ	3D radius of a spherical cap shaped droplet
ρ_0	Volume-dependent reference radius ($V = \frac{4\pi}{3}\rho_0^3$)
r	Radial coordinate at the contact site
(ϑ, ϕ)	Spherical coordinates at the free surface
$r_{\max}$	Radius of the contact site
p	Laplace pressure
E	Surface energy
W	Thermodynamic work
n	Number of contacts per droplet
m_{X}	Surface density of molecule species X
c_{X}	Bulk concentration of molecule species X
$D_{m\mathrm{X}}$	Lateral diffusion coefficient on the surface of molecule species X
$D_{c\mathrm{X}}$	Bulk diffusion coefficient of molecule species X
j_{X}	Flux between bulk and surface of species X
$k_{\mathrm{on}}^{\mathrm{X}}$	Rate of binding to the surface (e.g exocytosis) of species X
$k_{\mathrm{off}}^{\mathrm{X}}$	Rate of molecule release from the surface (e.g. endocytosis) of species X
$k_{\mathrm{p}}^{\mathrm{X}}$	Bulk production rate of molecule species X
$k_{\mathrm{d}}^{\mathrm{X}}$	Bulk decay rate of molecule species X
k_{s}	Cleavage rate of receptor-ligand complexes
k_+	Rate of receptor-ligand binding
k_-	Rate of receptor-ligand dissociation
τ	Time scale parameter
u_i	Internal state of cell/droplet i
s	Received signal
σ	Response function
χ	Signal susceptibility
ϕ	Available signal
γ_{A}	Adaptive adhesion coefficient

Continued on next page

Table 1.1 – Continued from previous page

Symbol	**Description**
γ_0	Baseline tension at the contact site
h	Hill coefficient in response functions
c_{ij}	Coupling matrix containing the contact topology
SN	Saddle node
H	Hopf bifurcation
Hom	Homoclinic bifurcation
HomSN	Homoclinic-to-saddle-node bifurcation (SNIC)
SHET	Saddle Heteroclinic bifurcation
LPC	Limit point of cycles bifurcation
CP	Cusp bifurcation
PF	Pitchfork bifurcation
BT	Bogdanov-Takens bifurcation
GH	Generalized Hopf bifurcation
NCH	Non-central homoclinic to saddle-node bifurcation
SP	Saddle node pitchfork bifurcation
BTC	Bogdanov-Takens-Cusp bifurcation

Chapter 2

Microscopic dynamics of contact-based signaling and adhesion

The macroscopic shape and state dynamics of active materials arise from nonequilibrium microscopic processes. In living systems, active processes are driven by a large set of biochemical interactions forming complex networks with nonlinearities arising, for instance, from cooperative binding [67, 107, 108]. As molecular interactions take place in space and time, additional nonlinearities arise from geometrical relations [109]. The involvement of multiple molecular components and the coupling of reaction and transport processes across different temporal and spatial scales makes it difficult to identify general principles. In this chapter, I address this gap by deriving tractable coarse-grained equations from the microscopic dynamics for a class of mechanochemical systems, in which biochemical signal processing is coupled to shape dynamics. Specifically, I introduce sets of bulk and surface reaction-diffusion equations for molecules that mediate (i) the exchange of contact-based chemical signals, and (ii) adhesion at contact surfaces. I discuss how steady state concentrations of signaling molecules depend on the systems geometry, and link these results to experiments reported in literature. In the last section of this chapter, I derive a set of tractable coarse-grained equations for mechanochemical systems, in which contact-based signals are coupled to the regulation of adhesion, by employing a separation of time scales that arises naturally when changes in the chemical composition depend on transcriptional and translational regulation, i.e. the slow synthesis of new protein molecules. Chapters 3 and 4 present a detailed nonlinear dynamics analysis of this set of equations and their application to model experimental data.

2.1 Reaction-diffusion equations with surface-bulk coupling

Consider continuity equations for particle densities c in the bulk Ω and m on the surface Γ of the form [110]

$$\partial_t c = D_\mathrm{c}\nabla^2 c + \mathcal{R}_\mathrm{c} \tag{2.1}$$

$$\partial_t m = D_\mathrm{m}\nabla^2 m + \mathcal{R}_\mathrm{m} \tag{2.2}$$

with diffusion coefficients $D_\mathrm{c}, D_\mathrm{m}$ in three and two dimensions respectively, and reaction terms $\mathcal{R}_\mathrm{c}$ and $\mathcal{R}_\mathrm{m}$. I do not consider convective flows or other active transport processes here. The boundary condition

$$-D_\mathrm{c}(\mathbf{n}\cdot\nabla)\, c|_\Gamma = j \tag{2.3}$$

couples the bulk and surface densities via the flux j between bulk and surface where $\mathbf{n}$ is the normal vector to the surface pointing outwards. A simple form of this flux is given by [74, 111]

$$j = k_\mathrm{on} c|_\Gamma - k_\mathrm{off} m \tag{2.4}$$

with k_on setting the rate with which molecules bind to the surface and k_off the rate with which they are released into the bulk. I consider the bulk reaction term [112]

$$\mathcal{R}_\mathrm{c} = k_\mathrm{p} - k_\mathrm{d} c \tag{2.5}$$

with k_p the active production of molecules (e.g. due to protein translation in cells) driving the system out of thermodynamic equilibrium, and k_d the rate of decay. The surface reactions $\mathcal{R}_\mathrm{m}$ are specified in the following sections, where I consider different molecular processes governing adhesion and contact-based signaling.

Averaging Eq. (2.1) over the bulk's volume V and using Eqs. (2.3) and (2.5) yields the dynamic equation for the average bulk concentration $\langle c\rangle$

$$\frac{d\langle c\rangle}{dt} = k_\mathrm{p} - k_\mathrm{d}\langle c\rangle - \frac{1}{V}\int_\Gamma j dA. \tag{2.6}$$

Defining the steady state average densities in the absence of boundary flux as the reference density $c^0 = k_\mathrm{p}/k_\mathrm{d}$ and $m^0 = k_\mathrm{on}c^0/k_\mathrm{off}$ permits introducing normalized particle densities c/c^0 and m/m^0.

With diffusion timescale $\tau_\mathrm{D} = V^{2/3}/D_\mathrm{c}$ and reaction timescales $\tau_\mathrm{R} = 1/k_\mathrm{d}$ and $\tau_\mathrm{on} = V^{1/3}/k_\mathrm{on}$, Eq. (2.1) and Eq. (2.3) with time rescaled in units of $\tau = t/\tau_\mathrm{R}$ read

$$\frac{\tau_\mathrm{D}}{\tau_\mathrm{R}}\frac{\partial_\tau c}{c^0} = V^{2/3}\nabla^2\frac{c}{c^0} + \frac{\tau_\mathrm{D}}{\tau_\mathrm{R}}\left(1 - \frac{c}{c^0}\right), \tag{2.7}$$

$$(\mathbf{n}\cdot\nabla)\,\frac{c}{c^0}\Big|_\Gamma = \frac{\tau_\mathrm{D}}{\tau_\mathrm{on}V^{1/3}}\left(\frac{m}{m^0} - \frac{c}{c^0}\right). \tag{2.8}$$

The focus of this work are the long time scale dynamics dominated by protein synthesis and decay. Given that the regulation of transcription, translation and the turnover of proteins are slow processes that require tens of minutes to hours and can vary greatly between different protein species [113, 114, 115], I assume that they dominate the dynamics. In comparison, biochemical interactions, diffusive transport across cellular scales and frictional time scales are typically at least an order of magnitude faster – set by diffusive, biochemical, and viscoelastic timescales on the order of seconds to minutes [74, 114, 116, 117]. Accordingly, I assume that bulk and surface concentrations relax to their steady state solutions, and that the system takes on equilibrium shapes. More specifically, I consider the limit in which bulk diffusion is fast compared to the reaction kinetics, i.e. $\tau_\mathrm{D} \ll \tau_\mathrm{R}$ and $\tau_\mathrm{D} \ll \tau_\mathrm{on}$. In this limit, the boundary condition Eq. (2.8) is reflective and Eq. (2.7) becomes a Laplace equation that is solved by a uniform concentration set by the solution of Eq. (2.6) (*shadow limit* [118]).
The surface of a cell, which is in contact with another cell or a substrate, can be separated into the domain of the contact interface Γ_c and the free surface Γ_f [Fig. 2.1(a)]. At the free surface, molecules can be exchanged with the bulk, but interactions between adhesion or signaling molecules are restricted to the contact interface. The reaction term at the free surface is therefore $\mathcal{R}_m|_{\Gamma_\mathrm{f}} = j$.

In the following sections, I introduce the reaction terms and corresponding boundary fluxes for contact-based signaling and adhesion dynamics and compute the steady state bulk and surface densities that fulfill Eqs. (2.2), (2.6).Note that lateral diffusion coefficients of proteins on lipid membranes are variable and on the order of 0.01–10 $\mu\mathrm{m}^2\,\mathrm{s}^{-1}$ [74, 117, 119, 120], allowing density fields to acquire their steady state within seconds over micrometer length-scales, while equilibration takes substantially longer in larger systems, such as synthetic biomimetic droplets [121].

2.2 Biochemical signaling interactions at contact surfaces

Cells respond to molecular signals from the environment by changing their internal properties. Many cellular signals are transmitted via the binding of chemicals to receptor molecules located at the cell surface (Section 1). These chemical events trigger internal processes, which result in changes to the molecular composition, spatial organisation, and corresponding functions of cells [48, Chapter 15].
Following the example of the Delta-Notch signaling pathway (Section 1.2.4), I consider the

reaction-diffusion dynamics of receptors (R), ligands (L), and receptor-ligand complexes (RL) at a signaling interface, and derive how the bulk concentration of signal molecules (S) depends on receptor-ligand binding at the boundary [Figs. 2.1, 2.8]. In particular, I discuss different cases of active biochemical regulation and limits in which scaling laws between the exchanged signal and different rates, concentration constants and geometrical properties can be derived.

2.2.1 A cell on a signal-transmitting substrate

I begin by considering a single cell in contact with a solid substrate that is functionalized with immobile ligands at a fixed uniform density $m_{\mathrm{L}}^{\max}$, similar to experimental systems developed for the Notch pathway in *in vitro* assays [122] [Fig. 2.1(b)]. The cell contains receptor molecules, signaling molecules, and regulator molecules with bulk concentrations $c_{\mathrm{R}}, c_{\mathrm{S}}$, and c_{U} respectively, whose dynamics are coupled via the reactions at the contact surface. I do not explicitly consider a bulk concentration of ligands, because the substrate has no receptor molecules to bind to—the cell is only receiving, but not sending signals. To describe the signaling dynamics at the surface, I use Eq. (2.2) for the surface densities of receptors m_{R}, substrate-bound ligands m_{L} and receptor-ligand complexes m_{RL} with the reaction terms adapted from Khait et al. (2016) [74]

$$\mathcal{R}_{m_{\mathrm{R}}} = k_{\mathrm{on}}^{\mathrm{R}} c_{\mathrm{R}} - (k_{\mathrm{off}}^{\mathrm{R}} + k_{+} m_{\mathrm{L}}) m_{\mathrm{R}} + k_{-} m_{\mathrm{RL}}, \tag{2.9}$$

$$\mathcal{R}_{m_{\mathrm{L}}} = (k_{-} + k_{\mathrm{s}}) m_{\mathrm{RL}} - k_{+} m_{\mathrm{L}} m_{\mathrm{R}}, \tag{2.10}$$

$$\mathcal{R}_{m_{\mathrm{RL}}} = k_{+} m_{\mathrm{L}} m_{\mathrm{R}} - (k_{-} + k_{\mathrm{s}}) m_{\mathrm{RL}}, \tag{2.11}$$

which are explained in the following [Fig. 2.1(b)]. Receptors are recruited to the surface with a rate set by $k_{\mathrm{on}}^{\mathrm{R}}$ (exocytosis) and they are removed from the surface with rate $k_{\mathrm{off}}^{\mathrm{R}}$ (endocytosis) [123]. Receptors at the contact surface bind ligands at a rate determined by k_{+} to form receptor-ligand complexes, which unbind with rate k_{-}. Receptor-ligand complexes undergo an irreversible enzymatic cleavage with rate k_{s} upon which a fragment of the bound receptor molecule is released into the bulk and acts as a signaling molecule (S), the remaining part is degraded, and the ligand is released within the surface where it can bind to a new receptor molecule. The bulk concentrations of receptors c_{R} and signaling molecules c_{S} are coupled to the signaling dynamics at the contact via Eq. (2.6). The ligands on the substrate are fixed in place such that $D_{m_{\mathrm{L}}} = 0, D_{m_{\mathrm{RL}}} = 0$ in Eq. (2.2). The density of unbound ligands is the difference between the total density of ligands covering the substrate and the density of receptor-ligand complexes $m_{\mathrm{L}} = m_{\mathrm{L}}^{\max} - m_{\mathrm{RL}}$. Eqs. (2.2) and (2.11) together with this relation permit expressing the normalized steady state concentration of receptor-ligand complexes in terms of the steady state receptor

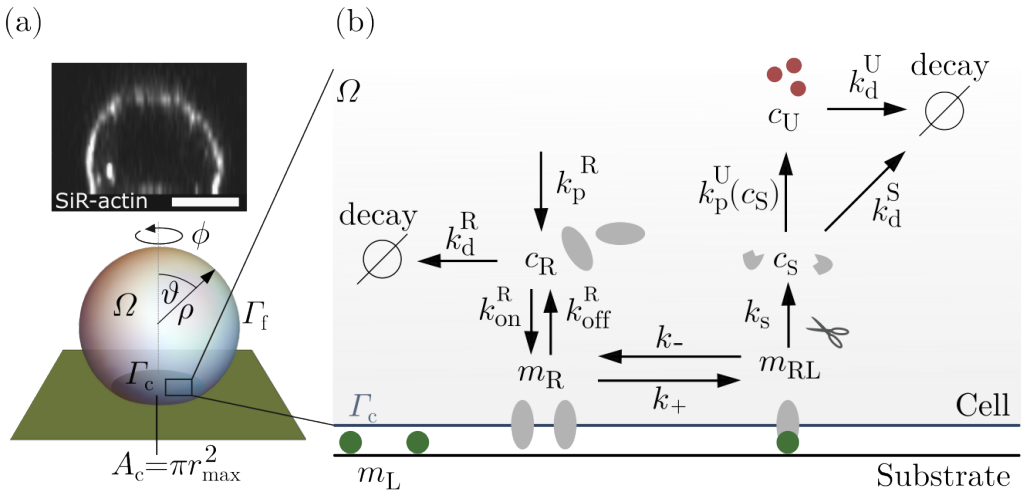

Figure 2.1. Microscopic interactions underlying signaling. (a) Schematics of a spherical-cap shaped cell of radius ρ adhering to a substrate with bulk Ω and the free and contact surface domains Γ_f, Γ_c, respectively. The radial symmetric contact has radius r_{max}. The free surface can be parameterized in spherical coordinates (ϕ, θ). The fluorescence microscopy image shows the actin cortex of a 3T3 fibroblast on a micropatterned substrate, stained with SiR-actin (Image courtesy of Alba Diz-Muñoz) . Scale bar: 5 µm. (b) Contact-dependent signals are received from a ligand-coated substrate. Receptor (R, gray) and ligand (L, green) molecules bind across the interface and form receptor-ligand complexes (RL). Receptors are produced in the bulk, exchanged with the surface and bind to substrate-bound ligands. Receptor-ligand complexes are cleaved irreversibly [70], which releases a signaling molecule (S, gray) into the bulk. Regulator molecules (U, red) are produced with a rate depending on the bulk concentration of signal molecules, and can in turn determine the production rate of new ligands (Section 2.3.1). Substrate-bound ligand molecules are released upon the cleavage event and can bind a new receptor. Here, c and m denote bulk and surface concentrations respectively, and k denote the kinetic rates of the reactions.

concentration as

$$\frac{m_{\mathrm{RL}}}{m_{\mathrm{L}}^{\max}} = \frac{m_{\mathrm{R}}}{m_{\mathrm{R}} + \dfrac{k_{\mathrm{s}} + k_{-}}{k_{+}}}. \tag{2.12}$$

The ratio of rate constants $\frac{k_{\mathrm{s}}+k_{-}}{k_{+}}$ defines the steady state receptor surface density at which half of all ligands are bound in receptor-ligand complexes [Fig. 2.2].
Parameter values reported for the Notch signaling pathway are summarized in Tab. 2.1, suggesting a value of $\sim 2.4\,\mu\mathrm{m}^{-2}$, far less than the typical receptor concentrations of 10–$1000\,\mu\mathrm{m}^{-2}$ reported for biological cells [124, Chapter 15],[74].
Given Eqs. (2.2), (2.9) and (2.12), the steady state relation for the distribution of receptors reads

$$0 = D_{m_{\mathrm{R}}} \nabla^2 m_{\mathrm{R}} + k_{\mathrm{on}}^{\mathrm{R}} c_{\mathrm{R}} - m_{\mathrm{R}} \left(k_{\mathrm{off}}^{\mathrm{R}} + \frac{k_s k_+ m_{\mathrm{L}}^{\max}}{k_+ m_{\mathrm{R}} + k_{\mathrm{s}} + k_{-}} \right). \tag{2.13}$$

The steady state bulk concentration of signaling molecules following Eq. (2.6) with $j_{\mathrm{S}} = -k_{\mathrm{s}} m_{\mathrm{RL}}$ and $k_{\mathrm{p}}^{\mathrm{S}} = 0$ is then

$$c_{\mathrm{S}} = \frac{k_{\mathrm{s}} m_{\mathrm{L}}^{\max}}{k_{\mathrm{d}}^{\mathrm{S}}} \int_{\Gamma_{\mathrm{c}}} \frac{m_{\mathrm{R}}}{m_{\mathrm{R}} + \dfrac{k_{\mathrm{s}} + k_{-}}{k_{+}}} dA, \tag{2.14}$$

where I used Eq. (2.12). The cleavage of the receptor-ligand complex leading to the loss of receptor molecules at the surface is characteristic for the Notch pathway and implies that steady states are out of thermal equilibrium with a constant particle flux from the bulk to the surface. In many other biochemical pathways, receptor molecules are recycled and receptor-ligand complexes induce the production of downstream signaling molecules, e.g. through enzymatic activity [48, Chapter 15], until they unbind. As I show in the following, the cleavage process is key to observe non-uniform steady state surface distributions. Note that despite their complexity and nonlinear relations, the reaction terms (2.9)–(2.11) are still a simplification of the real biological system. For instance, the

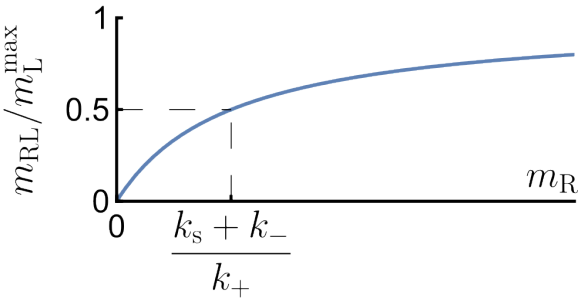

Figure 2.2. Fraction of ligands bound in receptor-ligand complexes as a function of the steady state receptor concentration [Eq. (2.12)].

cleavage rate k_s depends on other proteins and their concentration, cells posses different versions of receptor and ligand molecules with different binding and unbinding rates, and receptors can be chemically modified, which changes their reaction and diffusion properties. Nevertheless, these terms have been used successfully to quantify relations between molecule distributions, signal molecule production and contact area [74].

Constant bulk concentrations

To distinguish between effects arising from surface-bulk coupling and from the dynamics within the surface, I start with the assumption that the steady state bulk concentration of receptors $c_R = c_R^0$ is constant. This is the case, for instance, if feedback effects in the production rate of receptor molecules compensate for the loss of receptors through degradation in the bulk and at the surface [Eqs. (2.4), (2.6)], i.e.

$$k_p^R = c_R^0 \left(k_d^R + \frac{k_{on}^R A}{V} \right) - \frac{k_{off}^R}{V} \int_\Gamma m_R dA. \tag{2.15}$$

Indeed, biological cells possess a range of active feedback mechanisms to adapt their protein synthesis and degradation rates to maintain constant protein levels [125, 126], effectively acting as a *chemostat* that preserves a constant chemical potential. Similar assumptions have been used successfully to study how signaling depends on the surface distribution of receptor molecules in the Notch pathway [74].

The spherical cap geometry

In the following, I assume radial symmetry, which reduces Eq. (2.13) to the one-dimensional equation

$$0 = \frac{D_{m_R}}{r} \frac{\partial}{\partial r} \left(r \frac{\partial m_R}{\partial r} \right) + k_{on}^R c_R^0 - m_R \left(k_{off}^R + \frac{k_s k_+ m_L^{max}}{k_+ m_R + k_s + k_-} \right). \tag{2.16}$$

with $r \geq 0$ the radial coordinate. Such symmetry is given, for instance, in spherical cap shaped droplets—the equilibrium shape of a Young-Laplace droplet set by the balance between the Laplace pressure and the uniform surface tensions associated with the different surfaces (Section 1.1). Introducing the free diffusion length scale before a receptor is removed from the surface $l_{D,f} = \sqrt{D_{m_R}/k_{off}^R}$ and the reference receptor density $m_R^0 = k_{on}^R c_R^0 / k_{off}^R$ ($l_D \approx 1\,\mu m$, $m_R^0 \approx 100\,\mu m^{-2}$ for values in Tab. 2.1), I can write Eq. (2.16) for the normalized receptor concentration $M_R = m_R/m_R^0$ as

$$0 = \frac{l_{D,f}^2}{r} \frac{\partial}{\partial r} \left(r \frac{\partial M_R}{\partial r} \right) + 1 - M_R \left(1 + \frac{k_s k_+ m_L^{max}}{k_{off}^R (k_+ M_R m_R^0 + k_s + k_-)} \right). \tag{2.17}$$

At the free (non-contact) surface, molecules can be exchanged with the bulk, but interactions of signaling molecules are restricted to the contact interface. The reaction term

at the free surface is therefore $\mathcal{R}_m|_{\Gamma_\mathrm{f}} = j$. Given the spherical-cap geometry, the free surface can be parameterized in terms of the spherical coordinates ϑ, ϕ [Fig. 2.1(a)] and the steady state receptor concentration at the free surface follows

$$0 = \frac{l_{\mathrm{D,f}}^2}{\rho^2 \sin(\vartheta)^2} \frac{\partial}{\partial \vartheta} \left(\sin(\vartheta) \frac{\partial M_\mathrm{R}}{\partial \vartheta} \right) + 1 - M_\mathrm{R} \tag{2.18}$$

which is independent of the azimuthal angle ϕ due to axial symmetry. Note that the receptor distribution at the free surface only depends on the diffusive length scale $l_{\mathrm{D,f}}$ relative to the system size ρ and the boundary conditions. Demanding that solutions are smooth everywhere, in particular, $\frac{\partial M_\mathrm{R}}{\partial \vartheta}\Big|_{\vartheta=0} = 0$, Eq. (2.18) is solved by

$$M_\mathrm{R}|_{\Gamma_\mathrm{f}} = 1 + \mathcal{C}_1 P_\lambda (\cos \vartheta) \tag{2.19}$$

where P_λ is the generalized Legendre polynomial of degree

$$\lambda = -\frac{1}{2} + \sqrt{\frac{l_{\mathrm{D,f}}^2 - 4\rho^2}{4 l_{\mathrm{D,f}}^2}} \tag{2.20}$$

with ρ the three-dimensional radius of the spherical cap [Fig. 2.1(a)], which is related to the fixed volume V and the contact side radius r_max via

$$\rho = \frac{r_\mathrm{max}^2 + z(r_\mathrm{max}, V)^2}{2 z(r_\mathrm{max}, V)} \tag{2.21}$$

with

$$z(r_\mathrm{max}, V) = \sqrt[3]{\frac{3}{\pi} V + \sqrt{\frac{9}{\pi^2} V^2 + (r_\mathrm{max})^6}} + \sqrt[3]{\frac{3}{\pi} V - \sqrt{\frac{9}{\pi^2} V^2 + (r_\mathrm{max})^6}} \tag{2.22}$$

the height of the spherical cap [Appendix B].

Given that solutions are continuous and particles diffusing between free and contact surface are conserved, the two surfaces are coupled by the boundary conditions

$$M_\mathrm{R}(\vartheta)|_{\partial\Gamma_\mathrm{f}} = M_\mathrm{R}(r)|_{\partial\Gamma_\mathrm{c}}\,, \tag{2.23}$$

$$\frac{1}{\rho} \frac{\partial M_\mathrm{R}(\vartheta)}{\partial \vartheta}\bigg|_{\partial\Gamma_\mathrm{f}} = - \frac{\partial M_\mathrm{R}(r)}{\partial r}\bigg|_{\partial\Gamma_\mathrm{c}}\,. \tag{2.24}$$

In the following sections, I showcase three different limits in which Eqs. (2.17),(2.18) can be solved analytically as well as numerical solutions to the more general case.

Limit 1: low ligand density

In the limit of low ligand density $m_\mathrm{L}^\mathrm{max}$, I can consider the binding rate of receptor molecules to be small compared to their release rate into the bulk, i.e.

$$k_\mathrm{off}^\mathrm{R} \gg k_+ m_\mathrm{L}^\mathrm{max}. \tag{2.25}$$

Parameter	Symbol	Value
Endocytosis	k_{off}	$0.02\,\text{s}^{-1}$
Cleavage	k_{s}	$0.34\,\text{s}^{-1}$ (limit1,2) $34\,\text{s}^{-1}$(limit3)
Binding	k_{+}	$0.167\,\mu\text{m}^2\,\text{s}^{-1}$
Unbinding	k_{-}	$0.034\,\text{s}^{-1}$
Diffusion coefficients	$D_{m_{\text{R}}}, D_{m_{\text{L}}}$	0.02–$0.08\,\mu\text{m}^2\,\text{s}^{-1}$
Exocytosis receptors	$k_{\text{on}}^{\text{R}} c_{\text{R}}^0$	$2\,\mu\text{m}^{-2}\,\text{s}^{-1}$
Exocytosis ligands	$k_{\text{on}}^{\text{L}} c_{\text{L}}^0$	$0.2\,\mu\text{m}^{-2}\,\text{s}^{-1}$
Cell radius	ρ_0	$5\,\mu\text{m}$
Volume	V	$\frac{4}{3}\pi\rho_0^3$
Contact area	A_{c}	0–$125\,\mu\text{m}^2$
Ligand density	$m_{\text{L}}^{\max}$	$0.1\,\mu\text{m}^{-2}$ (limit 1) $5\,\mu\text{m}^2$ (limit 2) $10\,\mu\text{m}^{-2}$ (limit 3)

Table 2.1. Measured and estimated parameter values for reaction and diffusion rates of receptor and ligand molecules as reported in [74], and typical cellular length scales

It simplifies Eq. (2.17) to a Bessel equation

$$0 = \frac{l_{\text{D,f}}^2}{r}\frac{\partial}{\partial r}\left(r\frac{\partial M_{\text{R}}}{\partial r}\right) + 1 - M_{\text{R}}. \tag{2.26}$$

Demanding that solutions are smooth at the center of the contact, i.e. $\frac{\partial M_{\text{R}}}{\partial r}\big|_{r=0} = 0$, it is solved by

$$M_{\text{R}} = 1 + \mathcal{C}_2 I_0\left(r/l_{\text{D,f}}\right) \tag{2.27}$$

with I_n the modified Bessel function of first kind and order n and $\mathcal{C}_2$ an integration constant that depends on the boundary conditions. Solving for the integration constants of Eqs. (2.19),(2.27) given boundary conditions (2.23),(2.24) yields a uniform surface density of receptors $M_{\text{R}} = 1$ (i.e. $\mathcal{C}_1 = \mathcal{C}_2 = 0$) at both surfaces, set by the balance between receptor transport to and from the surface, because the loss of receptors due to signaling is negligible and does not appear in Eq. (2.26). Correspondingly, the density of receptor-ligand complexes at the contact side is uniform [Eq. (2.12)]. The bulk concentration of signaling molecules [Eq. (2.14)]

$$c_{\text{S}} = \frac{k_{\text{s}} k_{+} m_{\text{R}}^0}{k_{\text{d}}^{\text{S}}(k_{+} m_{\text{R}}^0 + (k_{-} + k_{\text{s}}))} m_{\text{L}}^{\max} A_{\text{c}} \tag{2.28}$$

scales linearly with the contact size A_{c} [Fig. 2.1(a)] and the ligand density on the substrate. It approaches the limit $c_{\text{S}} = \frac{k_{\text{s}}}{k_{\text{d}}^{\text{S}}} m_{\text{L}}^{\max} A_{\text{c}}$ when m_{R}^0 is large due to high production

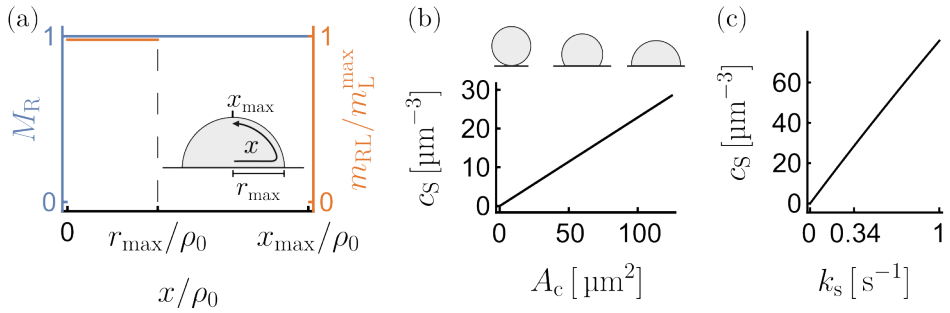

Figure 2.4. Limit of low ligand density. (a) Normalized distribution of receptors and receptor-ligand complexes are uniform due to negligible receptor loss at the surface. (b, c) The bulk signal molecule concentration scales linear with contact area (b) and nearly linear with the cleavage rate k_s (c). Parameter values as given in Tab. 2.1.

and low decay in the bulk or fast transport to the surface. Alternatively, the limit $c_S = \frac{k_+ m_R^0}{k_d^S} m_L^{max} A_c$ is valid when the right-hand-side of Eq. (2.28) is dominated by a fast cleavage rate k_s. The loss of receptors due to cleavage of the receptor-ligand complex is characteristic for Notch signaling, while in many other biochemical pathways, receptor molecules are recycled. In that case, Eq. (2.26) is generally valid [Appendix C] and steady state surface densities are uniform.

Typical parameter values for the rate constants of the Notch signaling pathway are summarized in Tab 2.1. The endocytosis rate k_{off}^R was measured in *in vitro* experiments to be $\sim 0.02\,s^{-1}$ [74] and the receptor-ligand binding rate k_+ estimated to $0.167\,\mu m^2\,s^{-1}$, thus, limit (2.25) would imply that $m_L^{max} \ll 0.12\,\mu m^{-2}$. For biological cells with contacts typically on the order of 0–100 μm^2, it would imply the detection of single molecules per contact side, making the system very susceptible to noise. Cells rather express 10–100 m^{-2} ligands on their surface and *in vitro* experiments have been conducted on substrates covered with $> 1000\,m^{-2}$ ligands [122]. In conclusion, the loss of receptor molecules due to signaling is often not negligible compared to the endocytosis rate. In the following, I show that the loss of molecules at the surface leads to non-uniform steady state surface densities of receptor-ligand complexes, causing nonlinear relationship between contact size and signal molecule concentration.

Limit 2: receptor excess

In the limit of a receptor excess compared to the ligand density m_L^{max} covering the substrate, most receptors at the surface remain unbound. It allows to expand Eq. (2.12) in the limit of small $(k_s + k_-)/(k_+ m_{R^0})$ ($(k_s + k_-)/(k_+ m_R^0) \approx 0.02$ given the values in

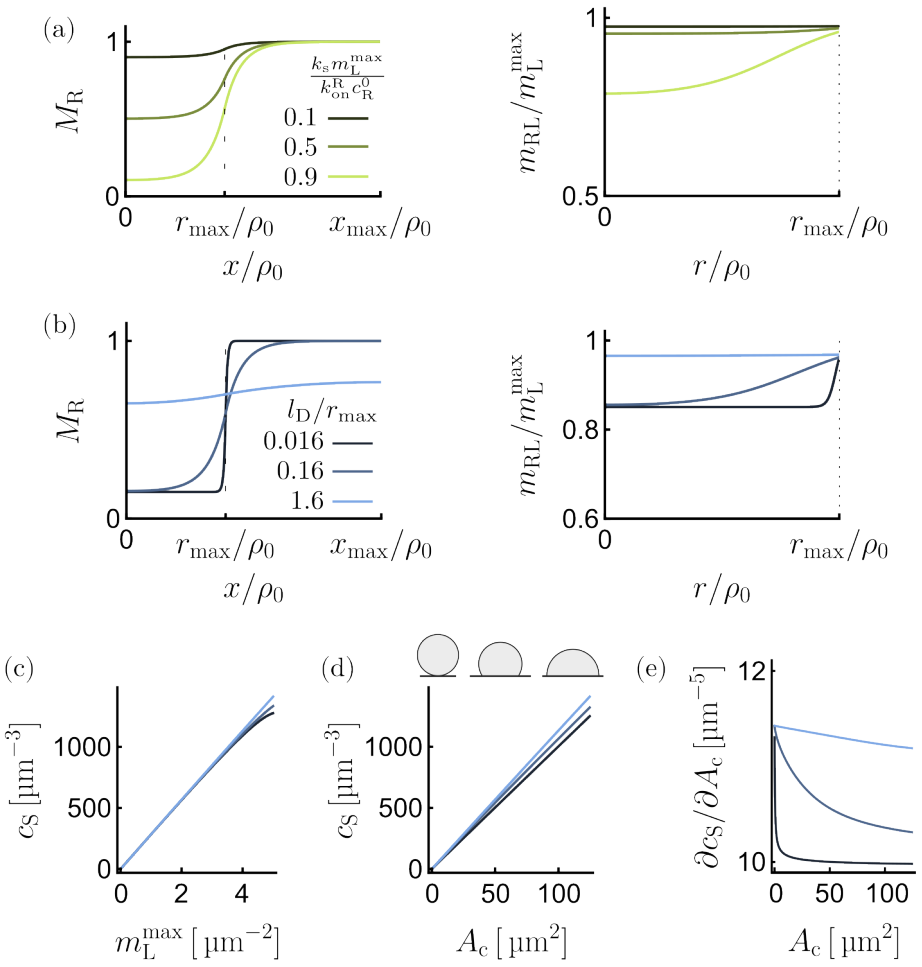

Figure 2.5. Limit of receptor excess. (a) Non-uniform distributions of surface receptors (left) translate to nearly uniform receptor-ligand complexes distributions (right) for small cleavage rates, because nearly all ligands are bound. (b-e) Varying the diffusion length scales alters the surface densities of receptors (b, left) and receptor-ligand complexes (b, right). Despite the non-uniform receptor-ligand complex distribution, the signal molecule concentration scales nearly linearly with the ligand density (c) and contact area (d). The nonlinearity is mainly visible in the derivative (e). Parameter values: (b-e) $k_s m_L^{max}/(k_{on}^R c_R^0) = 0.5$. (a-c) $r_{max}/\rho_0 = 2^{1/3}$ corresponding to a contact angle of $\pi/2$ (hemispheric) and (c-e) $\rho_0 = 5\,\mu m$, such that the three diffusion length scales (b-e) correspond to $l_D = \{0.1, 1, 10\}\mu m$. Other parameter values as given in Tab. 2.1.

Tab. 2.1)

$$m_{RL} = m_L^{max}\left(1 - \frac{k_s + k_-}{k_+ m_R^0 M_R}\right) + \mathcal{O}\left(\left(\frac{k_s + k_-}{k_+ m_R^0}\right)^2\right). \tag{2.29}$$

Together with Eqs.(2.2),(2.9) follows then for the normalized receptor surface density

$$0 = \frac{l_{D,f}}{r}\frac{\partial}{\partial r}\left(r\frac{\partial M_R}{\partial r}\right) + 1 - M_R - \frac{k_s m_L^{max}}{k_{on}^R c_R^0} - \frac{k_-(k_- + k_s)}{k_{off}^R k_+ m_R^0 M_R}\frac{m_L^{max}}{m_R^0}. \tag{2.30}$$

In accordance with expansion Eq. (2.29) for small $(k_\mathrm{s} + k_-)/(k_+ m_\mathrm{R}^0)$, the last term can be considered negligible. This is further justified considering the typically slow unbinding rate k_- (Tab. 2.1). For radially symmetric systems Eq. (2.30) is then solved by

$$M_\mathrm{R} = 1 - \frac{k_\mathrm{s} m_\mathrm{L}^\mathrm{max}}{k_\mathrm{on}^\mathrm{R} c_\mathrm{R}^0} + \mathcal{C}_3 I_0 \left(r/l_\mathrm{D,f}\right). \tag{2.31}$$

Note that this limit is only valid if $k_\mathrm{s} m_\mathrm{L}^\mathrm{max}/(k_\mathrm{on}^\mathrm{R} c_\mathrm{R}^0) < 1$, otherwise the solution contains regions with negative concentrations. Compared to Eq. (2.27), where the loss of receptor molecules due to signaling was completely neglected, it enters here as a constant contribution uniformly acting as a sink across the whole contact site, proportional to the cleavage rate k_s and total surface density of ligands $m_\mathrm{L}^\mathrm{max}$. The integration constants of Eqs. (2.18),(2.31) derived from the boundary conditions Eqs. (2.23),(2.24) result in lengthy expressions [Appendix D, Eq. 5.12], which depend on the relative length scales $l_\mathrm{D,f}/\rho_0$ and r_max/ρ_0, and the ratio between cleavage and transport of new receptors to the surface $k_\mathrm{s} m_\mathrm{L}^\mathrm{max}/(k_\mathrm{on}^\mathrm{R} c_\mathrm{R}^0)$.

The additional loss of receptors due to signaling at the contact site compared to the free surface leads to non-uniform steady state receptor densities [Fig. 2.5(a,b)]. Because $(k_\mathrm{s} + k_-)/(k_+ m_\mathrm{R}^0) \ll 1$ in the receptor excess limit, most ligands are bound by receptors [Fig. 2.2] and the non-uniform receptor distributions translate into rather uniform distribution of receptor-ligand complexes [Fig. 2.5(a)], leading to uniform production of signaling molecules across the contact site and a nearly linear scaling between maximum ligand density and the number of signaling molecules [Fig. 2.5(c)]. For small diffusion length scales $l_\mathrm{D} \ll r_\mathrm{max}$, profiles are uniform at the free and contact surface with a sharp transition at the contact line [Fig. 2.5(b)], and when l_D and ρ_0 are of the same order of magnitude, loss of molecules at the contact site can also deplete the receptors at the free surface [Fig. 2.5(b)]. Even for non-uniform distributions of receptor-ligand complexes [Fig. 2.5(b), right], scaling between the contact area and the bulk concentration of signaling molecules is nearly linear [Fig. 2.5(d,e)]. Moreover, the signal increases weakly with the diffusion length—especially at large contacts—due to a diffusive flux of receptors from the free to the contact surface.

Limit 3: fast cleavage rate

Another limit to consider are systems where the sum of the cleavage and the unbinding rate of receptor-ligand complex $k_\mathrm{s} + k_-$ is fast compared to the receptor binding rate such that only a small fraction of ligands is found in a bound state at a given time point, i.e.

$$k_\mathrm{s} + k_- \gg k_+ m_\mathrm{R}^0. \tag{2.32}$$

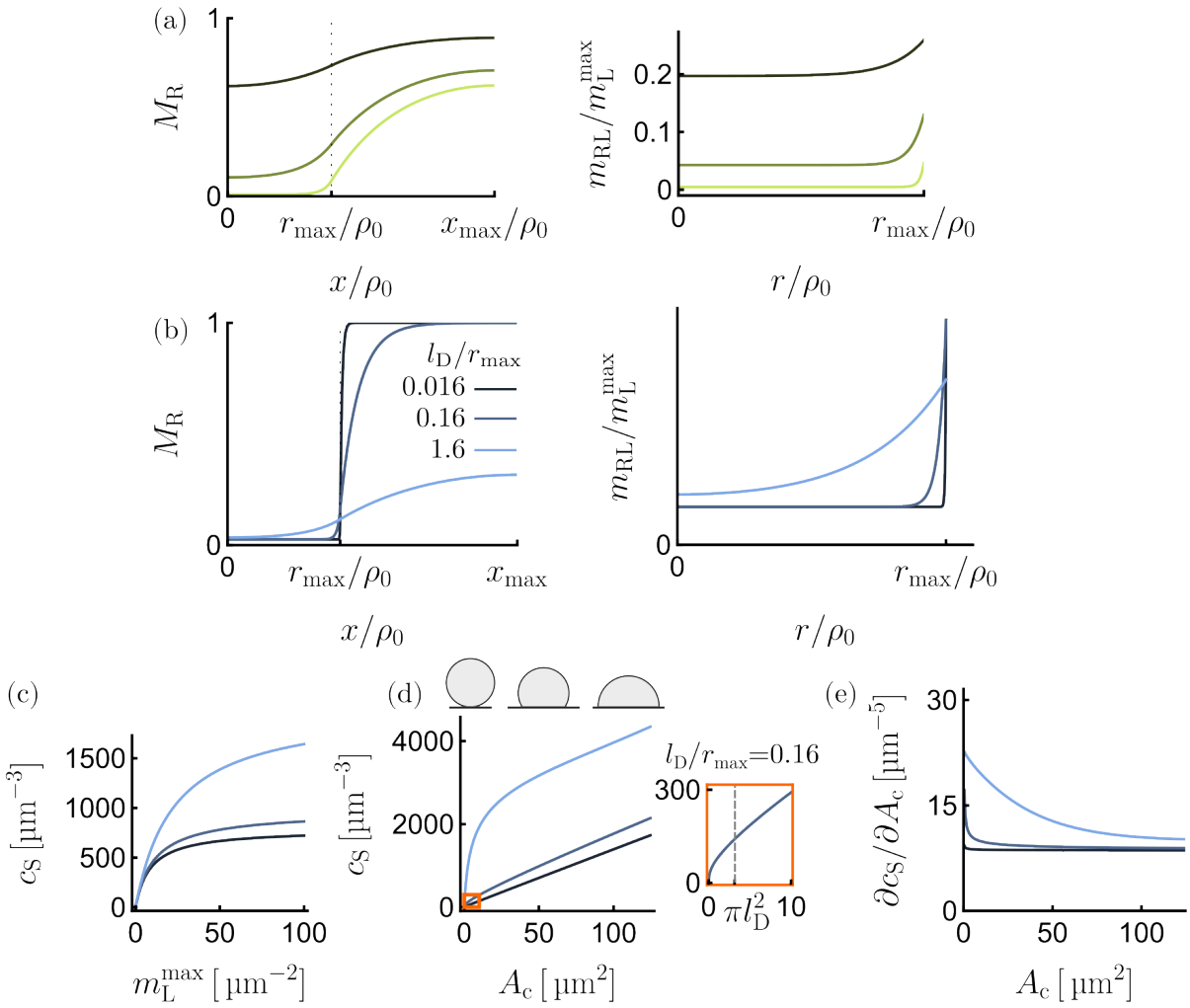

Figure 2.6. Limit of fast cleavage rate. (a) The normalized distribution of surface receptors (left) and receptor-ligand complexes (right) for varying degree of receptor loss at the contact due to signaling, $\frac{k_+ k_s m_L^{max}}{(k_s+k_-)k_{off}^R} = \{1, 10, 100\}$ (dark to light green), $l_D/r_{max} = 0.16$. (b-e) Varying the diffusion length scale alters the surface densities of receptors (b, left) and receptor-ligand complexes (b, right). (c) Signals increase with ligand density and plateau in the regime where recruitment of new receptors is limited by diffusion. (d, e) Scaling between signals and contact area has two regimes, a nonlinear ($r_{max} < \pi l_D$) and a linear regime ($r_{max} > \pi l_D$). Parameter values: (a-c) $r_{max}/\rho_0 = 2^{1/3}$ corresponding to a contact angle of $\pi/2$ (hemispheric) and (c-e) $\rho_0 = 5\,\mu m$, such that the three diffusion length scales (b-e) correspond to $l_D = \{0.1, 1, 10\}\mu m$, $k_s = 34$ in accordance with the fast cleavage limit [Eq. (2.32)], $m_L^{max} = 10\,\mu m^{-2}$. Other parameter values as given in Tab. 2.1.

Note that the reference density m_R^0—the steady state surface density without any physical contact—is an upper limit for the concentration of surface receptors, because the signaling process is removing additional molecules from the system. The example values reported in Tab. 2.1 do not fall into this limit, however, it could be appropriate for systems with

lower receptor concentrations (smaller m_{R}^0), weaker receptor-ligand interactions (smaller k_+/k_-) or faster conversion of the receptor-ligand complex into a signaling molecule (larger k_{s}), for instance when cleavage does not depend on the recruitment of another enzyme.

In this limit, Eq. (2.17) can be simplified to

$$0 = \frac{l_{\mathrm{D,f}}^2}{r}\frac{\partial}{\partial r}\left(r\frac{\partial M_{\mathrm{R}}}{\partial r}\right) + 1 - \left(1 + \frac{k_+ k_{\mathrm{s}} m_{\mathrm{L}}^{\max}}{(k_{\mathrm{s}} + k_-)k_{\mathrm{off}}^{\mathrm{R}}}\right) M_{\mathrm{R}}, \tag{2.33}$$

where the term in the right brackets contains information about the number of receptor molecules lost through signaling compared to receptors internalized back into the bulk. The loss of receptor molecules due to signaling thus enters as a term proportional to the surface density of receptors. The solution is

$$M_{\mathrm{R}} = \frac{1}{1 + \dfrac{k_+ k_{\mathrm{s}} m_{\mathrm{L}}^{\max}}{(k_{\mathrm{s}} + k_-)k_{\mathrm{off}}^{\mathrm{R}}}} + \mathcal{C}_4 I_0\left(r/l_{\mathrm{D,c}}\right) \tag{2.34}$$

with

$$l_{\mathrm{D,c}} = \frac{l_{\mathrm{D,f}}}{\sqrt{1 + \dfrac{k_+ k_{\mathrm{s}} m_{\mathrm{L}}^{\max}}{(k_{\mathrm{s}} + k_-)k_{\mathrm{off}}^{\mathrm{R}}}}} \tag{2.35}$$

a length scale containing information about the diffusion distance of a receptor molecule at the contact site before it is removed from the surface due to endocytosis or ligand binding and cleavage. The integration constant $\mathcal{C}_4$ of Eq. (2.34) can be derived together with $\mathcal{C}_1$ [Eq. (2.19)] from boundary conditions Eqs. (2.23),(2.24) and Eq. (2.21) [Appendix D, Eq. 5.14]. They depend on the relative length scales $r_{\max}/\rho_0$, $l_{\mathrm{D,f}}/\rho_0$ and the loss term [Eq. (2.33), right bracket]. Given the parameter values in Tab. 2.1, the binding and cleavage rate are much faster than the internalization (endocytosis) of receptors and the steady state receptor density at the contact site is close to zero [Fig. 2.6(a), left]. Due to the high cleavage (or unbinding) rate, only a small fraction of ligands is bound in receptor-ligand complexes [Fig. 2.6(a), right]. The signal increases with the ligand density until the receptors at the surface are depleted and signaling is limited by the diffusion of unbound receptors from the free to the contact surface [Fig. 2.6(c)]. Signals scale nearly linear with the diffusion length and finally plateau for $l_{\mathrm{D}} > \rho_0$, either because receptors at the free and contact surface are depleted or–for small contacts—because all ligands at the contact are saturated with bound receptors [Fig. 2.6(b)]. The right panel in Fig. 2.6(d) shows the scaling between signal molecule concentration and contact area for a cell of radius $\rho_0 = 5\,\mu\mathrm{m}$ with a contact radius $r_{\max} = 5 \times 2^{1/3}\mu\mathrm{m}$ (i.e. a contact angle of $\pi/2$) and a diffusion length $l_{\mathrm{D}} = 1\,\mu\mathrm{m}$ (i.e. $l_{\mathrm{D}}/r_{\max} \approx 0.16$). One can distinguish two regimes, where signals increase more strongly with contact area if $r_{\max} < l_{\mathrm{D}}$ and

converge to a linear scaling law for $r_{\max} > {}_{\mathrm{D}}$. Indeed, *in vitro* experiments measuring Notch signals at cell-cell contacts revealed a roughly linear relation between the Notch signaling response and the contact area [74].

In conclusion, the Notch signaling pathway exhibits a unique feature in which receptor molecules are irreversibly lost during the signaling process, effectively making the cell surface a sink for receptors. Given parameter values reported in the literature (Tab. 2.1), this molecular depletion is typically non-negligible (Limit 1), leading to non-uniform steady state distributions of free receptor molecules. However, when receptors are expressed in excess and the majority of ligands are sequestered in signaling complexes, the overall signal scales nearly linearly with the contact area, despite spatially heterogeneous receptor distributions (Limit 2). A notable departure from this behavior occurs under conditions of rapid receptor-ligand complex turnover, such as in the case of a high cleavage rate (Limit 3), or when ligands are in excess—as can be achieved in *in vitro* experiments [122]. Under these conditions, the distribution of receptor-ligand complexes follows radial gradients strong enough to induce significant nonlinear scaling between the bulk signaling molecule concentration and the contact area.

2.2.2 Active processes at the contact line

In living cells, additional regulatory processes controlling the transport of receptor and ligand molecules, for instance at the contact line, can produce molecular gradients [127, 128], which motivates to treat the boundary of the contact domain as a free parameter. In the following, I thus consider the receptor concentration at the contact line $M_{\mathrm{R}}|_{\partial\Gamma_{\mathrm{c}}}$ as a fixed control parameter and discuss the steady state solutions at the contact site. Because signaling molecules are only produced at the contact, the free surface plays no role for their bulk concentration. For fixed boundary concentration, the solutions of the normalized steady state receptor density in the three limits are: Limit 1 [Eq. (2.26)]

$$M_{\mathrm{R}} = 1 + \left(M_{\mathrm{R}}|_{\partial\Gamma_{\mathrm{c}}} - 1\right) \frac{I_0\left(r/l_{\mathrm{D,f}}\right)}{I_0\left(r_{\max}/l_{\mathrm{D,f}}\right)}, \tag{2.36}$$

Limit 2 [Eq. (2.30)]

$$M_{\mathrm{R}} = \left(1 - \frac{k_{\mathrm{s}} m_{\mathrm{L}}^{\max}}{k_{\mathrm{on}}^{\mathrm{R}} c_{\mathrm{R}}^{0}}\right) + \left(M_{\mathrm{R}}|_{\partial\Gamma_{\mathrm{c}}} - \left(1 - \frac{k_{\mathrm{s}} m_{\mathrm{L}}^{\max}}{k_{\mathrm{on}}^{\mathrm{R}} c_{\mathrm{R}}^{0}}\right)\right) \frac{I_0\left(r/l_{\mathrm{D,f}}\right)}{I_0\left(r_{\max}/l_{\mathrm{D,f}}\right)}, \tag{2.37}$$

Limit 3 [Eq. (2.33)]

$$M_{\mathrm{R}} = \frac{1}{1 + \dfrac{k_{+} k_{\mathrm{s}} m_{\mathrm{L}}^{\max}}{(k_{\mathrm{s}} + k_{-}) k_{\mathrm{off}}^{\mathrm{R}}}} + \left(M_{\mathrm{R}}|_{\partial\Gamma_{\mathrm{c}}} - \frac{1}{1 + \dfrac{k_{+} k_{\mathrm{s}} m_{\mathrm{L}}^{\max}}{(k_{\mathrm{s}} + k_{-}) k_{\mathrm{off}}^{\mathrm{R}}}}\right) \frac{I_0\left(r/l_{\mathrm{D,c}}\right)}{I_0\left(r_{\max}/l_{\mathrm{D,c}}\right)}. \tag{2.38}$$

In the low ligand density limit [Eq. (2.25)], the fixed boundary concentration induces non-uniform receptor profiles with surface densities increasing or decreasing towards the boundary depending on the ratio between $M_{\mathrm{R}}|_{\Gamma_{\mathrm{c}}}$ and m_{R}^{0} [Fig. 2.7(a)]. When the contact radius is small compared to the free diffusion length $l_{\mathrm{D,f}}$, receptor profiles are nearly uniform. Similarly, contact areas much larger than the diffusion length scale have nearly uniform receptor profiles except for the regime close to the contact line. However, because most ligands are bound at steady state, signals scale nearly linearly with the contact size and independent of the boundary concentration [Eq. (2.7)(a)]. Similarly, non-uniform receptor profiles in the limit 2 [Eq. (2.55)] lead to a nearly linear relation between signals and contact area and a weak dependence on the boundary concentration [Fig. 2.7(b)]. In limit 3, due to the fast depletion of molecules at the contact site, receptor densities are close to zero except near the contact line due to the limitless supply of receptors from the boundary. Because the production of signaling molecules at the surface j_{s} is proportional to m_{RL} [Eq. (2.48)], the majority of signaling molecules are produced close to the boundary, and signals scale nonlinearly with contact area. For large contacts $r_{\max} \gg l_{\mathrm{D}}$, the area in which most signaling occurs scales approximately with $\sim 2\pi l_{\mathrm{D,c}} r_{\max}$, thus, $c_{\mathrm{S}} \sim \sqrt{A_{\mathrm{c}}}$.

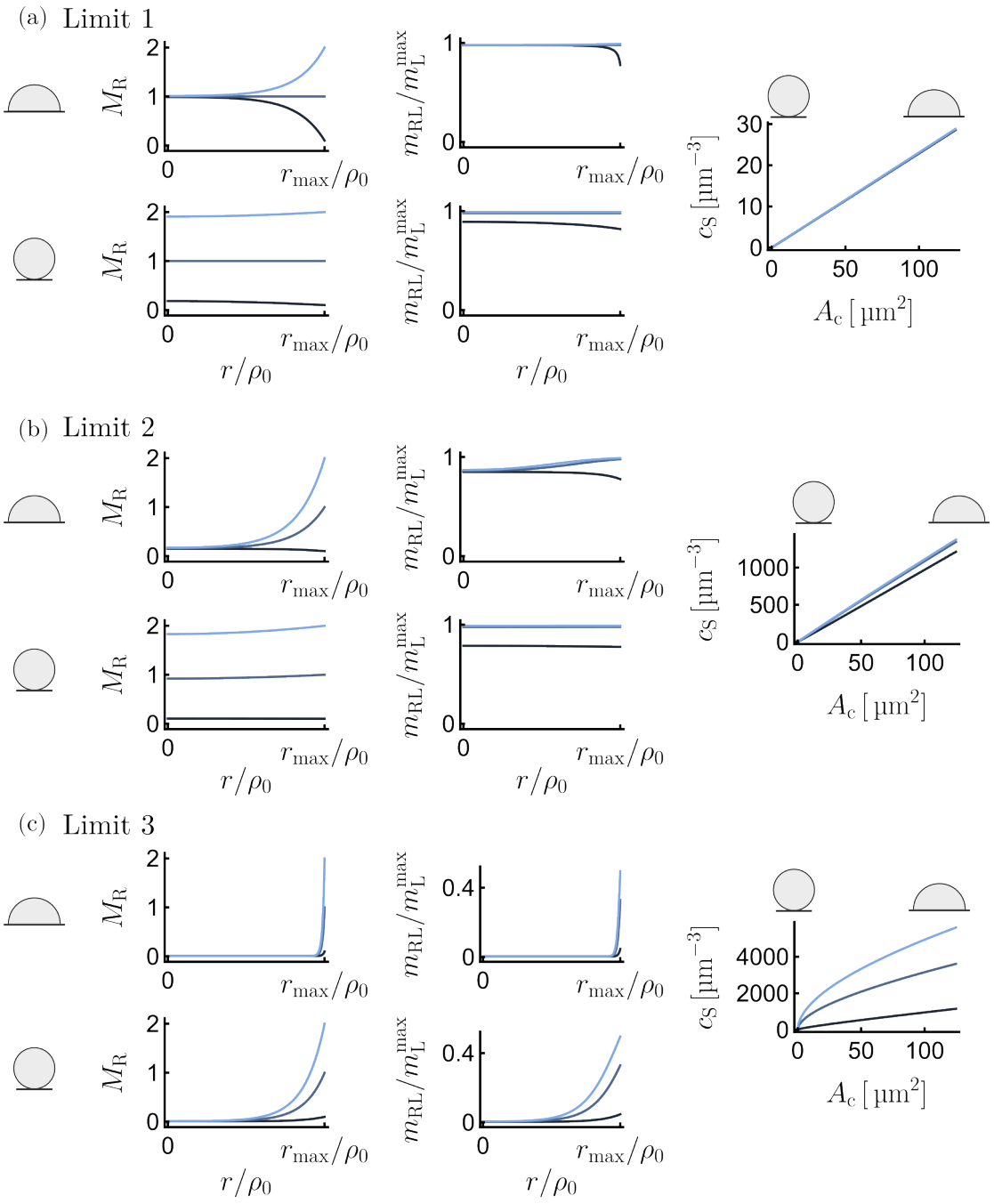

Figure 2.7. Active regulation at the contact line. (a, b) In the limits of low ligand density (a) and receptor excess (b), fixed receptor concentrations at the contact line ($M_R|_{\Gamma_c} = \{0.1, 1, 2\}$ dark to light blue) induce non-uniform receptor distributions, but translate into nearly uniform receptor-ligand complex distribution and linear scaling between signals and contact area due to saturation of available ligands. (c) In the fast cleavage limit, the diffusive flux of molecules from the boundary induces a strong, nonlinear contact area dependence of signals. For (a-c), top row corresponds to a contact radius $r_{max}/\rho_0 = 5 \times 2^{1/3}$, bottom row $r_{max}/\rho_0 = 0.1$, $l_D/\rho_0 = 0.2$ everywhere. Other parameter values as listed in Tab. 2.1.

Dynamically changing bulk concentrations

In the previous sections, I analyzed the distribution of receptors and signaling complexes at the surface under the assumption of a constant bulk concentration of receptors [Eq. (2.15)]. However, in most cells, proteins and other functional molecules are constantly produced and degraded, leading to temporal variations of the cytoplasmic concentration. In the following, I consider a constant production and decay rate of receptors in the bulk [Eq. (2.5)] and discuss how the surface-bulk coupling influences the bulk and surface densities of receptors, receptor-ligand complexes and signaling molecules for varying contacts. To isolate the effects of surface-bulk coupling from the diffusive flow and patterning dynamics within the surface, I assume in the following that the contact line separating the free and contact surfaces forms a diffusive barrier, i.e. that no molecules can diffuse laterally between the surfaces. This assumption substantially simplifies the calculations, and indeed diffusion barriers based on protein structures associated with the membrane, the lipid composition or extreme curvatures—as given at the contact line—have been found to impede diffusive transport on cellular membranes [129, 130]. The boundary conditions for the surface densities on the two domains then are

$$(\mathbf{n}\cdot\nabla)m|_{\partial\Gamma_\mathrm{f}} = 0 \tag{2.39}$$

$$(\mathbf{n}\cdot\nabla)m|_{\partial\Gamma_\mathrm{c}} = 0 \tag{2.40}$$

in which $\partial\Gamma_\mathrm{f}, \partial\Gamma_\mathrm{c}$ denote the contact line. From Eqs. (2.2),(2.6) follows at steady state $j|_{\Gamma_\mathrm{f}} = 0$ and the uniform steady state bulk concentration

$$c = \frac{k_\mathrm{p}}{k_\mathrm{d}} - \frac{1}{k_\mathrm{d}V}\int_{\Gamma_\mathrm{c}} j dA \tag{2.41}$$

only depends on processes in the bulk and at the contact site Γ_c. Considering typical parameter values (Tab 2.1), the rate of receptors binding to ligands on the substrate is large compared to the transport of receptors from the surface into the bulk, i.e.

$$k_+ m_\mathrm{L}^\mathrm{max} \gg k_\mathrm{off}^\mathrm{R}. \tag{2.42}$$

In this limit, solutions of Eq. (2.13) are uniform and follow

$$m_\mathrm{R} = \frac{k_\mathrm{on}^\mathrm{R} c_\mathrm{R}(k_- + k_\mathrm{s})}{k_+(k_\mathrm{s} m_\mathrm{L}^\mathrm{max} - k_\mathrm{on}^\mathrm{R} c_\mathrm{R})}, \tag{2.43}$$

under boundary condition Eq. (2.40). The bulk and surface densities of receptors are coupled via the flux [Eq. (2.41)]

$$j_\mathrm{R} = k_\mathrm{on}^\mathrm{R} c_\mathrm{R} - k_\mathrm{off}^\mathrm{R} m_\mathrm{R}. \tag{2.44}$$

Using Eq. (2.43) and assuming (2.25), the flux can be approximated as $j_\mathrm{R} = k_\mathrm{on}^\mathrm{R} c_\mathrm{R}$ and the steady state bulk and surface densities of receptors that follow from Eqs. (2.41) and (2.43) are given by

$$c_\mathrm{R} = \frac{k_\mathrm{p}^\mathrm{R} V}{k_\mathrm{d}^\mathrm{R} V + k_\mathrm{on}^\mathrm{R} A_\mathrm{c}}, \tag{2.45}$$

$$m_\mathrm{R} = \frac{k_\mathrm{on}^\mathrm{R} k_\mathrm{p}^\mathrm{R} (k_- + k_\mathrm{s}) V}{k_+ [k_\mathrm{s} m_\mathrm{L}^\mathrm{max} (k_\mathrm{on}^\mathrm{R} A_\mathrm{c} + k_\mathrm{d}^\mathrm{R} V) - k_\mathrm{on}^\mathrm{R} k_\mathrm{p}^\mathrm{R} V]}. \tag{2.46}$$

For Notch receptors, reported values are $k_+ = 0.167\,\mu\mathrm{m}^2\,\mathrm{s}^{-1}$ and $k_\mathrm{off}^\mathrm{R} = 0.02\,\mathrm{s}^{-1}$ [74] and Notch activation assays with cells on ligand-coated substrates are performed with surface densities of up to $m_\mathrm{L}^\mathrm{max} \approx 10^5\,\mu\mathrm{m}^{-2}$ [122], which justifies limit (2.42) and allows to neglect the $k_\mathrm{off}^\mathrm{R}$-term in Eq. (2.13). Importantly, m_R and c_R have upper bounds: in the absence of ligands ($m_\mathrm{L}^\mathrm{max} = 0$), the steady state receptor density is uniform at $m_\mathrm{R}^0 = k_\mathrm{on}^\mathrm{R} c_\mathrm{R}^0 / k_\mathrm{off}^\mathrm{R}$ with bulk concentration $c_\mathrm{R}^0 = k_\mathrm{p}^\mathrm{R} / k_\mathrm{d}^\mathrm{R}$. Because receptors are removed upon receptor-ligand binding and subsequent cleavage, m_R^0 and c_R^0 are upper bounds to the steady state concentrations. If I estimate the term in brackets of Eq. (2.13) using $m_\mathrm{R} = m_\mathrm{R}^0$ and typical parameter values as listed in Tab. 2.1, neglecting $k_\mathrm{off}^\mathrm{R}$ is valid if $m_\mathrm{L}^\mathrm{max} \gg 10\,\mu\mathrm{m}^{-2}$. Given Eqs. (2.12) and (2.46), the steady state density of receptor-ligand complexes is

$$m_\mathrm{RL} = \frac{k_\mathrm{on}^\mathrm{R} k_\mathrm{p}^\mathrm{R} V}{k_\mathrm{s} (k_\mathrm{on}^\mathrm{R} A_\mathrm{c} + k_\mathrm{d}^\mathrm{R} V)}. \tag{2.47}$$

The bulk concentration of signaling molecules follows Eq. (2.41), without a bulk production term ($k_\mathrm{p}^\mathrm{S} = 0$) and with flux $j_\mathrm{S} = -k_\mathrm{s} m_\mathrm{RL}$, arising from the cleavage of receptor-ligand molecules at the surface. The steady state bulk concentration is given by

$$c_\mathrm{S} = \frac{k_\mathrm{on}^\mathrm{R} k_\mathrm{p}^\mathrm{R} A_\mathrm{c}}{k_\mathrm{d}^\mathrm{S} (k_\mathrm{on}^\mathrm{R} A_\mathrm{c} + k_\mathrm{d}^\mathrm{R} V)}. \tag{2.48}$$

This relation shows how the received signal depends on the receptor-ligand kinetics, the volume, and the geometry of the adherent cell. In particular, it demonstrates that a nonlinear relation between signal molecule concentration and contact area arises from surface-bulk coupling due to the additional loss of receptor molecules in the signaling process. For sufficiently large contacts (and high ligand density [Eq. (2.42)]), the loss of receptors at the surface dominates over the turnover in the bulk and the signal molecule concentration $c_\mathrm{S} = k_\mathrm{p}^\mathrm{R} / k_\mathrm{d}^\mathrm{S}$ is independent of the contact area and limited by the total amount of receptors available in the system.

2.2.3 Signaling interactions between contacting cells

In this section, I consider receptor-ligand interactions at the interface between two cells indexed with $i, j \in \{1, 2\}$ [Fig. 2.8]. Each cell produces receptors as well as ligands, which

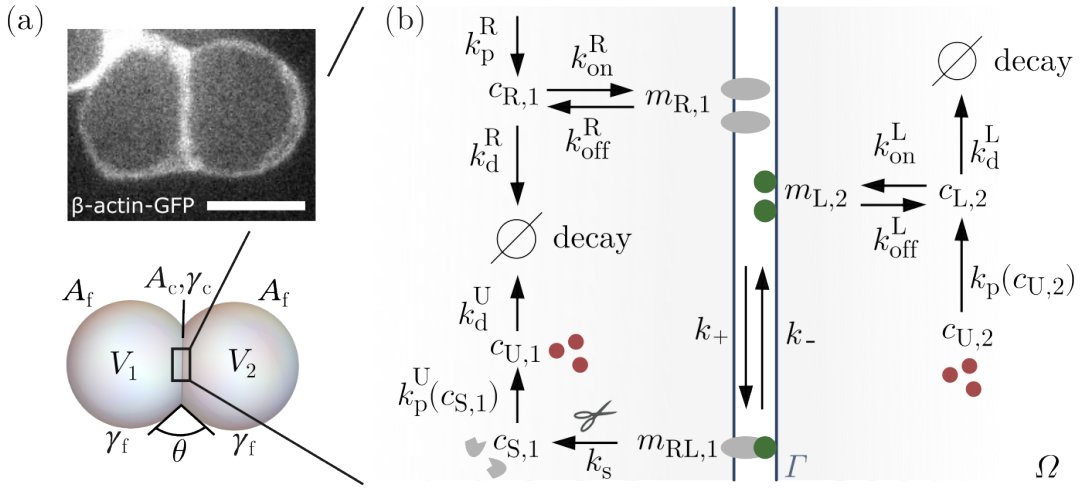

Figure 2.8. Microscopic details of cell-cell signaling. (a) Schematics of a cell pair with a shared interface with fixed volumes V and uniform interfacial tensions γ_c, γ_f conjugate to interfacial areas A_c, A_f. Fluorescence microscopy image shows a pair of zebrafish sensory cells exchanging Notch signals across their contact surface (adapted from [68]). Scale bar: 5 µm. (b) Contact-dependent signals are exchanged at the cell-cell contact. Receptor (R, gray) and ligand (L, green) molecules bind across the interface and form receptor-ligand complexes (RL). Both receptors and ligands are produced in the bulk and exchanged with the surface. Receptor-ligand complexes are cleaved irreversibly [70], which releases a signaling molecule (S, gray) into the bulk. Regulator molecules (U, red) are produced with a rate depending on the bulk concentration of signal molecules, and in turn determine the production rate of new ligands (Section 2.3.1). The remaining part of the RL complex is degraded after cleavage [70]. Here, c and m denote bulk and surface concentrations respectively, and k denote the kinetic rates of the reactions.

exchange between bulk and surface—ligands are not substrate-bound with fixed positions as I considered in the preceding part. The receptors on the surface of cell i bind to the ligands on the surface of the other cell j and vice versa, producing respectively oriented receptor-ligand complexes. Upon cleavage they release signal molecules into the receptor-carrying cell i. Contrary to the way I treated substrate-bound ligands in the preceding section, ligands at the droplet interface are not released after cleavage of the receptor-ligand complexes, but are degraded together with the remaining receptor fragment instead [131]. While some literature suggests that ligands can also be recycled after a signaling event or enter alternative signaling pathways [132, 133], I here consider that receptors and ligands are always degraded after cleavage. Signaling molecules control the production of regulator molecules as before, which feed back onto the production terms. In line with the typical molecular mechanisms in Notch signaling, I consider an active regulation of

ligand production [70]. As explained in Section 2.1, the steady state bulk concentrations of receptor, ligand, signaling, and regulator molecules are uniform within each cell with a value set by the flux balance condition [Eq. (2.41)]. To capture the reaction-diffusion dynamics at the interface, I use Eq. (2.2) for receptors, ligands, and complexes with the reaction terms [74]

$$\mathcal{R}_{\mathrm{R}} = k_{\mathrm{on}}^{\mathrm{R}} c_{\mathrm{R},i} - (k_{\mathrm{off}}^{\mathrm{R}} + k_{+} m_{\mathrm{L},j}) m_{\mathrm{R},i} + k_{-} m_{\mathrm{RL},i}, \tag{2.49}$$

$$\mathcal{R}_{\mathrm{L}} = k_{\mathrm{on}}^{L} c_{\mathrm{L},j} - (k_{\mathrm{off}}^{\mathrm{L}} + k_{+} m_{\mathrm{R},i}) m_{\mathrm{L},j} + k_{-} m_{\mathrm{RL},i}, \tag{2.50}$$

$$\mathcal{R}_{\mathrm{RL}} = k_{+} m_{\mathrm{R},i} m_{\mathrm{L},j} - (k_{-} + k_{\mathrm{s}}) m_{\mathrm{RL},i}, \tag{2.51}$$

with rate constants as described in Section 2.2.1. Under boundary condition Eq. (2.40), steady state solutions of Eq. (2.2) for the densities of receptors, ligands and receptor-ligand complexes with the reaction terms Eqs. (2.49)-(2.51) are uniform and follow the relations

$$m_{\mathrm{R},i} = \frac{k_{\mathrm{on}}^{\mathrm{R}} c_{\mathrm{R},i} (k_{\mathrm{s}} + k_{-})}{k_{\mathrm{off}}^{\mathrm{R}} (k_{\mathrm{s}} + k_{-}) + k_{+} k_{\mathrm{s}} m_{\mathrm{L},j}}, \tag{2.52}$$

$$m_{\mathrm{L},j} = \frac{k_{\mathrm{on}}^{\mathrm{L}} c_{\mathrm{L},j} (k_{\mathrm{s}} + k_{-})}{k_{\mathrm{off}}^{\mathrm{L}} (k_{\mathrm{s}} + k_{-}) + k_{+} k_{\mathrm{s}} m_{\mathrm{R},i}}. \tag{2.53}$$

Ligand molecules are only produced in the bulk, but not at the surface, thus, the steady state concentrations of bulk and surface densities have the upper limits $c_{\mathrm{L}}^{0} = k_{\mathrm{p}}^{\mathrm{L}}/k_{\mathrm{d}}^{\mathrm{L}}$ and $m_{\mathrm{L}}^{0} = k_{\mathrm{on}}^{\mathrm{L}} c^{0}/k_{\mathrm{off}}^{\mathrm{L}}$. Together with Eqs. (2.52) and (2.41) for the receptor bulk concentration, one can define a lower limit for the surface density of receptors

$$m_{\mathrm{R}}^{\mathrm{min}} = \frac{k_{\mathrm{on}}^{\mathrm{R}} k_{\mathrm{off}}^{\mathrm{L}} (k_{-} + k_{\mathrm{s}}) k_{\mathrm{p}}^{\mathrm{R}} k_{\mathrm{d}}^{\mathrm{L}} V}{k_{\mathrm{on}}^{\mathrm{L}} k_{+} k_{\mathrm{s}} k_{\mathrm{p}}^{\mathrm{L}} (k_{\mathrm{on}}^{\mathrm{R}} A_{\mathrm{c}} + k_{\mathrm{d}}^{\mathrm{R}} V) + k_{\mathrm{d}}^{\mathrm{L}} k_{\mathrm{off}}^{\mathrm{R}} (k_{-} + k_{\mathrm{s}}) k_{\mathrm{d}}^{\mathrm{R}} V}. \tag{2.54}$$

In line with Khait et al. 2016 [74], I consider that cells produce an excess of receptors compared to the number of ligands, i.e. $k_{\mathrm{p}}^{\mathrm{R}} \gg k_{\mathrm{p}}^{\mathrm{L}}$, and similar to limit (2.25) for the single cell I assume that the endocytosis rate of ligands is small compared to the rate of binding

$$k_{+} m_{\mathrm{R}}^{\mathrm{min}} \gg k_{\mathrm{off}}^{\mathrm{L}}, \tag{2.55}$$

allowing me to neglect the $k_{\mathrm{off}}^{\mathrm{L}}$-term in Eq. (2.50). The bulk and surface densities of ligands are coupled in Eq. (2.41) via the flux

$$j_{\mathrm{L},j} = k_{\mathrm{on}}^{\mathrm{L}} c_{\mathrm{L},j} - k_{\mathrm{off}}^{\mathrm{L}} m_{\mathrm{L},j}, \tag{2.56}$$

which using Eq. (2.53) and assuming (2.55) can be written as $j_{\mathrm{L,j}} = k_{\mathrm{on}}^{\mathrm{L}} c_{\mathrm{L,j}}$. In this limit, solving Eq. (2.2) with the reaction terms Eqs. (2.49)–(2.51) under boundary condition

Eq. (2.40) together with Eq. (2.41) and boundary flux Eq. (2.44) for the bulk density of receptors yields

$$c_{\mathrm{R},i} = \frac{k_{\mathrm{p}}^{\mathrm{R}}(k_{\mathrm{on}}^{\mathrm{L}}A_{\mathrm{c}} + k_{\mathrm{d}}^{\mathrm{L}}V) - k_{\mathrm{p}}^{\mathrm{L}}k_{\mathrm{on}}^{\mathrm{L}}A_{\mathrm{c}}}{k_{\mathrm{d}}^{\mathrm{R}}(k_{\mathrm{on}}^{\mathrm{L}}A_{\mathrm{c}} + k_{\mathrm{d}}^{\mathrm{L}}V)}, \tag{2.57}$$

$$c_{\mathrm{L},j} = \frac{k_{\mathrm{p}}^{\mathrm{L}}V}{k_{\mathrm{on}}^{\mathrm{L}}A_{\mathrm{c}} + k_{\mathrm{d}}^{\mathrm{L}}V}, \tag{2.58}$$

$$m_{\mathrm{R},i} = \frac{A_{\mathrm{c}}k_{\mathrm{on}}^{\mathrm{L}}k_{\mathrm{on}}^{\mathrm{R}}(k_{\mathrm{p}}^{\mathrm{R}} - k_{\mathrm{p}}^{\mathrm{L}}) + (k_{\mathrm{d}}^{\mathrm{L}}k_{\mathrm{on}}^{\mathrm{R}}k_{\mathrm{p}}^{\mathrm{R}} - k_{\mathrm{d}}^{\mathrm{R}}k_{\mathrm{on}}^{\mathrm{L}}k_{\mathrm{p}}^{\mathrm{L}})V}{k_{\mathrm{d}}^{\mathrm{R}}k_{\mathrm{off}}^{\mathrm{R}}(k_{\mathrm{on}}^{\mathrm{L}}A_{\mathrm{c}} + k_{\mathrm{d}}^{\mathrm{L}}V)}, \tag{2.59}$$

$$m_{\mathrm{L},j} = \frac{k_{\mathrm{on}}^{\mathrm{L}}k_{\mathrm{p}}^{\mathrm{L}}k_{\mathrm{d}}^{\mathrm{R}}k_{\mathrm{off}}^{\mathrm{R}}(k_{-} + k_{\mathrm{s}})V}{k_{+}k_{\mathrm{s}}(A_{\mathrm{c}}k_{\mathrm{on}}^{\mathrm{L}}k_{\mathrm{on}}^{\mathrm{R}}(k_{\mathrm{p}}^{\mathrm{R}} - k_{\mathrm{p}}^{\mathrm{L}}) + (k_{\mathrm{d}}^{\mathrm{L}}k_{\mathrm{on}}^{\mathrm{R}}k_{\mathrm{p}}^{\mathrm{R}} - k_{\mathrm{d}}^{\mathrm{R}}k_{\mathrm{on}}^{\mathrm{L}}k_{\mathrm{p}}^{\mathrm{L}})V)}, \tag{2.60}$$

$$m_{\mathrm{RL},i} = \frac{k_{\mathrm{on}}^{\mathrm{L}}k_{\mathrm{p}}^{\mathrm{L}}V}{k_{\mathrm{s}}(k_{\mathrm{on}}^{\mathrm{L}}A_{\mathrm{c}} + k_{\mathrm{d}}^{\mathrm{L}}V)}. \tag{2.61}$$

The steady state bulk concentration of signaling molecules following Eq. (2.41) with $j_{\mathrm{S}} = -k_{\mathrm{s}}m_{\mathrm{RL}}$ and $k_{\mathrm{p}}^{\mathrm{S}} = 0$ as before is

$$c_{\mathrm{S},i} = \frac{k_{\mathrm{on}}^{\mathrm{L}}k_{\mathrm{p}}^{\mathrm{L}}A_{\mathrm{c}}}{k_{\mathrm{d}}^{\mathrm{S}}(k_{\mathrm{on}}^{\mathrm{L}}A_{\mathrm{c}} + k_{\mathrm{d}}^{\mathrm{L}}V)}. \tag{2.62}$$

Similar to Eq. (2.48), this relation shows how the signal exchanged between interacting cells depends on the receptor-ligand kinetics and the geometry of the cells. Contrary to Eq. (2.48), the signal depends on the rate constants concerning turnover and transport of ligands instead of receptors—expressing the ligand-limited case. Indeed, studies of Notch signaling pairs of cells suggest that cells possess an excess of receptors compared to ligands [74].

2.2.4 Modulation of interfacial tensions by adhesion

Cells produce integrin and cadherin molecules that form transmembrane complexes to adhere to external structures or other cells [Section 1.2.2] [48, Chapter 19]. To derive how the kinetics of such adhesion molecules change the coarse-grained interfacial tension at contact surfaces, I consider droplets containing adhesion molecules N with a bulk concentration c_{N}, in contact either with an external substrate, or with another droplet [Fig. 2.9]. At a droplet-substrate interface, these molecules can adhere to the substrate with a surface density m_{N} [Fig. 2.9(a)], whereas at a droplet-droplet interface, molecules from the two droplets bind to each other and form complexes with surface concentration m_{NN} [Fig. 2.9(b)]. Similar problems are discussed in [47, 49, 134, 135, 136].

Tension at the contact interface of a droplet wetting a solid substrate

I first derive the adaptive adhesion term for a contact surface between a fluid droplet and a solid substrate, to which adhesion molecules can bind [Fig. 2.9(a)]. A mass-action

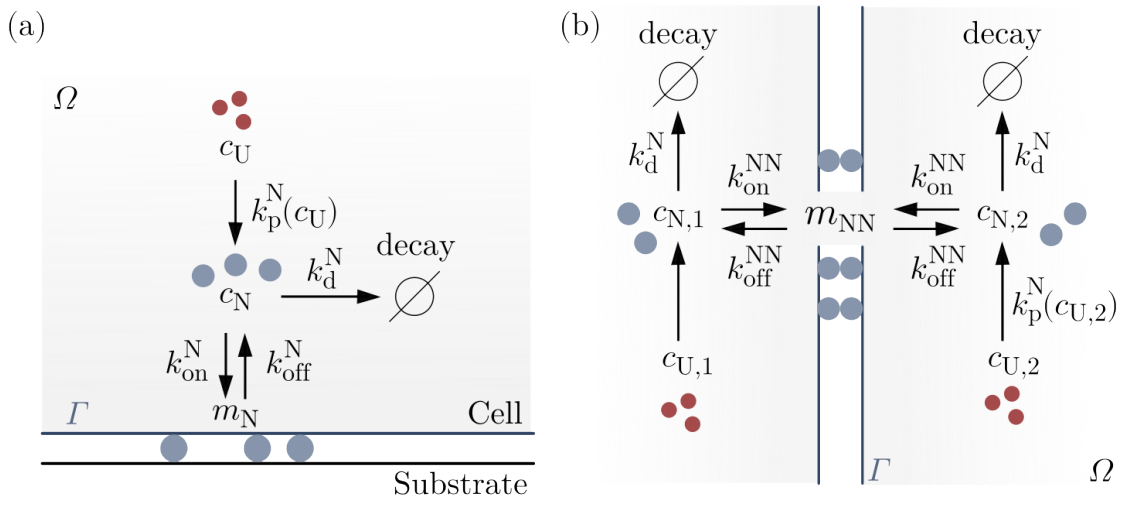

Figure 2.9. Adhesion molecules (N, blue) are exchanged between bulk and surface and form complexes at the cell-substrate (a) or across the cell-cell interface (b), which reduce the surface energy. The rate of adhesion molecule production due to transcriptional regulation depends on the regulator concentration c_U (red) (Section 2.3.1); decay rates are constant. In general, c and m denote bulk and surface concentrations respectively, and k denote the kinetic rates of the reactions.

based reaction term for the surface concentration Eq. (2.2) of adhesion molecules reads

$$\mathcal{R}_{m_N} = k_{on}^N (m_N^{max} - m_N) c_N - k_{off}^N m_N \tag{2.63}$$

with m_N^{max} the density of available binding sites at the contact. The flux coupling bulk and contact surface is $j_N = \mathcal{R}_{m_N}$ and adhesion molecules bound to the substrate are fixed in place, i.e. $D_{m_N} = 0$ in Eq. (2.2). At steady state, it follows from Eqs. (2.2), (2.41),(2.63) and boundary condition Eq. (2.40) that $j_N = 0$, $c_N = k_p^N/k_d^N$, and

$$m_N = \frac{k_{on}^N k_p^N}{k_{on}^N k_p^N + k_{off}^N k_d^N} m_N^{max}. \tag{2.64}$$

The same expression can also be derived from the grand canonical ensemble (Appendix F). Expansion in the dilute limit $k_{on}^N k_p^N / k_d^N \ll k_{off}^N$, i.e. where saturation effects do not play a role, yields

$$m_N = \frac{k_{on}^N k_p^N}{k_{off}^N k_d^N} m_N^{max} + \mathcal{O}\left(\left(\frac{k_{on}^N k_p^N}{k_{off}^N k_d^N} \right)^2 \right). \tag{2.65}$$

Given that each adhesion complex reduces the surface energy by ϵ [137], the surface tension at a contact site [Fig. 2.1(a)] in this limit is

$$\gamma_c = \gamma_0 - \epsilon \frac{k_{on}^N k_p^N}{k_{off}^N k_d^N} m_N^{max}, \tag{2.66}$$

with γ_0 a baseline tension that contains all other components of the interfacial tension.

Tension at the interface between two droplets

At contact surfaces between two droplets, adhesion molecules produced within the droplets can bind across the interface and form adhesion complexes with surface density m_{NN} [Fig. 2.9(d)] [53]. Taking exclusion effects into account, adhesion complexes can only form at unoccupied sites on the interface. The density of unoccupied sites is $(m_{\mathrm{NN}}^{\mathrm{max}} - m_{\mathrm{NN}})$ with $m_{\mathrm{NN}}^{\mathrm{max}}$ the maximum possible density of adhesion complexes. The reaction term for the density of adhesion complexes is then

$$\mathcal{R}_{m_{\mathrm{NN}}} = k_{\mathrm{on}}^{\mathrm{NN}}(m_{\mathrm{NN}}^{\mathrm{max}} - m_{\mathrm{NN}})c_{\mathrm{N},1}c_{\mathrm{N},2} - k_{\mathrm{off}}^{\mathrm{NN}}m_{\mathrm{NN}} \tag{2.67}$$

with indices $\{1, 2\}$ labeling the two droplets. The flux coupling bulk and surface densities is $j_{\mathrm{NN}} = \mathcal{R}_{m_{\mathrm{NN}}}$, and the tension at the droplet-droplet interface in the dilute limit $k_{\mathrm{on}}^{\mathrm{NN}}(k_{\mathrm{p}}^{\mathrm{N}}/k_{\mathrm{d}}^{\mathrm{N}})^2 \ll k_{\mathrm{off}}^{\mathrm{NN}}$ is

$$\gamma_{\mathrm{c}} = \gamma_0 - \epsilon\frac{k_{\mathrm{on}}^{\mathrm{NN}}}{k_{\mathrm{off}}^{\mathrm{NN}}}\left(\frac{k_{\mathrm{p}}^{\mathrm{N}}}{k_{\mathrm{d}}^{\mathrm{N}}}\right)^2 m_{\mathrm{NN}}^{\mathrm{max}}. \tag{2.68}$$

Indeed, the force necessary to separate two adhesive cells has been shown to scale linearly with the squared total number of adhesion molecules [137, 138]. In general, the kinetic rates of adhesion molecules can differ between contacting cells, subject to internal regulatory mechanisms. In Section 2.3.3, I analyse the case in which the production rate of adhesion molecules $k_{\mathrm{p}}^{\mathrm{N}}$ depends on a cell-intrinsic signaling state.

2.3 Mechanochemical feedback between adhesion and cell-cell signaling

In response to external signals, cells typically change their gene expression through transcription factors and transcriptional regulators, thereby controlling the production rates of diverse proteins, including adhesion and signaling molecules [48, Chapter 7]. Responding to shape-dependent signals, and feeding back onto both mechanics and signaling, these internal regulatory states couple the processes described in Sections. 2.2.4 and 2.2. In the following, I derive the macroscopic equations that govern the evolution of such internal states, taking into account how the received signals depend on contact geometry, and how the contact geometry in turn is set by adaptive adhesion. In particular, from the microscopic kinetics of adhesion and signaling molecules (Sections.2.2.4, 2.2) I obtain two macroscopic feedback parameters: the *signal susceptibility* χ determines how the contact area affects the magnitude of transmitted signals, and the *adaptive adhesion coefficient* γ_{A} controls how the received signals feed back onto the contact mechanics [Fig. 1.3].

2.3.1 Evolution of a macroscopic signaling state

I introduce a macroscopic internal cell state variable that responds to area-dependent biochemical signals defined by the uniform bulk concentration of a regulator molecule U– representing for instance a transcription factor. The bulk concentration c_U is governed by Eq. (2.6) with $j_\mathrm{U} = 0$, and I assume that the effective production rate of regulator molecules depends on the steady state concentration of signal molecules $k_\mathrm{p}^\mathrm{U}(c_\mathrm{s})$—the more signal molecules are present, the more regulator molecules are produced [Figs. 2.1, 2.8]. The regulation of genes and the synthesis of new proteins involve multiple steps and molecular intermediates, which lead to the presence of nonlinear effects like cooperative binding and multimerization, commonly captured using Hill functions [139]. Similar to previous studies modeling canonical Notch signaling [67, 68, 99, 140], I therefore assume that steady state concentrations of U are bounded within a range $c_\mathrm{U}^\mathrm{min} \leq c_\mathrm{U} \leq c_\mathrm{U}^\mathrm{max}$ and I consider a nonlinear production rate with Hill coefficient h

$$k_\mathrm{p}^\mathrm{U}(c_\mathrm{S}) = \frac{1}{\tau_\mathrm{u}} \left(c_\mathrm{U}^\mathrm{min} + \frac{(c_\mathrm{U}^\mathrm{max} - c_\mathrm{U}^\mathrm{min})}{1 + \left(\frac{c_\mathrm{S}^\mathrm{crit}}{c_\mathrm{S}}\right)^h} \right), \tag{2.69}$$

in which $\tau_\mathrm{u} = 1/k_\mathrm{d}^\mathrm{U}$ is the characteristic time scale on which c_U is changing, and $c_\mathrm{S}^\mathrm{crit}$ is the critical concentration at the inflection point.
The saturating response to the received signal [Eq. (2.69)] permits introducing a dimensionless *signaling state* variable

$$u := \frac{c_\mathrm{U} - c_\mathrm{U}^\mathrm{min}}{c_\mathrm{U}^\mathrm{max} - c_\mathrm{U}^\mathrm{min}}, \tag{2.70}$$

normalized to the response range such that $u \in [0, 1]$. Eqs. (2.6), (2.69), and (2.70) together with the definition of a normalized received signal

$$s = c_\mathrm{S}/c_\mathrm{S}^\mathrm{crit} \tag{2.71}$$

lead to a dynamical equation for the evolution of the internal state

$$\tau_\mathrm{u} \frac{du}{dt} = \sigma(s) - u, \tag{2.72}$$

with sigmoidal response function [Fig. 2.10]

$$\sigma(s) = \frac{s^h}{1 + s^h}. \tag{2.73}$$

Given that the regulation of protein concentrations through transcriptional changes requires tens of minutes to hours and can vary greatly between different protein species [114, 115], I assume that the timescale associated with the regulator turnover τ_u dominates the dynamics of the system. On this timescale, I assume that bulk and surface

concentrations relax to their steady state solutions. In cells, concentration and shape dynamics are indeed typically at least an order of magnitude faster—set by diffusive, biochemical, and viscoelastic timescales which are on the order of seconds to minutes [74, 114, 116, 117]. In the following sections, I discuss how the internal state dynamics govern the production of adhesion and ligand molecules.

2.3.2 Signal susceptibility

In general, the received signal (2.71) depends nonlinearly on the size of the contact area, i.e. $s(A_\mathrm{c})$ according to e.g. Eqs. (2.48) or (2.62). When the number of receptors that are recruited to the surface and lost in the signaling process is small compared to the turnover of molecules in the bulk, I can expand the bulk concentration of signal molecules [Eq. (2.48),(2.62)], and obtain a relation that is linear in the contact area. In the limit in which receptors interact with an excess of ligands [Eq. (2.25)], e.g. for the single cell on the functionalized substrate, the expression reads

$$c_\mathrm{S} = \frac{k_\mathrm{p}^\mathrm{R} k_\mathrm{on}^\mathrm{R} A_\mathrm{c}}{k_\mathrm{d}^\mathrm{S} k_\mathrm{d}^\mathrm{R} V} + \mathcal{O}\left(\left(\frac{k_\mathrm{on}^\mathrm{R} A_\mathrm{c}}{k_\mathrm{d}^\mathrm{R} V}\right)^2\right). \tag{2.74}$$

Indeed, *in vitro* experiments revealed a roughly linear relation between the Notch signaling response and the contact area, including for large contacts [74]. The received signal [Eq. (2.71)] can then be written as

$$s = \chi \frac{A_\mathrm{c}}{A_0}, \tag{2.75}$$

in which I introduced the *signal susceptibility*

$$\chi = \frac{k_\mathrm{p}^\mathrm{R} k_\mathrm{on}^\mathrm{R}}{c_\mathrm{S}^\mathrm{crit} k_\mathrm{d}^\mathrm{S} k_\mathrm{d}^\mathrm{R} V} A_0 \tag{2.76}$$

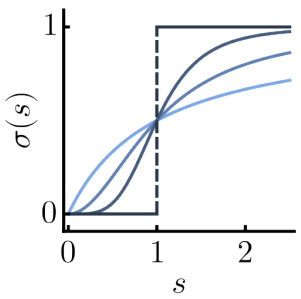

Figure 2.10. Signals s are processed with a sigmoidal response function (Hill function Eq. (2.73)). In the limit $h \to \pm\infty$, the response is a step function: Light to dark blue: $h = \{1, 2, 4, \infty\}$.

using the definition of the volume-dependent reference area $A_0 = (3V/2)^{2/3}\pi^{1/3}$. The volume-dependence of the susceptibility arises because the degradation of molecules in the bulk scales with the volume, and due to the reference area A_0, yielding a scaling of $\chi \propto V^{-1/3}$. However, in cells where protein degradation does not increase with the cell volume, the signal susceptibility might increase with volume. One can estimate the order of magnitude of the susceptibility [Eq. (2.76)] using $k_{\mathrm{on}}^{\mathrm{R}} k_{\mathrm{p}}^{\mathrm{R}}/k_{\mathrm{d}}^{\mathrm{R}} = 2\,\mu\mathrm{m}^{-2}\,\mathrm{s}^{-1}$ [74], $V = 500\,\mu\mathrm{m}^3$, $k_{\mathrm{d}}^{\mathrm{S}} = 5 \times 10^{-3}\,\mathrm{min}^{-1}$ [141, 142] and $c_{\mathrm{S}}^{\mathrm{crit}} = 1000/V$ [120] yielding $\chi \sim 3000$.

Signal-dependent production of ligands

Mutually inhibitory Notch signals typically lead to a decrease in the production rate of ligands in response to received signals [70, 143]. I therefore consider that the production rate of ligands is a monotonously *decreasing* function of the regulator concentration c_{U}. I assume that no ligands are produced at $c_{\mathrm{U}} = c_{\mathrm{U}}^{\max}$, i.e. $k_{\mathrm{p}}^{\mathrm{L}}(c_{\mathrm{U}}^{\max}) = 0$, and I expand $k_{\mathrm{p}}^{\mathrm{L}}$ to first order around $c_{\mathrm{U}}^{\max}$

$$k_{\mathrm{p}}^{\mathrm{L}}(c_{\mathrm{U}}) = \left.\frac{dk_{\mathrm{p}}^{\mathrm{L}}}{dc_{\mathrm{U}}}\right|_{c_{\mathrm{U}}^{\max}} (c_{\mathrm{U}} - c_{\mathrm{U}}^{\max}) + \mathcal{O}\left((c_{\mathrm{U}} - c_{\mathrm{U}}^{\max})^2\right). \tag{2.77}$$

Using the definition of u [Eq. (2.70)] it follows that

$$k_{\mathrm{p}}^{\mathrm{L}}(u) = \left(- \left.\frac{dk_{\mathrm{p}}^{\mathrm{L}}}{dc_{\mathrm{U}}}\right|_{c_{\mathrm{U}}^{\max}} \right) (c_{\mathrm{U}}^{\max} - c_{\mathrm{U}}^{\min})(1-u). \tag{2.78}$$

Linearizing the bulk concentration of signal molecules [Eq. (2.62)] as before, I obtain

$$c_{\mathrm{S},i} = \frac{k_{\mathrm{p}}^{\mathrm{L}} k_{\mathrm{on}}^{\mathrm{L}} A_{\mathrm{c}}}{k_{\mathrm{d}}^{\mathrm{S}} k_{\mathrm{d}}^{\mathrm{L}} V} + \mathcal{O}\left(\left(\frac{k_{\mathrm{on}}^{\mathrm{L}} A_{\mathrm{c}}}{k_{\mathrm{d}}^{\mathrm{L}} V}\right)^2\right), \tag{2.79}$$

with which the signal $s_{ij} = c_{\mathrm{s},i}/c_{\mathrm{s}}^{\mathrm{crit}}$ received by cell i from cell j is

$$s_{ij} = \chi \frac{A_{\mathrm{c}}}{A_0}(1 - u_j) \tag{2.80}$$

with the signal susceptibility in the ligand-limited case given by

$$\chi = \frac{k_{\mathrm{on}}^{\mathrm{L}} A_0 (c_{\mathrm{U}}^{\max} - c_{\mathrm{U}}^{\min})}{c_{\mathrm{S}}^{\mathrm{crit}} k_{\mathrm{d}}^{\mathrm{S}} k_{\mathrm{d}}^{\mathrm{L}} V} \left(- \left.\frac{dk_{\mathrm{p}}^{\mathrm{L}}}{dc_{\mathrm{U}}}\right|_{c_{\mathrm{U}}^{\max}} \right) \tag{2.81}$$

The expression of the susceptibility is similar to Eq. (2.76), but depends on the production, decay and transport rates of ligands rather than receptors. While Eq. (2.76) holds when receptors interact with an excess of ligands [Eq. (2.25)], an excess of receptors compared to ligands [Eq. (2.55)] leads to Eq. (2.81). In the ligand-limited case, contributions

to the susceptibility can be further distinguished based on properties of the signal *sending* cell, specifically $k_\mathrm{p}^\mathrm{L} k_\mathrm{on}^\mathrm{L}/k_\mathrm{d}$, and properties of the signal *receiving* cell, including $c_\mathrm{s}^\mathrm{crit}$ and k_d^S [144]. In particular, instead of Eq. (2.80), one can define the signal as

$$s_{ij} = \phi\chi\frac{A_\mathrm{c}}{A_0}(1-u_j), \tag{2.82}$$

where ϕ contains all contributions from the *sending cell*, i.e. the *overall available signal*, and the susceptibility χ only the contributions from the receiving cell.
Interestingly, the signal susceptibility is independent of the cleavage rate k_s. A common experimental perturbation to Notch signaling is the pharmacological inhibition of the enzyme cleaving the receptor-ligand complexes (treatment of cells with γ-secretase inhibitors) [145]. Our result suggests that the signal susceptibility and thus the steady state concentration of signaling molecules is independent of k_s unless cleavage is completely prevented.

2.3.3 Signal-dependent active mechanics and the adaptive adhesion coefficient

In many biological systems, for instance mechanosensory epithelia [68, 81, 146] or synthetically engineered systems [52], adhesion molecules are expressed downstream of contact-based signals. Accordingly, I consider that the production rate of adhesion molecules $k_\mathrm{p}^\mathrm{N}(c_\mathrm{U})$ is a monotonously increasing function of the regulator concentration [Fig. 2.9(c)]. I assume that k_p^N vanishes for $c_\mathrm{U} \leq c_\mathrm{U}^\mathrm{min}$, i.e. no adhesion molecules are produced when the regulator concentration drops below a concentration $c_\mathrm{U}^\mathrm{min}$, and I linearize k_p^N around $c_\mathrm{U}^\mathrm{min}$

$$k_\mathrm{p}^\mathrm{N}(c_\mathrm{U}) = \left.\frac{dk_\mathrm{p}^\mathrm{N}}{dc_\mathrm{U}}\right|_{c_\mathrm{U}^\mathrm{min}} (c_\mathrm{U} - c_\mathrm{U}^\mathrm{min}) + \mathcal{O}\left((c_\mathrm{U} - c_\mathrm{U}^\mathrm{min})^2\right). \tag{2.83}$$

With Eq. (2.70), the surface tension at the contact site of a single cell with an underlying substrate [Eq. (2.66)] can then be written as

$$\gamma_\mathrm{c} = \gamma_0 - \gamma_\mathrm{A} u \tag{2.84}$$

where I define the *adaptive adhesion coefficient*

$$\gamma_\mathrm{A} = \epsilon\frac{k_\mathrm{on}^\mathrm{N}(c_\mathrm{U}^\mathrm{max} - c_\mathrm{U}^\mathrm{min})}{k_\mathrm{off}^\mathrm{N} k_\mathrm{d}^\mathrm{N}} \left.\frac{dk_\mathrm{p}^\mathrm{N}}{dc_\mathrm{U}}\right|_{c_\mathrm{U}^\mathrm{min}} m_\mathrm{L}^\mathrm{max}. \tag{2.85}$$

Similarly, the tension at the interface between two contacting cells Eq. (2.68) is

$$\gamma_\mathrm{c} = \gamma_0 - \gamma_\mathrm{A} u_1 u_2, \tag{2.86}$$

with

$$\gamma_{\mathrm{A}} = \epsilon \frac{k_{\mathrm{on}}^{\mathrm{NN}} (c_{\mathrm{U}}^{\mathrm{max}} - c_{\mathrm{U}}^{\mathrm{min}})^2}{k_{\mathrm{off}}^{\mathrm{NN}} (k_{\mathrm{d}}^{\mathrm{N}})^2} \left(\frac{dk_{\mathrm{p}}^{\mathrm{N}}}{dc_{\mathrm{U}}} \bigg|_{c_{\mathrm{U}}^{\mathrm{max}}} \right)^2 m_{\mathrm{NN}}^{\mathrm{max}}. \tag{2.87}$$

Eqs. (2.84) and (2.86) are identical except for the squared terms arising from the production and decay of adhesion molecules, because both cells need to contribute molecules for the formation of adhesion complexes at their shared interface [Fig. 2.9(b)].

The adaptive adhesion coefficient γ_{A} has units of energy per area. The tension at cellular surfaces is usually dominated by the active contractility of the actomyosin cortex and is on the order of 0.05–0.5 $\mathrm{nN\,\mu m^{-1}}$ [147, 148, 149, 150, 151]. The tension at a cell-cell or cell-substrate interface can be inferred from the contact angle if the tension at the free surface γ_{f} is known [152]. For instance, for $\gamma_{\mathrm{f}} = 0.1\,\mathrm{nN\,\mu m^{-1}}$, a range of contact angles θ =10-100° corresponds to interfacial tensions of approx. 0.13–0.2 $\mathrm{nN\,\mu m^{-1}}$. Combined fluorescence-based density measurements of the adhesion molecule E-cadherin in *C.elegans* embryos suggests that changes in the interfacial tension γ_{c} due to expression of adhesion molecules—as described by the adaptive adhesion term—are up to 0.41 $\mathrm{nN\,\mu m^{-1}}$ [147], demonstrating that regulation of adhesion molecule expression provides access to a large range of shape configurations. Assuming a lateral distance of $\sim$ 10 nm between adhesion molecules [153], i.e. a surface density of 10.000 $\mathrm{\mu m^{-2}}$, the effective surface energy per adhesion molecule would be $\epsilon \approx 4 \times 10^{-17}$ J—several orders larger than $k_{\mathrm{B}}T$. Indeed, adhesion complexes in cells interact with different molecules and their formation depends also on anchoring to the cytoskeleton, which itself exhibits complex dynamics and feedback effects [46, 50, 53, 127], thus ϵ corresponds to an effective energy per adhesion complex that captures more than just the binding energy between two adhesion molecules.

2.3.4 Equilibrium shapes of cells with uniform interfacial tensions

Equations (2.75),(2.80) and (2.84),(2.86) respectively describe how transmitted signals depend on the area of the cell-cell or cell-substrate interface, and how the interfacial tension in turn depends on the internal states. Given that the mechanochemical dynamics are dominated by the slowest timescale τ_{u}, set by transcriptional regulation, the contact areas across which signals are exchanged are determined quasi-instantaneously by the conjugate interfacial tension γ_{c}. Neglecting any non-uniform contributions to the surface tensions, I assume that the cell shapes can be approximated by minimal surface configurations, i.e. that minimize the effective surface energy of N coupled, incompressible

droplets [Eq. (1.3)]. In the minimal surface configuration, the droplets acquire spherical-cap shapes with contact areas given by Eq. (1.7). Indeed, biological cells have been found in minimal surface configurations in many contexts [Figs. 2.1(a), 2.8], including [53, 68, 147, 148, 150, 154].

2.4 Outlook: Macroscopic dynamics of mechanochemical droplets

Starting from microscopic equations, I have derived a macroscopic framework [Eqs. (2.72), (2.75), (2.80),(2.84), (2.86) and (1.7)] describing the mechanochemical dynamics of shape-adaptive cells, governed by two feedback parameters that couple shape changes to signaling (susceptibility χ) and signaling to shape adaptation (adhesion coefficient γ_{A}) [Fig. 1.3(a)]. By employing a minimal set of parameters and internal states, this framework enables a tractable exploration of shape and state dynamics, allowing for a systematic identification of critical points that mark transitions in dynamic behavior.
In the following chapter, using a combination of linear stability analysis, simulations, and numerical continuation, I analyze the dynamical states emerging from the interplay between shape changes and signaling. Specifically, I show how the positive feedback between contact-dependent signals and area-increasing adhesion can produce multiple stable wetting states, and I explain how it lowers the threshold susceptibility for symmetry-breaking of internal states in interacting droplet pairs. Moreover, for large adaptive adhesion coefficients I show that mechanochemical feedback can drive excitability and self-sustained oscillations of shapes and internal states.

Chapter 3

Macroscopic feedback dynamics

The macroscopic equations (2.72),(2.75),(2.80),(2.84),(2.86) and (1.7) describe the mechanochemical dynamics of shape-adaptive cells, with two feedback parameters that couple shape changes to signaling (susceptibility χ) and signaling to shape adaptation (adhesion coefficient γ_{A}), which I have derived from microscopic relations (Chapter 2). Using a combination of linear stability analysis, simulations, and numerical continuation (Appendix G) for details), I analyze the dynamical states emerging from the interplay between shape changes and signaling. In particular, I demonstrate how positive feedback between contact-dependent signaling and adhesion-driven area expansion can induce shape bistability, giving rise to multiple stable wetting states for individual droplets on functionalized substrates. In the context of interacting cell pairs, this feedback mechanism lowers the threshold susceptibility required for symmetry-breaking of internal states. Furthermore, for sufficiently large adaptive adhesion coefficients, I demonstrate that mechanochemical feedback can lead to excitability, giving rise to self-sustained oscillations in both shape and internal states. I show that the underlying critical points and bifurcation structures are topologically equivalent to those found in conductance-based models of neuronal excitation, highlighting an interesting parallel between signal processing in neurons and mechanochemical signal processing through adaptive shape change. Lastly, I explore how variations in mechanical and signaling properties influence the feedback-driven dynamics.

3.1 Shape-dependent feedback creates bistability

Equations (2.72),(2.75),(2.84), and (1.7) describe the dynamics of the signaling state u and contact area A_{c} of the single, adherent cell.

Depending on the combination of feedback parameters χ and γ_{A} relative to the tension ratio $(\gamma_0 - \gamma_{\mathrm{m}})/\gamma_{\mathrm{f}}$, Eq. (2.72) has either one or two stable steady state solutions u^* [Fig. 3.1(a)]. Using numerical continuation, I find a bistable regime above a critical

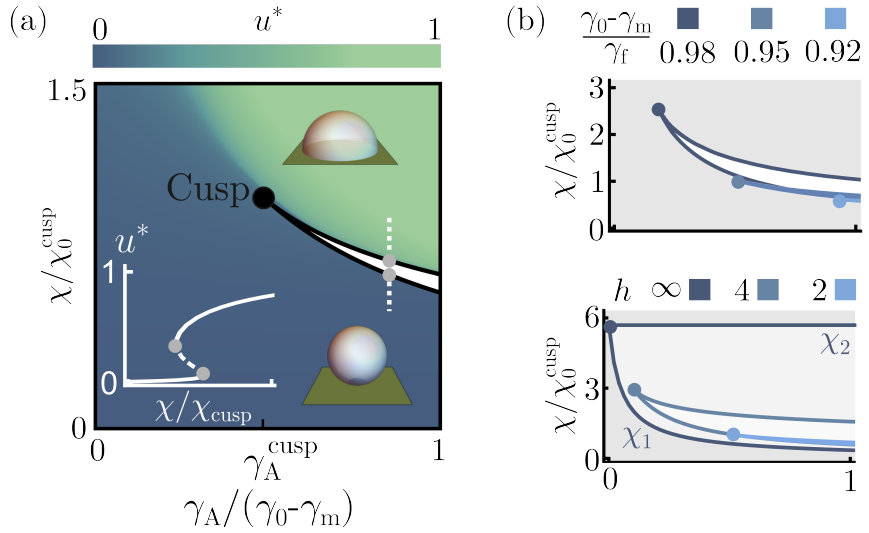

Figure 3.1. Adaptive adhesion leads to bistability. (a) The parameter diagram, derived via numerical continuation (Appendix G), contains a bistable regime (white) bounded by saddle-node bifurcations (black lines) converging in a codimension-2 cusp point, separating regimes of strong and weak substrate wetting. (b) The size of the bistable regime increases with the tension ratio $(\gamma_0 - \gamma_{\rm m})/\gamma_{\rm f}$ (top) and with the Hill coefficient h of the nonlinear response function [Eq. (2.73)] (bottom) ($\chi_0^{\rm cusp}$: reference susceptibility at cusp for $(\gamma_0 - \gamma_{\rm m})/\gamma_{\rm f} = 0.95$, $h = 2$). Parameter values for each diagram listed in Appendix J.

value of the adaptive adhesion coefficient $\gamma_A^{\rm cusp}$ where two saddle-node bifurcation lines (SN) emerge from a cusp bifurcation point [Fig. 3.1(a)]. For $\gamma_{\rm A} > \gamma_A^{\rm cusp}$ and small χ, the only stable solution is a configuration with small contact area $A_{\rm c}$, correspondingly weak signal transmission and a low signaling state u. For values of χ above the lower SN line, a second stable configuration appears with large contact area $A_{\rm c}$, which permits a stronger signaling interaction with the substrate and a larger signaling state u [Fig. 3.1(a), inset]. This latter configuration is accessible only when the positive feedback between signaling and adaptive mechanics is sufficiently strong. The position of the cusp point within the feedback-parameter diagram, and the size of the associated bistable regime depends on the tension ratio $(\gamma_0 - \gamma_{\rm m})/\gamma_{\rm f}$, and on the Hill coefficient h in the response function [Eq. (2.73)]—increasing either of the two parameters lowers the threshold adaptive adhesion coefficient $\gamma_A^{\rm cusp}$ [Fig. 3.1(b)]. I find bistability for $h \geq 2$.

In the limit $h \to \infty$, i.e. where the internal states respond to signals in a step-wise manner [Fig. 2.10], one can derive a simple relation between χ and γ_A for the two saddle-node lines [Fig. 3.1(c)]. In this limit, the only possible stable steady state solutions of Eq. (2.72) are $u^* \in \{0; 1\}$ and the corresponding surface tensions at the contact site are $\gamma_c \in \{\gamma_0; \gamma_0 - \gamma_A\}$ [Eq. (2.84)]. For small values of χ, signaling is weak and the only stable steady state is $u^* = 0$ with a small contact area set by $\gamma_c = \gamma_0$. The second stable

steady state $u^* = 1$ appears for

$$s(A_c|_{\gamma_c=\gamma_0-\gamma_A}) \geq 1. \tag{3.1}$$

For

$$s(A_c|_{\gamma_c=\gamma_0}) > 1, \tag{3.2}$$

the configuration with small contact area and $u = 0$ is no longer a steady state solution and $u^* = 1$ remains the only stable steady state. From conditions (3.1)–(3.2) together with Eq. (2.75) follows that the critical susceptibilities at the saddle-node lines delineating the bistable regime are given by

$$\chi_1 = \frac{A_0}{A_c|_{\gamma_c=\gamma_0-\gamma_A}} \tag{3.3}$$

and

$$\chi_2 = \frac{A_0}{A_c|_{\gamma_c=\gamma_0}}. \tag{3.4}$$

for the lower and upper lines respectively [Fig. 3.1(c)]. It shows that bifurcation curves simply scale with the inverse of the steady state contact area, and it confirms that the transition between the bistable regime and the single stable strong wetting state (upper SN line) is independent of the adaptive adhesion coefficient (χ_2).

3.2 Symmetry-breaking of internal states

Next, I study the dynamics of cell pairs exchanging mutually inhibitory signals Eqs. (2.72), (2.80), (2.86) and (1.7). Strong mutually inhibitory interactions generically lead to spontaneous symmetry-breaking, whereby initially small differences between interacting units diverge to low- and high-value steady states [155], a mechanism relevant for the patterning of different cell types [143]. Using numerical continuation, I find that in the state-diagram of feedback parameters the regimes of uniform and symmetry-broken steady states are separated by a line of supercritical pitchfork bifurcations (PF) [Fig. 3.2(a)]. Below the critical value χ_{PF}, inhibition is not strong enough to produce symmetry-breaking, and the cell pair converges to identical low internal states with a small contact area. Linear stability analysis shows that this critical susceptibility scales approximately inversely with the interfacial area $\chi_{PF} \sim A_0/A_c$ (Appendix H)—indicating that the adaptive adhesion promotes symmetry-breaking: starting from low, nearly identical internal states, the active term in Eq. (2.68) transiently expands the contact area as the trajectory approaches a saddle in the phase space of internal states [Fig. 3.2(a), inset].

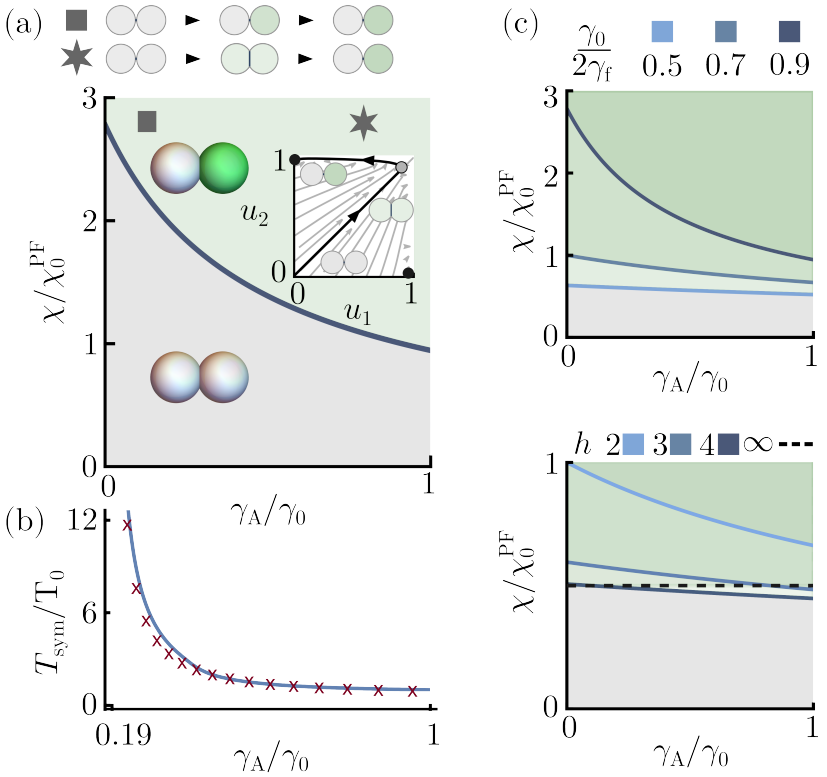

Figure 3.2. Adaptive adhesion promotes symmetry-breaking. (a) Mutually inhibitory interactions between the signaling states of contacting droplets lead to symmetry-breaking via a line of pitchfork bifurcations (PF), separating uniform (gray) and symmetry broken (green) steady states. Adaptive adhesion promotes symmetry-breaking by transiently increasing the contact area across which mutually inhibitory signals are exchanged (inset: filled black circle: stable steady state, filled gray circle: saddle). (b) The relaxation time to the symmetry-broken steady state T_{sym} (blue curve), is dominated by the inverse of the maximum saddle eigenvalue (red crosses) and decreases with increasing γ_A, because the larger transient interface allows for the exchange of stronger signals promoting symmetry-breaking ($\chi/\chi_0^{PF} = 2$, T_0: reference relaxation time for $\gamma_A/\gamma_0 = 1$), (Appendix H for further details). (c) The baseline tension ratio $\gamma_0/2\gamma_f$ (top) and the Hill coefficient h of the nonlinear response function [Eq. (2.73)] (bottom) determine how the critical susceptibility changes with the adaptive adhesion coefficient (χ_0^{PF}: reference susceptibility at PF for $\gamma_A = 0$, $\gamma_0/2\gamma_f = 0.7$, $h = 2$). Parameter values for each diagram listed in Appendix J.

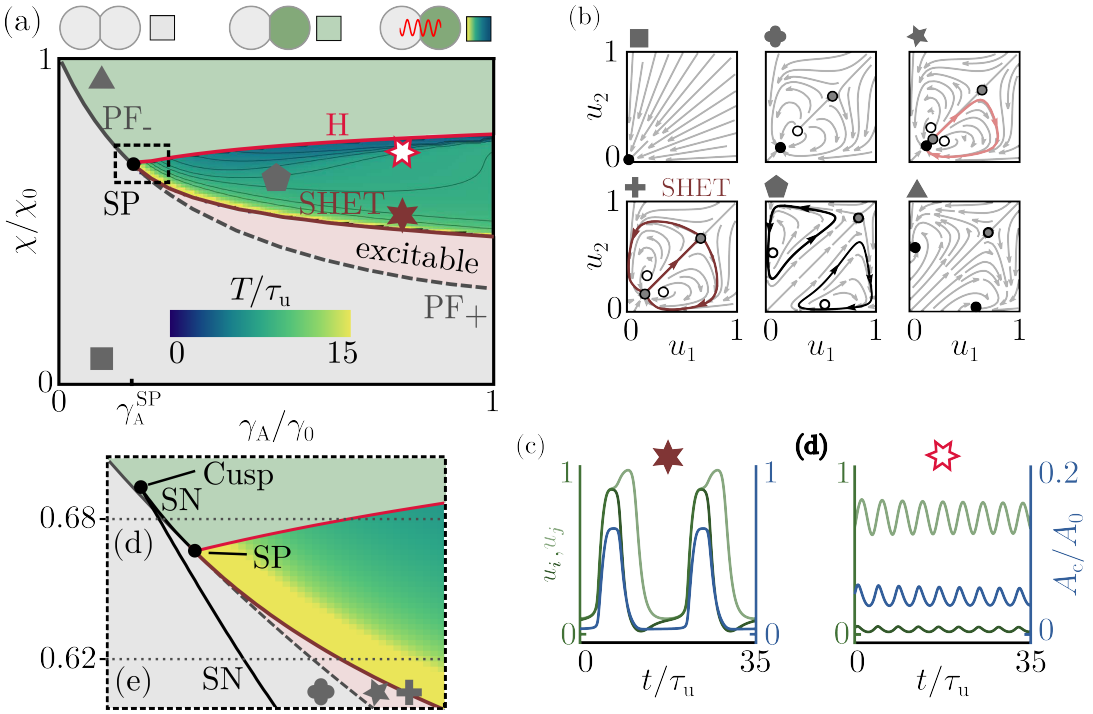

Figure 3.3. Excitability and oscillations of mechanochemically coupled cell pairs. (a) Adaptive adhesion leads to self-sustained oscillations of signals and cell shapes (color gradient and contour lines denote the oscillation period T). The oscillatory regime is surrounded by saddle-heteroclinic (SHET) and Hopf (H) bifurcation lines, which originate from a saddle-node pitchfork codimension-2 point (SP) (PF$_-$: supercritical pitchfork PF$_+$: subcritical pitchfork). Bottom panel: Enlarged view of the SP point environment shows saddle-node (SN) and cusp bifurcations that preserve stable attractor structures. The reference susceptibility is the critical value in the absence of adaptive tension ($\chi_0 = \chi_{PF}|_{\gamma_A=0}$). (b) Phase portraits for parameter values marked with gray symbols (filled black circles: stable steady states, filled gray circles: saddles, open circles: unstable steady states, rose line: trajectory in the excitable regime, red lines: heteroclinics, black lines: limit cycles). (c, d) Oscillation amplitudes decrease and the oscillation period increases with waveforms changing from relaxation-like (near the SHET line) to sinusoidal (near the Hopf line) for increasing χ. Parameter values given in Appendix J

The large contact effectively lowers the threshold susceptibility and drives the divergence of the internal states, which in turn reduces adhesion and the contact area. Correspondingly, starting from nearly uniform conditions, the time it takes for the internal states to diverge decreases with increasing γ_A and correlates with the largest eigenvalue of the saddle [Fig. 3.2(b)]. I find regimes of symmetry-breaking for $h \geq 2$, which increase with the baseline tension ratio $\gamma_0/2\gamma_f$ [Fig. 3.2(c)], as well as with increasing Hill coefficient h [Fig. 3.2(d)]. Overall, I find that shape-dependent mechanochemical feedback increases

the robustness of symmetry-breaking, which could aid reliable fate determination in noisy biological environments [17, 68, 146]. For instance, adaptive contact dynamics occur between sensory cell pairs in zebrafish embryos that exchange mutually inhibitory signals to undergo robust symmetry breaking [68, 87].

3.3 Tunable self-sustained oscillations in droplet pairs

At large values of the adaptive adhesion coefficient, the coupling between signaling and interface geometry can drive self-sustained oscillations of the internal states and shape of interacting cell pairs. These oscillations are driven by competition between the adaptive adhesion and the tendency of the pair to undergo symmetry-breaking: the product of internal states u_1u_2 increases the contact area according to Eq. (2.68), thereby driving their own inhibition, leading to negative feedback. The oscillatory regime, bounded by Hopf (H) and saddle heteroclinic (SHET) bifurcation lines, separates the stable symmetric and symmetry-broken states in the parameter diagram [Fig. 3.3(a-b)], derived via numerical continuation (Appendix G). These lines originate from a saddle-node pitchfork bifurcation point (SP)—a codimension-2 bifurcation at which the PF line tangentially intersects with a saddle-node (SN) bifurcation line [Fig. 3.3(a, c)] [156].

When $\gamma_A > \gamma_A^{SP}$ and χ reaches the critical susceptibility χ_{PF}, the inhibitory signals induce symmetry-breaking and the unstable fixed point undergoes a subcritical pitchfork bifurcation, producing a saddle and two new unstable fixed points [Fig. 3.3(b) star]. In this regime the droplet pair is excitable: fluctuations moving the internal states beyond the separatrices, which connect the saddle to the unstable fixed points, trigger a large increase of both internal states and the contact area A_c, followed by transient symmetry-breaking [Fig. 3.3(b) star]. Increasing χ shortens the distance between the uniform stable dfixed point and the saddle, thus lowering the excitation threshold until the two points collide at the SHET line and give rise to a pair of heteroclinic orbits that connect the resulting transversely stable, nonhyperbolic point to the second saddle point [Fig. 3.3(b) cross]. This nonhyperbolic point is destroyed as the heteroclinic orbits bifurcate into two symmetric stable limit cycles [Fig. 3.3(b) pentagon], which remain the only stable attractors of the system. Thus, cycles appear once transmitted signals are strong enough to induce symmetry-breaking, which in turn lowers the adhesion—and thereby the contact area—sufficiently to reduce signals below the symmetry-breaking threshold. In turn, the product of states [Eq. (2.86)] increases again, thereby driving adhesion, contact area, and signal amplitude back above the threshold. Depending on the two feedback parameters, the mechanochemical oscillations exhibit a range of temporal profiles. Near the SHET line the droplet pair exhibits relaxation-type oscillations in which it spends a large fraction of

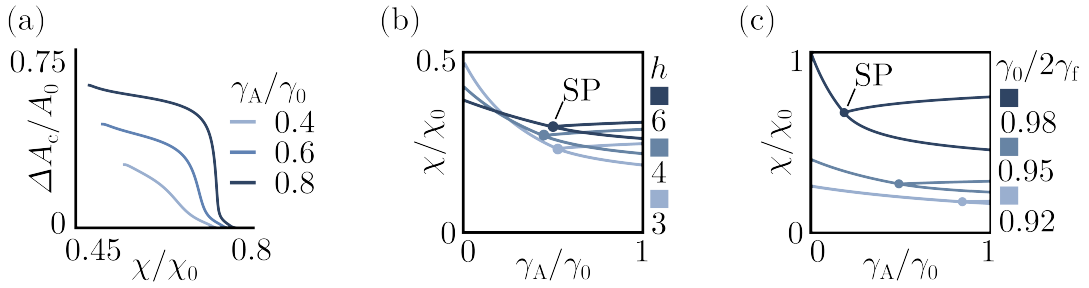

Figure 3.4. (a) Amplitude of contact area oscillations in droplet pairs. (b, c) The location of the SP point and associated bifurcations in the state diagram depends on (b) the Hill coefficient h of the response function and (c) the baseline tension ratio $\gamma_0/2\gamma_f$.

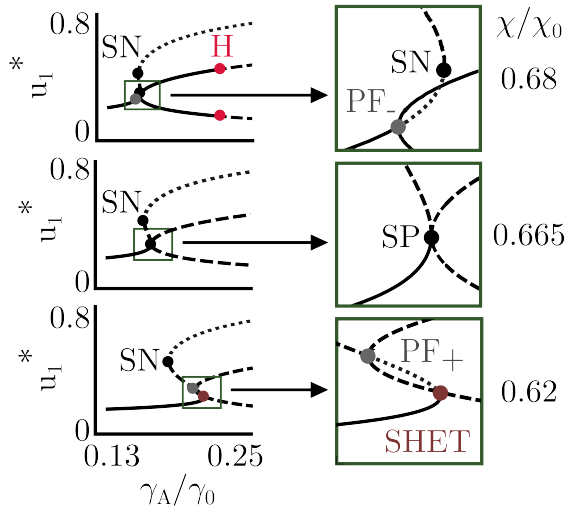

Figure 3.5. Series of bifurcation diagrams close to the codimension-2 SP bifurcation. Stable (solid line), unstable (dashed line) fixpoints and saddles (dotted line) computed for variation of γ_A/γ_0 as indicated by gray dotted lines in Fig. 3.3(a). Panels on the right show how the PF and SN interact, turning the latter into a SHET.

the cycle in small-area configurations with nearly identical states, interrupted by spikes in the contact area A_c and rapid, transient symmetry-breaking [Fig. 3.3(d)]. The oscillation period diverges as χ approaches χ_{SHET} due to the ghost of the destroyed saddle point that critically slows down the limit-cycle phase when passing through its vicinity [Fig. 3.3(a)]. With increasing χ, the time-averaged difference between the internal states increases and the oscillation amplitudes decrease, reaching near-sinusoidal waveforms in states and contact area close to the Hopf bifurcation line, where the limit cycles smoothly contract into symmetry-broken fixed points [Fig. 3.3(b, d-e)].

The position of the SP point within the feedback-parameter diagram, and the size of the associated regimes depend on the baseline tension ratio $\gamma_0/2\gamma_f$, and on the Hill coefficient h in the response function [Eq. (2.73)]. Increasing γ_0 lowers the threshold adaptive tension

for the onset of oscillations [Fig. 3.4(b)], while for low γ_0 the adaptive adhesion can push the interface into a regime where any area increase lowers the total surface energy, leading to shape instabilities [157, 158]. Close to $\gamma_A/\gamma_0 = 1$, such instabilities may remain transient, i.e. restricted to fractions of the oscillation phase, before restabilizing due to the decrease of adhesion upon symmetry-breaking of internal states, whereas at large γ_A/γ_0, these effects are expected to dominate the dynamics and lead to new phenomena. I found shape bistabilities and symmetry-breaking for Hill coefficients $h \geq 2$, and oscillations for $h \geq 3$. Strongly nonlinear response functions are commonly used to model regulatory feedbacks in cells [67, 107, 159], and experimental evidence has been reported for e.g. the Nodal pathways [108, 144]. Interestingly, I observe that strong adaptive adhesion achieves lower thresholds for smaller Hill coefficients, i.e. that the PF bifurcation lines for different Hill coefficients intersect in the feedback parameter space [Fig. 3.2(c), Fig. 3.4(a)], indicating a non-trivial interplay between the response nonlinearity and the geometry-dependent nonlinearity which together drive symmetry-breaking.
Together, these results illustrate how mechanochemical feedback can drive excitability and self-sustained oscillations.

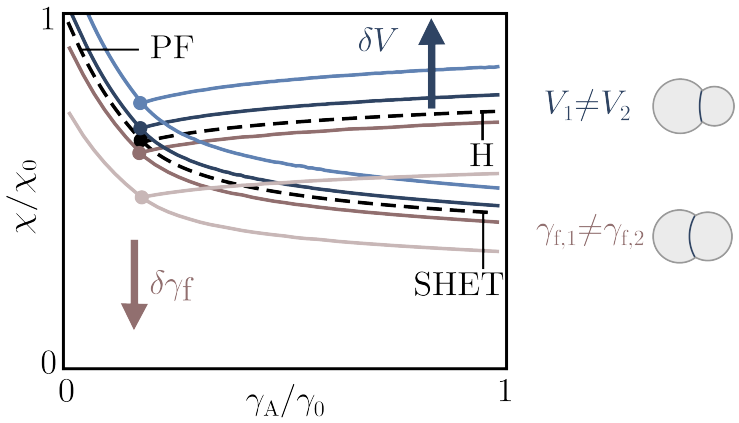

Figure 3.6. Different cell volumes $\delta V/\bar{V} = \{0.25, 0.5\}$ (blue) or outer tensions $\delta\gamma_f/\bar{\gamma}_f = \{0.25, 0.5\}$ (brown) shift the SP point and associated bifurcation lines in the state diagram. Parameter values given in Appendix J.

3.4 Feedback dynamics in asymmetric droplet pairs

The SP point arises for identical droplets. While such state-space structures have been found and experimentally characterized for instance in optical cavities [156], most physical systems exhibit non-negligible variations in their properties. Differences in the properties of the interacting droplets change the state diagram shown in Fig. 3.3(a). For unequal droplet volumes $V_{1,2} = \bar{V} \pm \delta V$, symmetry-breaking and oscillatory dynamics emerge at

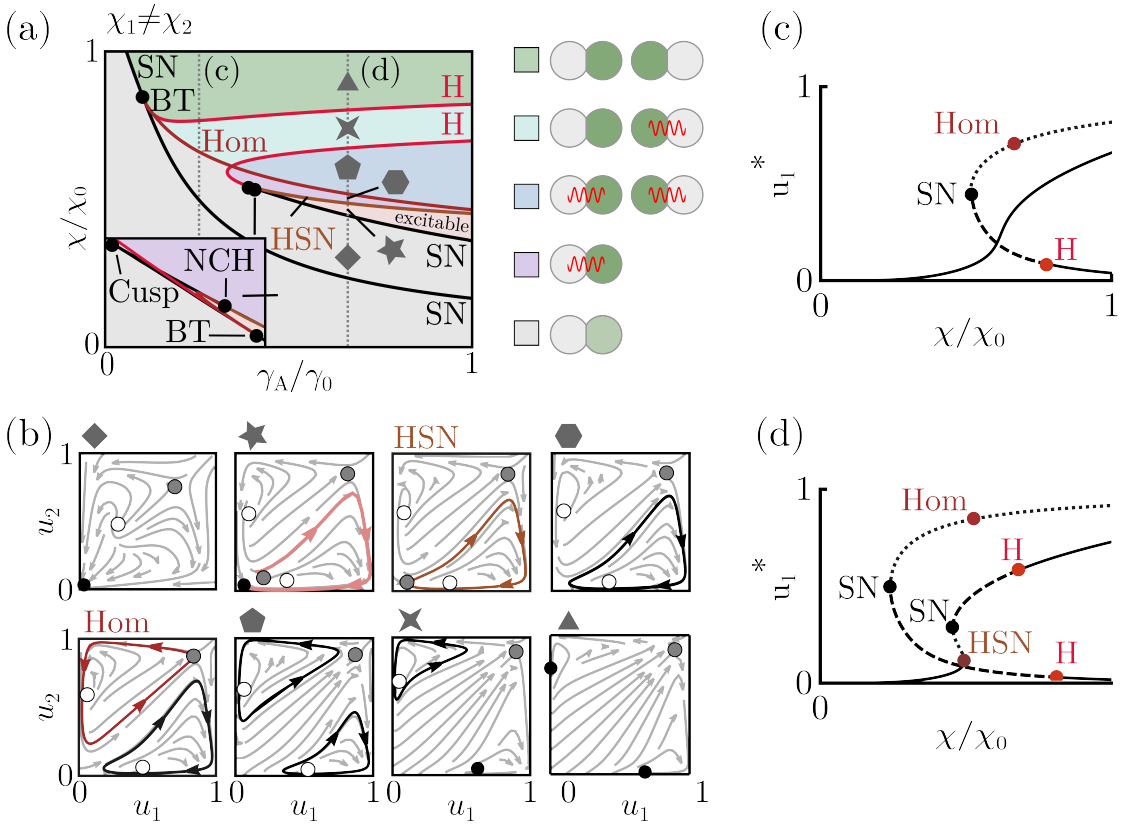

Figure 3.7. Heterogeneous susceptibility in interacting cell pairs. (a) A difference in signal susceptibilities $\delta\chi/\bar{\chi} = 0.05$ (i.e. $\chi_1/\chi_2 \approx 1.1$) splits the SP point into a pair of Bogdanov-Takens bifurcation points (BT), a non-central homoclinic to saddle-node bifurcation (NCH) and associated bifurcation lines. Inset shows the state diagram close to the second BT point ($\gamma_A/\gamma_0 \in [0.3896, 0.403]$, $\chi/\chi_0 \in [0.5388, 0.5441]$). Note that NCH and BT are connected by a homoclinic (Hom). (HSN: Saddle-node homoclinic). (b) Phase portraits for parameter values marked with gray symbols in (b). (filled black circle: stable steady state, filled gray circle: saddle, open circle: unstable steady state, rose line: trajectory in the excitable regime, thick black line: limit cycle) (c) Wit unequal signaling properties ($\chi_1 \neq \chi_2$), the pitchfork bifurcation is replaced by a new saddle-node bifurcation (compare to Fig. 3.3(c)). Parameter values given in Appendix J.

a larger signaling susceptibility χ than in pairs of identical droplets, whereas a difference in the outer surface tensions $\gamma_{f,1,2} = \bar{\gamma}_f \pm \delta\gamma_f$ promotes symmetry-breaking and oscillations at lower susceptibilities due to partial internalization resulting in larger equilibrium contact areas [Fig. 3.6]. For details about parameterizing asymmetric droplet shapes, about minimizing their surface energy and about computing the mutual contact area, see Appendix I.

Tension and volume asymmetry do not favour any droplet to reach a higher or lower internal state, because the signaling properties of each droplet remain unaffected, and thus

the topology of the state space is preserved. In contrast, numerical continuation shows that a difference in the signaling susceptibility $\chi_{1,2} = \bar{\chi} \pm \delta\chi$ splits the SP point into two Bogdanov-Takens (BT) codimension-2 points, and the SHET line into two homoclinics (Hom) and a saddle-node homoclinic (HSN) bifurcation line emerging from a non-central homoclinic to saddle-node (NCH) [Fig. 3.7(a)]. Accordingly, the limit cycle and the corresponding symmetry-broken state, in which the less susceptible droplet maintains the lower internal state, require lower values of χ and γ_A than the inverse symmetry-broken states. Thus, two limit cycles appear at different susceptibilities through a HSN and a Hom bifurcation [Fig. 3.7(b)], compared to homogeneous droplets, for which two limit cycles appear simultaneously in a SHET bifurcation [Fig. 3.3(b) cross]. This allows for parameter regimes with single limit cycles [Fig. 3.7(b) hexagon] or coexistence with stable fixed points [Fig. 3.7(b) 4-pointed star]—contrary to the case of identical susceptibilities. Heterogeneous material properties can thus produce an even wider spectrum of dynamics.

3.5 Shape oscillations and total wetting of adhesive droplets

In the previous sections, I discussed the shape and state dynamics in droplet pairs arising from contact-dependent mechanochemical feedback. Despite minimal degrees of freedom—one state variable per droplet—I found a rich dynamical landscape including multistability, excitability and self-sustained oscillations. Note that in this case, a pair of droplets has two free state variables, the minimal degree of freedom necessary to observe oscillations.

In the following, I return to the single droplet adhering to a functionalized stiff substrate. Given a single, dynamic state variable, the Cusp bifurcation and the associated bistable regime discussed in Section 3.1 already represent the range of bifurcation structures that can be expected in a one-dimensional system. To further extend the scope of the analysis, I consider in the following that the droplet has two internal states $u_\mathrm{R}, u_\mathrm{N}$, where u_R controls the signaling activity and u_N the active surface mechanics. The *one-state-per-droplet* case was motivated from microscopic equations, where a master regulator molecule (Section 2.3.1), e.g. a transcription factor, changes it's concentration in response to signals on the slowest system time scale. For a *two-state-model*, however, the introduction of a master regulator is not necessary. Instead, one can consider that u_R represents the normalized concentration of receptor molecules, while u_N is the normalized concentration of adhesion molecules. Considering a nonlinear production rate of receptor molecules (R) and adhesion molecules (N) depending on the received signal s [Eq. (2.69)] leads to the

system of equations [compare to Eq. (2.72)]

$$\tau_{\mathrm{N}}\frac{du_{\mathrm{N}}}{dt} = \sigma_{\mathrm{N}}(s) - u_{\mathrm{N}}, \tag{3.5}$$

$$\tau_{\mathrm{R}}\frac{du_{\mathrm{R}}}{dt} = \sigma_{\mathrm{R}}(s) - u_{\mathrm{R}}, \tag{3.6}$$

with a contact tension [compare to Eq. (2.66)]

$$\gamma_{\mathrm{c}} = \gamma_0 - \gamma_{\mathrm{A}} u_{\mathrm{N}} \tag{3.7}$$

and a received signal [compare to Eqs. (2.75),(2.82)]

$$s = \phi\chi\frac{A_{\mathrm{c}}}{A_0}(u_R + u_R^0), \tag{3.8}$$

in which u_{R}^0 is the normalized base line concentration of receptors independent of signaling, χ the susceptibility and ϕ the available amount of signal. Similar to Section 2.3.1, I thereby assume that the loss of receptors at the surface due to signaling can be neglected. Otherwise, an additional contact area-dependent decay term has to be introduced in Eq. (3.6). Note that if $u_{\mathrm{R}}^0 = 0$ and $\sigma(s = 0) = 0$, then $u_{\mathrm{R}} = 0$ is always a fixpoint of Eq. (3.6). Equation (3.8) introduces the coupled parameter $\chi\phi$ in order to emphasize that it can not only change due to changes in the intrinsic susceptibility χ of the signal receiving droplet, but also due to changes of the available, external signal ϕ. In previous sections, both contributions were summarized in the parameter χ [compare Eqs. (2.80), (2.82)].

The nonlinear response functions $\sigma_{\mathrm{N}}, \sigma_{\mathrm{R}}$ can be increasing or decreasing functions of the received signal, depending on the sign of the corresponding Hill coefficient $h_{\mathrm{N}}, h_{\mathrm{R}}$, which fundamentally defines the feedback dynamics [Fig. 3.8. When both $u_{\mathrm{R}}, u_{\mathrm{N}}$ decrease in response to the received signal ($h_{\mathrm{R}}, h_{\mathrm{N}} < 0$), the feedback in both states acts to reduce signals and prevent substrate wetting. In this case, the system has a single steady state for any combination of feedback parameter, with a contact area that decreases with increasing $\chi\phi$.

On the other hand, when both $u_{\mathrm{R}}, u_{\mathrm{N}}$ increase in response to received signals ($h_{\mathrm{R}}, h_{\mathrm{N}} > 0$), then the positive feedback can induce a bistability between two states of weak and strong wetting, as discussed in Section 3.1. The regime of bistability is demarcated by two SN lines converging in two codimension-2 cusp bifurcation points [Fig. 3.8(b)]. The Cusp at lower adaptive adhesion corresponds to the Cusp shown in Fig. 3.1.

Interestingly, for a sufficiently large adaptive adhesion coefficient, positive feedback in either of the two dynamic states can push the system into a total wetting state [Fig. 3.8(b)]. From Eq. (3.7) and $u_{\mathrm{N}} \leq 1$ follows that total wetting is accessible if $\gamma_{\mathrm{A}} \geq \gamma_0 + \gamma_{\mathrm{f}}$ [Fig. 3.8(b), vertical dashed line], and phase space dynamics are ill-defined if $\gamma_{\mathrm{A}} u_{\mathrm{N}} \geq$

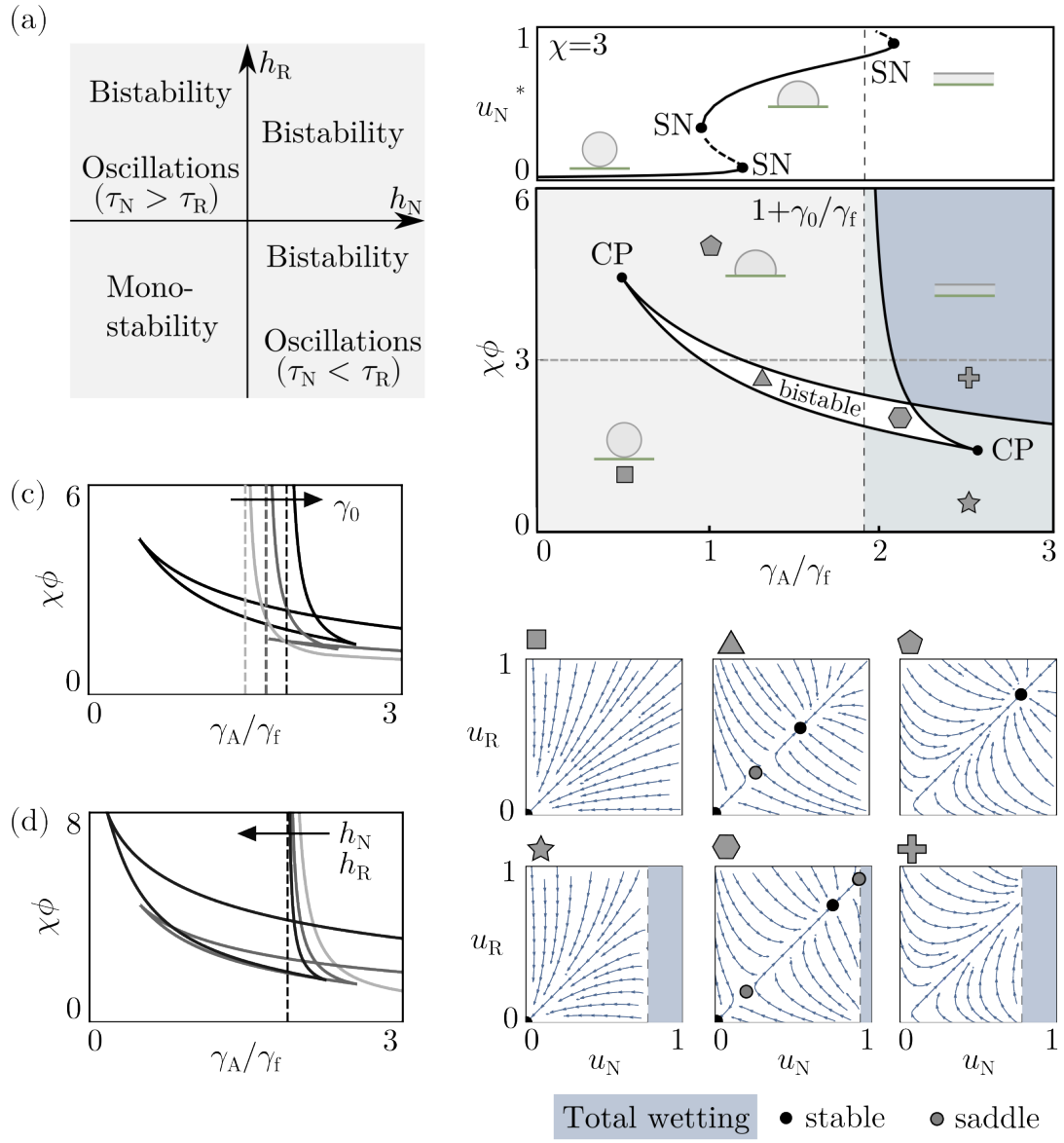

Figure 3.8. Multi-stability of shape-adaptive adherent droplets. (a) The nonlinear feedback dynamics that can possibly be observed depend on the Hill coefficients of the response functions h_R, h_N and the time scale ratio τ_N/τ_R. (b) State-space with respect to adaptive adhesion coefficient γ_A/γ_f and coupled parameter $\chi\phi$. The top diagram depicts the steady-state u_N for $\chi\phi = 3$. The vertical, dashed line indicates the minimal adaptive adhesion coefficient for which total wetting is possible. Black lines correspond to saddle node bifurcations (SN) converging in two Cusp points (CP). In the dark blue regime the system always diverges towards total wetting (i.e. $A_c \to \infty$). Below: phase portraits as marked by symbols. $h_N = h_R = 1, u_R^0 = 0.05, \gamma_0/\gamma_f = 0.9, \tau_N/\tau_R = 1$ (c, d) The size of the bistable regime decreases with decreasing γ_0/γ_f ((c) light to dark: $\gamma_0\gamma_f = \{0.5, 0.7, 0.9\}$ or decreasing Hill coefficients ((d) light to dark: $h_N = h_R = \{0.8, 1, 1.2\}$).

$\gamma_0 + \gamma_f$, which is depicted by the blue shaded regions in the phase portraits of Fig. 3.8(b). For sufficiently large $\chi\phi$ and adaptive tension γ_A, the system is always driven towards total wetting, independent of the initial conditions [Fig. 3.8(b), dark blue region]. This regime is separated by a line of saddle-node bifurcations (SN) from the parameter regimes with one or two stable solutions with partial wetting. Note that for physical droplets or cells, total wetting would probably imply that the behavior is governed by physical forces not captured in this simple framework, e.g. where spreading is opposed by elastic forces of the nucleus resisting deformation, or by an active response of the cytoskeleton.
As discussed in Section 3.1, decreasing the Hill coefficients or increasing the base line tension γ_0 reduces the size of the bistable regime until it disappears in a single line of saddle node bifurcations separating partial and total wetting regimes [Fig. 3.8(d)].
In the limit of an infinite sharp, positive feedback response, i.e. $h_R, h_N \to \infty$, conditions for bistability can be derived analytically, as I have shown in Section 3.1 [Eq. (3.3), (3.4)]. It is straightforward to derive the corresponding expressions for the two-state system

$$\chi\phi_1 = \frac{A_0}{(1+u_R^0)\, A_c|_{\gamma_0-\gamma_A}} \tag{3.9}$$

and

$$\chi\phi_2 = \frac{A_0}{(1+u_R^0)\, A_c|_{\gamma_0}}. \tag{3.10}$$

State and shape oscillations in adherent droplets

When the Hill coefficients h_N and h_R are of different sign, then the system combines a positive and a negative feedback loop. Generically, when a fast positive feedback loop is coupled to a delayed negative feedback, oscillations are possible. In the following, I explore this case at the example of $h_N > 0$ and $h_R < 0$, i.e. where strong signals promote wetting and produce a bistability between different states of partial wetting as previously discussed [Fig. 3.1], but signals decrease the production of receptor molecules. For $\tau_n/\tau_R < 1$, the mechanical, positive feedback is faster than the negative feedback of receptor molecule regulation. As the time scale ratio is reduced, steady states in the partial wetting regime with large contact area are destabilized, because the fast mechanical adaptation allows the system to quickly relax back to the small contact area configuration before an opposing, strong signal can be established that maintains a sufficiently high adhesion molecule concentration. Therefore, part of the bistable regime is lost for excitable dynamics: fluctuations around the unique stable state of the system (weak wetting) can excite a transient trajectory with strong wetting and large contact interface [Fig. 3.9(c) star]. When $\gamma_A \leq \gamma_0 + \gamma_f$, such excitations can drive the system towards total wetting [Fig. 3.9(c) square].

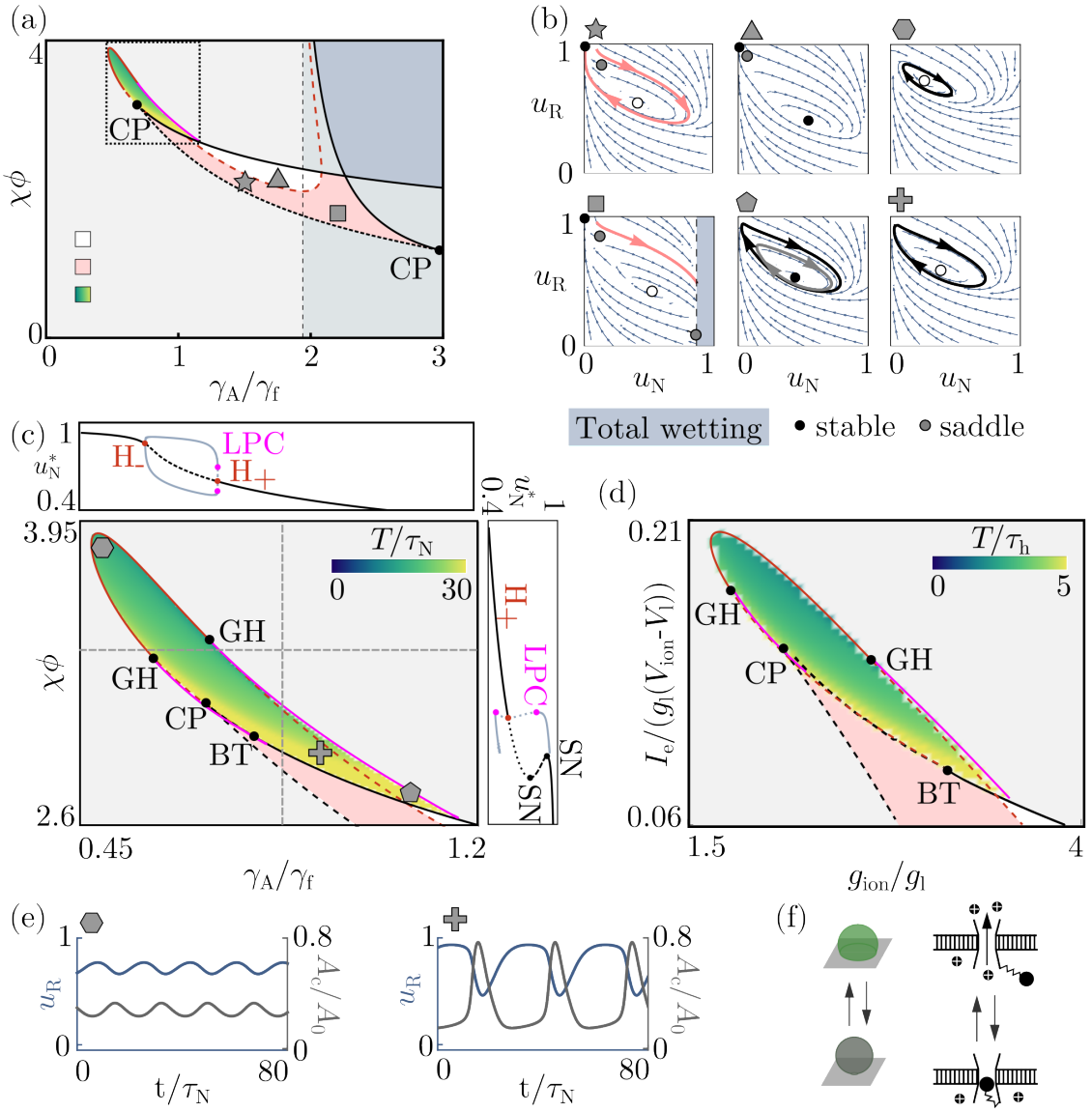

Figure 3.9. Oscillations in adherent droplets. (a) Adaptive tension feedback creates regimes of excitability and self-sustained oscillations of droplet shapes and internal states. $h_N = 4, h_R = -4, u_R^0 = 0.05, \gamma_0/\gamma_f = 0.9, \tau_N/\tau_R = 0.25$. (b) Phase portraits for symbols indicated in panel (a). (c) Zoomed-in state diagram as indicated in (a), GH: Generalized Hopf, CP: Cusp, BT: Bogdanov-Takens, black, solid line: Saddle-node to a stable node; black, dashed line: Saddle-node to an unstable node; red, solid line: supercritical Hopf; red, dashed line: subcritical Hopf; solid, magenta line: Limit point of cycles (LPC). Top and right diagrams depict steady state u_N for $\chi\phi = 3.375$ and $\gamma_A/\gamma_f = 0.85$ (gray dashed lines). Light blue lines: Min/Max u_N of limit cycles. (d) Conductance-based neuronal excitation models, here for the $I_{Na,t}$-model [160] in the limit of an instantaneously adjusting membrane potential, show topologically equivalent bifurcation structures. (e) Oscillation waveforms range from near-sinusoidal to relaxation-type. (f) Shape dynamics in adherent droplets correspond to gate dynamics in ion channels.

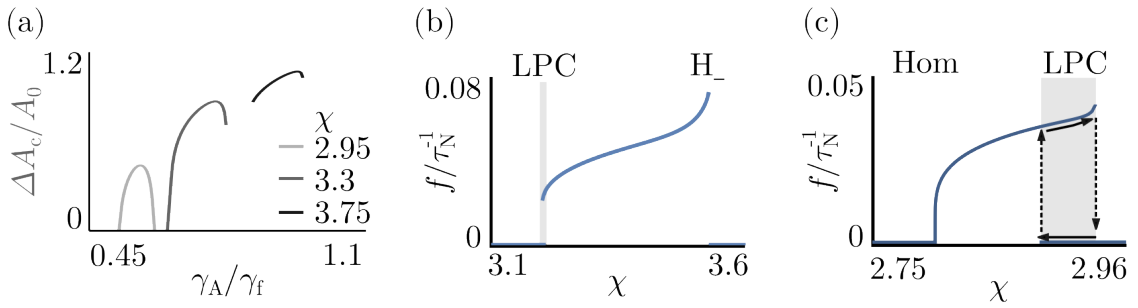

Figure 3.10. (a) The difference between maximal and minimal contact area during limit cycle oscillations. (b, c) Frequencies of self-sustained oscillations for $\gamma_A/\gamma_f = \{0.65, 0.95\}$, respectively. Close to the homoclinic (Hom), frequencies can be arbitrary small. Close to the limit point of cycles (LPC) stable quiescent and oscillatory states coexist (marked light gray). The subcritical bifurcation structure can lead to hysteresis (indicated by arrows).

When the time scale ratio is sufficiently reduced, a codimension-2 Bogdanov-Takens bifurcation point (BT) moves from the lower to the upper SN branch, thereby passing through the left CP bifurcation point. In the three-dimensional parameter space $\chi\phi, \gamma_A, \tau_N/\tau_R$, this transition marks a codimension-3 Bogdanov-Takens-Cusp (BTC) bifurcation point. It coincides with the emergence of a regime of self-sustained shape and signaling oscillations [Fig. 3.9(a-c)]. As for the droplet pair [Fig. 3.3], the oscillation waveform depends on the two feedback parameters $\chi\phi$ and γ_A: for small γ_A and large $\chi\phi$—close to a supercritical Hopf bifurcation line—oscillations are near-sinusoidal with small oscillation amplitudes. Increasing γ_A while decreasing $\chi\phi$ increases the amplitude of shape changes and renders the oscillations more and more relaxation-like [Fig. 3.9(e)]. At the transition between the oscillatory and excitable regimes, the oscillation period diverges due to the presence of a homoclinic bifurcation associated with the BT point. The maximum shape oscillation amplitude (i.e. $(A_c^{max} - A_c^{min})/A_0$ during an oscillation cycle for given γ_A/γ_f) reveals a near linear scaling with the adaptive tension coefficient γ_A/γ_f [Fig. 3.10(a)].

In general, the amplitude, frequency and waveform of the oscillations can be understood from the closest codimension-1 bifurcation delineating the oscillatory regime–especially close to the transition between quiescent and oscillatory states [Fig. 3.10(b,c)]. These bifurcations are organized by several higher order, codimension-2 bifurcation points including the Cusp, the BT point and two generalized Hopf (GH) bifurcation points [Fig. 3.9(c)], which in turn descent from the codimension-3 BTC bifurcation [161]. At the GH bifurcation points, the line of supercritical Hopf bifurcations splits into a subcritical Hopf and a saddle-node of limit cycles bifurcation [Fig. 3.9(c)]. Each GH point opens a parameter regime at the transition between oscillatory and non-oscillatory states, in which the

stable limit cycle coexist with a stable fixpoint solution [Fig. 3.9(c) and Fig. 3.10(b-c)]. Here, the droplet can experience hysteresis: for instance, given a fixed adaptive adhesion coefficient, the external signal at which the system transitions from a steady state to a limit cycle, and vice versa, are not identical [Fig. 3.10(c)]. Moreover, oscillation period and amplitude at the transition are non-zero and finite.

In summary, transitions between the oscillatory and non-oscillatory regime can be grouped in three classes: (i) at the supercritical Hopf bifurcation line (small γ_A), the period is finite and the oscillation amplitude close to zero, (ii) at the LPCs, amplitude and frequency are finite and non-zero at the onset of oscillations, and (iii) at the homoclinic [Fig. 3.10(c)], amplitudes are large and the oscillation period diverges. It showcases how tuning the adaptive adhesion coefficient, a mechanical coupling parameter, allows to tune the onset of oscillations in response to an external signal ϕ in signal-processing droplets.

Shape-adaptation oscillations generate neuron-like dynamics

The bifurcation structures discussed above—in particular the BTC codimension-3 bifurcation—are commonly encountered in neuroscience. More specifically, they are a hallmark of conductance-based (Hodgkin-Huxley type) models describing the generation of action potentials in firing neurons [160, 161, 162, 163]. The generation of action potentials is a core process in neurons to produce and process signals. It raises the intriguing question, how the variables and parameters in the conductance-based models map to internal states and shape dynamics of signal processing adherent droplets [Fig. 3.9(f)].

In neurons, ion channels open stochastically with a time-dependent probability $p(t) = m(t)h(t)$ depending on the state of so-called *activation* and *inactivation gates* $m(t)$ and $h(t)$. These variables represent the probability of ion channel subdomains to take a configuration that allows ions to pass. All activation/inactivation variables must be in an open state for ions to flow. Depending on the type of ion channel, activation and inactivation gates can be coupled in various ways and proportions [160]. For instance, consider the transient sodium channel model $I_{\mathrm{Na,t}}$ [160] in which the membrane potential V changes over time as

$$C\frac{dV}{dt} = -I_{\mathrm{e}} - g_{\mathrm{ion}}m(t)h(t)(V - V_{\mathrm{ion}}) - g_{\mathrm{l}}(V - V_{\mathrm{l}}) \tag{3.11}$$

with C the membrane capacitance, I_{e} an externally applied current (the signal that the neuron responds to), g_{ion} the conductance if all sodium ion channels are open, V_{ion} the sodium Nernst potential, g_{l} the leak conductance at the membrane and V_{l} the leak membrane potential. Following Fermi-Dirac statistics for a 2-state system (gates are

either in an *open* or *closed* state), gate dynamics are commonly modeled as

$$\tau_{\mathrm{m}} m(t) = m_\infty - m(t), \tag{3.12}$$

$$\tau_{\mathrm{h}} h(t) = h_\infty - h(t) \tag{3.13}$$

with

$$m_\infty = \frac{1}{1+\exp\left(V_1 - V\right)/V_2}, \tag{3.14}$$

$$h_\infty = \frac{1}{1+\exp\left(V_3 - V\right)/V_4} \tag{3.15}$$

reflecting the steady-state probability for a gate to be open given a fixed membrane voltage V [160]. Its form can be derived from the free energy difference between open and closed ion channel states [164]; $V_i,\ i \in \{1,2,3,4\}$ are usually treated as fit parameters. Consider that $m(t)$ is an activation variable that increases with the membrane voltage, and $h(t)$ an inactivation gate that decreases with rising voltage levels. Comparison of Eqs. (3.5),(3.6) and Eqs. (3.12) ,(3.13) indicates that $m(t)$ corresponds to the change of adhesion molecules u_{N} (fast positive feedback), while $h(t)$ maps to the normalized receptor concentration u_{R} (delayed negative feedback). Moreover, changes in the membrane potential V correspond to changing signals s received by the adherent droplet. As discussed in Chapter 2, the framework for shape-adapting droplets focuses on a time scale regime governed by the production and decay rates of molecules, while shape and signal adapt instantaneously. In the conductance-based neuron model, this corresponds to a membrane potential that equilibrates much faster than changes in the gate dynamics. In contrast, most studies of neuronal dynamics assume that the activation gate acts faster than changes of the membrane potential V [160, 164]. However, because similar bifurcation structures can be observed for both cases—in particular the Bogdanov-Takens-Cusp bifurcation [161]—I assume in the following fast voltage dynamics ($dV/dt = 0$). The voltage is then given as a function of the two dynamic gate variables $V(m(t), h(t))$ [Eq. (3.11)]. When I define the normalized voltage $v = (V - V_{\mathrm{l}})/(V_{\mathrm{ion}} - V_{\mathrm{l}})$, it follows from Eq. (3.11) that

$$v = \frac{\dfrac{I_{\mathrm{e}}}{g_{\mathrm{l}}(V_{\mathrm{ion}} - V_{\mathrm{l}})} + \dfrac{g_{\mathrm{ion}}}{g_{\mathrm{l}}} m(t)h(t)}{1 + \dfrac{g_{\mathrm{ion}}}{g_{\mathrm{l}}} m(t)h(t)}, \tag{3.16}$$

which only depends on two dimensionless parameters. Figure 3.9(d) shows part of the two-dimensional parameter space spanned by the conductance ratio g_{ion}/g_l—which tunes how strongly the membrane voltage responds to the opening and closing of the ion channels—and the normalized, externally applied current $I_{\mathrm{e}}/g_{\mathrm{l}}(V_{\mathrm{ion}} - V_{\mathrm{l}})$. The comparison between neurons and the shape-adapting droplet model shows a striking resemblance of bifurca-

tion topologies, and indeed, one finds the BTC and all descended lower codimensional bifurcations, including the BT, CP and GH bifurcation points [Fig. 3.3(c-d)] [163].
In the quiescent state, neurons occupy the non-oscillatory (gray) or excitable (pink) regime below the oscillatory regime [Fig. 3.9(d)]. When an external stimulus (in form of current I_e) is applied, the neuron transitions into the oscillatory regime, where it starts firing—creating a series of action potentials—until the external stimulus is withdrawn. Neurons can tune the oscillation waveform, and in particular the frequency of action potentials, via modification of the ion channel conductance g_{ion}, for instance via biochemical ion channel modifications [161, 162]. Analogously, signal processing adherent droplets can follow excitable and oscillatory dynamics in response to an external signal ϕ, which are tunable by the mechanical coupling parameter γ_A [Fig. 3.9(c)].

In light of the intriguing parallel between tunable oscillations in neurons and shape-adapting droplets, the question remains whether the corresponding parameter regimes are indeed accessible to physical droplets and cells. Moreover, it raises the question how the mechanochemical feedback dynamics in droplets influences signal processing. In the next section, I analyze the signal processing capacity of oscillating droplets, i.e. the ability to encode information via oscillations, in the limit case of an infinitely sharp signal response ($h_R, h_N \to \pm\infty$). Note that due to the slow, chemical time scales assumed for the signal-processing droplets (Chapter 2), only a few oscillation cycles would be expected to occur within minutes to hours. Neurons, on the other hand, can generate a series of action potentials on a sub-second time scale [160], allowing for a much faster and cleaner encoding of information in the frequency domain.
In Section 3.7, I apply the presented framework of signal processing droplets to infer the feedback parameters $\chi\phi$ and γ_A from contact angle measurements in zebrafish embryos. Although no oscillations are observed, I show in particular that the embryonic tissue occupies a feedback parameter regime closely associated with the CP bifurcation point that interacts with the BT point during the BTC codimension-3 bifurcation. In the embryo, proximity to the CP point enables the prediction of an experimentally observed tissue boundary formation.

3.6 How feedback dynamics encode information

Through evolution, biological systems have learned to position themselves close to critical points markingtransition between regimes of qualitatively different behavior [165, 166]. Thereby, a system becomes sensitive to small parameter changes. For instance, quiescent neurons are typically found in states close to the transition into the oscillatory regime such

that small external perturbations can set the system into an oscillatory state [160, 166]. The computational properties of firing neurons depend on their firing characteristics at the onset of self-sustained oscillations, e.g. the firing frequency [160]. For instance, neurons of excitability class I can fire with arbitrary slow frequency, while class II neurons always generate action potentials with a finite oscillation period.

In analogy to firing neurons, I consider the oscillation properties of shape-adapting droplets close to the transition between excitable and oscillatory regime. In particular, I ask if features of the oscillation allow to encode information about system state parameters in the presence of noise, focusing on encoding information in the frequency domain.

To simplify the analysis, I consider the limit in which the concentration of adhesion molecules u_N adjusts instantaneously to changes in the receptor molecule concentration, i.e. $\tau_\mathrm{N}/\tau_\mathrm{R} \to 0$. The concentration of adhesion molecules is then given by $u_\mathrm{N} = \sigma_\mathrm{N}(s)$ with $\sigma_\mathrm{N}(s) \in \{0, 1\}$ and the only dynamic equation to consider is

$$\dot{u_\mathrm{R}} = \begin{cases} 1 - u_\mathrm{R}, \text{ if } s < 1 \\ -u_\mathrm{R}, \text{ if } s \geq 1. \end{cases} \tag{3.17}$$

Sketches of corresponding phase portraits in the excitable and oscillatory regime are shown in Fig. 3.11(b) for the excitable regime ($\chi\phi \leq \chi\phi_\mathrm{crit}$) and the oscillatory regime ($\chi\phi > \chi\phi_\mathrm{crit}$). When the system is in the oscillatory state, one can compute the period of oscillations via integration of the two parts of the trajectory $T = T_1 + T_2$ with

$$T_1 = \int_{u_2}^{u_1} \frac{du_\mathrm{R}}{1 - u_\mathrm{R}} = \ln\left(\frac{1 - u_2}{1 - u_1}\right) \tag{3.18}$$

$$T_2 = \int_{u_1}^{u_2} \frac{du_\mathrm{R}}{-u_\mathrm{R}} = \ln\left(\frac{u_1}{u_2}\right), \tag{3.19}$$

where T_1, T_2, u_1, u_2 are defined as shown in Fig. 3.11(b), and the overall period is given by

$$T = \ln\left(\frac{u_2(1 - u_1)}{u_1(1 - u_2)}\right). \tag{3.20}$$

As long as the system moves along one branch in the phase portrait, u_N is constant. In particular, during T_2, $u_\mathrm{N} = 1$ and thus $A_\mathrm{c} = A_\mathrm{c}((\gamma_0 - \gamma_\mathrm{A})/\gamma_\mathrm{f})$, i.e. the droplet takes a shape with large contact area (strong wetting), while during T_1, $u_\mathrm{N} = 0$ and the contact area $A_\mathrm{c} = A_\mathrm{c}(\gamma_0/\gamma_\mathrm{f})$ is minimal. The transition between the two branches occurs whenever the signal passes the threshold $s = 1$. From Eq. (2.75) follows for the corresponding receptor concentrations u_1, u_2

$$u_1 = \frac{A_0}{\chi\phi A_\mathrm{c}((\gamma_0 - \gamma_\mathrm{A})/\gamma_\mathrm{f})} - u_R^0 \tag{3.21}$$

$$u_2 = \frac{A_0}{\chi\phi A_\mathrm{c}(\gamma_0/\gamma_\mathrm{f})} - u_R^0. \tag{3.22}$$

The transition between oscillatory and excitable regime is an SN-like (or SNIC-like) critical point, where the stable fixpoint ($u_\mathrm{N} = 0, u_\mathrm{R} = 1$) with small contact area $A_\mathrm{c}(\gamma_0/\gamma_\mathrm{f})$ is replaced by a limit cycle as the only stable attractor [Fig. 3.11(b)]. The condition for the transition

$$s = \chi\phi\frac{A_\mathrm{c}(\gamma_0)}{A_0}(1 + u_R^0) = 1 \tag{3.23}$$

matches the condition where the period T diverges [Eq. (3.20)]. Moreover, it fits the condition for one of the saddle node bifurcation points [Eq. (3.10)], thus, the period diverges due to the ghost of the saddle-node—a result I also found for the general case of finite Hill coefficients and non-zero time scale ratios using numerical continuation [Fig. 3.9(a)].

The ability of a system to oscillate with arbitrary slow frequency provides the capability to encode information about state parameters in the frequency domain. Indeed, many cellular processes respond not only to absolute concentration levels, but to temporal signatures of bulk concentration changes [167, 168, 169]. However, close to the onset of self-sustained oscillations, small perturbations can suffice to trigger an excitation. To assess the ability to robustly encode information through temporal dynamics, oscillations must therefore be studied under the presence of noise.

To gain a simple understanding of how features of shape- and state oscillations could encode information in the presence of perturbations, I consider that the signal s is affected by stochastic perturbations δs whenever the droplet is in the small contact area configuration ($u_\mathrm{N} = 0$). In particular, I consider a Cox process with fluctuations following Poisson distribution in time, and amplitudes drawn from a normal distribution with mean $\mu = 0$ and variance σ^2_noise. Perturbations are assumed to decay fast, such that they are non-additive. In the small contact area configuration ($u_\mathrm{N} = 0$), noise can trigger an excitation, i.e. a transient increase in the contact area, when the signal passes the threshold $s \geq 1$. It follows that fluctuations trigger an excitation if

$$\delta s \geq 1 - s(t) = 1 - \chi\phi\frac{A_\mathrm{c}|_{\gamma_0/\gamma_\mathrm{f}}}{A_0}(u_\mathrm{R}(t) + u_\mathrm{R}^0). \tag{3.24}$$

As $u_\mathrm{R}(t)$ changes over time, so does the probability that a fluctuation is sufficient to trigger an excitation. During T_1, u_R decreases and thus the probability of excitation increases. Note that I ignore fluctuations during T_2 that could shift the system back towards the small contact area configuration. The mean frequency of perturbation-induced oscillations then depends on the first passage time of the signal to pass the threshold. When fluctuations occur with rate λ, then the effective rate of fluctuations that suffice to pass the excitation threshold is

$$\lambda_\mathrm{eff}(t) = \lambda\left(1 - \Phi\left(\frac{1 - s(t)}{\sigma_\mathrm{noise}}\right)\right) \tag{3.25}$$

with Φ the cumulative density function of the normal distribution. It means that excitation-triggering fluctuations follow a thinned, non-homogeneous Poisson process. In the excitable regime, oscillations are solely noise-induced and their frequency is given by the mean of the inverse period

$$f = \int_0^\infty \frac{1}{T(t)} \lambda_{\text{eff}}(t) e^{\int_0^t \lambda_{\text{eff}}(\eta) d\eta} dt, \tag{3.26}$$

where $\lambda_{\text{eff}}(t) e^{\int_0^t \lambda_{\text{eff}}(\eta) d\eta} dt$ is the probability to observe the first fluctuation moving the system from phase T_1 to phase T_2 in the time interval $[t, t + dt]$ and

$$T(t) = t + \frac{\ln\left(\frac{1-(1-u_2)e^{-t}}{u_2}\right)}{A_{\text{c}}|_{\gamma_0 - \gamma_{\text{A}}}} \tag{3.27}$$

is the time of one oscillation cycle until the system returns to $u_{\text{R}} = u_1$ given that the excitation was triggered at time t. In the regime of self-sustained oscillations, when the system reaches $u_{\text{R}} = u_2$ (denoted as time $t_{\max}$, Eq. (3.18)) before any fluctuation has triggered an excitation, the system jumps to the large contact area state ($u_{\text{N}} = 1$). Taking this into account, the mean oscillation frequency is

$$f = \int_0^{t_{\max}} \frac{1}{T(t)} \lambda_{\text{eff}}(t) e^{\int_0^t \lambda_{\text{eff}}(\eta) d\eta} dt + \frac{1}{T(t_{\max})} e^{\int_0^{t_{\max}} \lambda_{\text{eff}}(\eta) d\eta}. \tag{3.28}$$

This gives a general expression for the mean oscillation frequency, in the excitable as well as in the oscillatory regime, considering that in the excitable regime $t_{\max} \to \infty$ such that the second term vanishes. The oscillation frequency was computed numerically and plotted in Fig. 3.11(c) for a varying variance of the perturbation amplitude σ^2_{noise}.

The sensitivity $d \ln f / d \ln \chi\phi$ describes the fractional change in frequency f given a fractional change in $\chi\phi$ [Fig. 3.11(d)]. In general, it decreases with increase of $\chi\phi$ and also decreases with the noise amplitude variance σ^2_{noise} in the excitable regime, but plateaus to a finite oscillation frequency determined by the frequency of self-sustained oscillations in the absence of noise [Eq. (3.20)].

To robustly encode signals, a system needs to maximize its signal-to-noise ratio. I thus compute the standard-deviation of the oscillation frequency relative to its mean value [Fig. 3.11(e)]. Interestingly, in the excitable regime, this ratio decreases with increasing perturbation amplitudes. In the oscillatory regime, where the frequency is mainly determined by the limit cycle of self-sustained oscillations, variations in the frequency instead increase with σ^2_{noise}. In conclusion, under the presence of stochastic perturbations, the ideal state for a system aiming for high sensitivity of the oscillation frequency with respect to a changing signal susceptibility $\chi\phi$ while guaranteeing a high signal-to-noise ratio is close to the bifurcation marking the transition between excitable and oscillatory regime–as commonly observed in other excitable systems encoding information in the frequency domain [166].

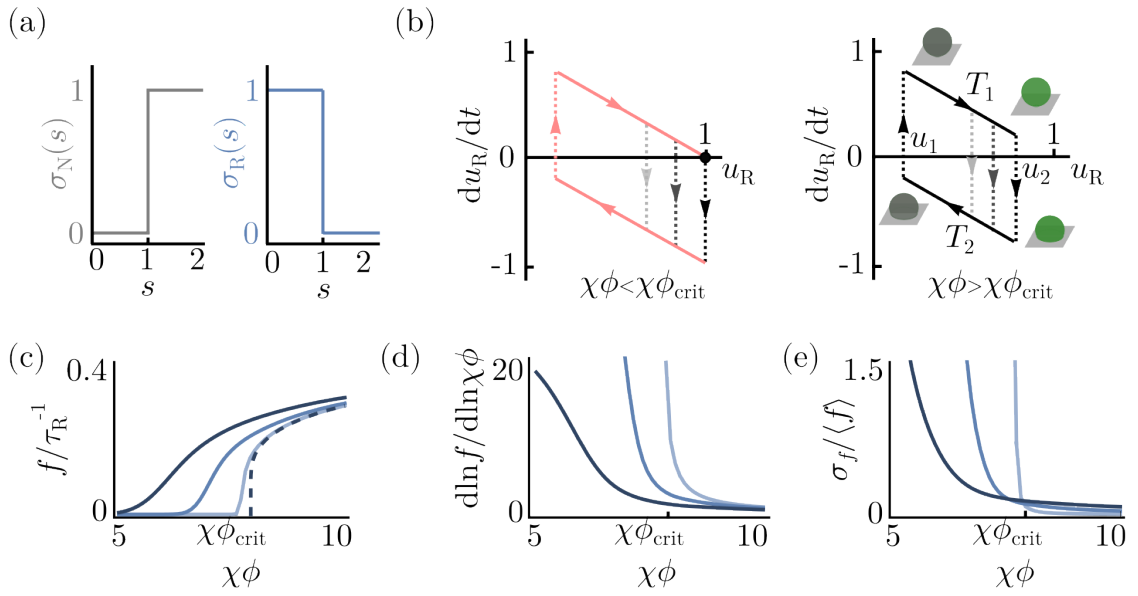

Figure 3.11. Dynamically encoding signals in the presence of noise. (a) Signaling response functions in the limit $h_N \to \infty, h_R \to -\infty$. (b) In the time scale limit $\tau_N/\tau_R \to 0$, $u_N \in \{0, 1\}$ adapts instantaneously. All dynamics are captured in the u_R phase diagram. In the excitable regime ($\chi\phi < \chi\phi_{crit}$), $u_R = 1$ is a stable state, but small perturbations can trigger an excitation (rose trajectory), thus , generating noise-induced oscillations. In the oscillatory regime ($\chi\phi > \chi\phi_{crit}$), the system follows a limit cycle with $u_R \in [u_1, u_2]$ and with two phases of period T_1 and T_2 corresponding to small ($A_c(\gamma_0)$) and large ($A_c(\gamma_0-\gamma_A)$ contact areas. During T_1, stochastic perturbations can trigger a contact area expansion before u_R has reached u_2. (c) Frequency of oscillations f in the presence of perturbations modeled as a Cox process with Poissonian distributed fluctuations of rate $\lambda = 10$ and gaussian amplitude with zero mean and standard deviation $\sigma = \{0.01, 0.05, 0.1\}$ (light to dark blue). (d) The sensitivity $d\ln f/d\ln\chi\phi$–i.e. the fractional frequency change df/f relative to fractional changes of $d(\chi\phi)/\chi\phi$–decreases with increasing $\chi\phi$ and increasing amplitudes of fluctuation σ (e). The standard deviation of the frequency σ_f relative to the mean frequency $\langle f\rangle$ decreases with increasing $\chi\phi$. Larger perturbations reduce the ratio in the excitable regime, but slightly increases it in the oscillatory regime ($\chi\phi > \chi\phi_{crit}$).

3.7 Emerging tissue boundaries in zebrafish mesendoderm formation

In this section, by applying the framework of signal processing droplets to shape measurements from zebrafish embryos, I show how feedback between cell-cell adhesion and signaling can support the formation of distinct tissue regions, highlighting the regulatory role of mechanochemical interactions in developmental patterning. In particular, I find that the experimental observations are best described by a combination of feedback parameters $\phi\chi, \gamma_{\mathrm{A}}$ close to the Cusp bifurcation point presented in Section 3.1. It suggests that physical systems can indeed explore parts of the parameter regime that are associated with the rich dynamical behavior outlined in previous sections.
This chapter starts with an overview of the main results obtained from the parameter inference. Subsequent sections explain the underlying analysis in more detail. All experimental data presented in this chapter was acquired by Camilla Autorino (Petridou lab, EMBL).

3.7.1 Mesendoderm formation in zebrafish embryos

Mesendoderm formation in zebrafish embryos is an early developmental event in which the cells that later form the organism's internal organs differentiate and alter their material properties. This process is guided by a spatial gradient of Nodal signaling activity, which decreases along the animal-to-vegetal embryo axis (AV-axis) from the margin towards the animal pole [Fig. 3.12(b)] [170], and involves changes in cell-cell adhesion [165]. Through positive feedback signals exchanged between cells increase their mutual adhesiveness. In contrast to Eq. (2.82), (where I considered mutually inhibitory signals), the signal received by a cell i is thus here defined as

$$s_i = \chi\phi\frac{A_{\mathrm{c}}}{A_0}. \tag{3.29}$$

with $\chi\phi$ the product of signal susceptibility and available signal, and A_{c} the total contact area per droplet.

3.7.2 Tension adaptation produces a shape transition

For constant external signals ϕ, numerical continuation of Eqs. (1.7), (2.72), (2.68), (3.29) with varying coupling parameters γ_{A} and χ reveals that the bistability between weakly and strongly adhesive states, and the associated bifurcation points already discussed in earlier sections (Section 3.1), can be found more generally for droplet lattices, where each droplet has the same number of contacts n [Fig. 3.12(a)].

I expect this shape transition to occur in diverse systems in which area-dependent signals affect mechanical changes. As an example of a specific mechanochemically regulated system, I thus investigated the cell shapes in the zebrafish blastoderm. In this embryonic tissue, it was previously shown that Nodal, an extracellular signaling molecule involved in cell fate specification [172, 173], increases intercellular adhesion [165], and that cell-cell contacts can in turn enhance the competence of cells to respond to Nodal [72]. Moreover, the external level of Nodal varies spatially, decreasing from the tissue margin to the embryo pole, thus allowing to test if the cells undergo the predicted switch from strong to weak adhesion as a function of the external signal in Eq. (3.29), which thereby acts as the control parameter. While the structure of the zebrafish blastoderm resembles a disordered wet-limit foam with an average of six contacts per cell [174], I model it for simplicity as an ordered lattice with $n = 6$ contacts (cubic) in the small-angle limit, consistent with the data [Fig. 3.13]. Given the typically low concentrations of signaling molecules [175, 176], I model fluctuations of the local level of Nodal by a Gamma distribution, whose mean follows an exponentially decaying profile $\langle\phi(y)\rangle = \phi_0 \exp(-y/\xi)$ from its source at the tissue margin with a characteristic length of $\xi = 40\,\mu\text{m}$ [173]. The variance of the Nodal level $\sigma_\phi^2 = \langle\phi\rangle$ is motivated by the Poissonian statistics of density fluctuations [177, Appendix III]. To test the predictions, our collaborators measured the distribution of cell-cell contact angles θ from fluorescence microscopy images of embryos taken five hours post fertilization at different positions $y_j \geq 0$ along the embryo axis [Fig. 3.12(b)]. I evaluated Eqs. (1.7), (2.72), (2.68), (3.29) at each y_j in the local approximation, i.e. neglecting spatial variations of Nodal across nearest-neighbor cells and any non-local effects of area coupling. Using simulation-based inference [171], I then estimated the three unknown parameters from the samples of θ [Fig. 3.12(b)], obtaining $\gamma_0/2\gamma_\text{f} = 0.87 \pm 0.01$, $\gamma_\text{A}/\gamma_0 = 0.16 \pm 0.03$ and $\chi\phi_0 = 3.1 \pm 0.8$ (standard error from cross-validation). The small value of the ratio γ_A/γ_0 is consistent with Eq. (2.68) being a lowest-order expansion around a constant. Furthermore, genetic perturbation of adhesion regulation in *silberblick* mutants [165, 178, 179] yielded a significant reduction in the adaptive tension coefficient as expected ($\gamma_{\text{A,SLB}}/\gamma_0 = 0.05 \pm 0.01$, inferred with the two other parameters $\gamma_0/2\gamma_\text{f}$ and $\chi\phi$ left unaltered [Fig. 3.12c]).

Overall, I find that the estimated parameters of blastoderm cells are close to the critical cusp point of the bistable regime, which locates the transition between low- and high-contact regimes at approximately 50–70 µm above the margin of the tissue [Fig. 3.12(d), obtained without further fitting]. This length corresponds indeed to the observed size of the subsequently developing rigid tissue region, which at later stages forms the internal parts of the organism [180].

The following sections provide more details about the simulation-based inference approach

as well as justifications for the different modeling assumptions.

3.7.3 Fluorescence imaging of mesendoderm formation in zebrafish

My collaborators, Camilla Autorino and Nicoletta Petridou (EMBL), obtained fluorescence imaging data of wild type (WT) and *silberblick* mutant (SLB) embryos 5 h after fertilization, and measured the contact angles $\theta_j(y_j)$ between cells of the blastoderm at different positions y_j along the AV-axis from the margin at $y = 0$. They obtained $N = 2132$ contact angle datapoints from five WT embryos, and $N = 806$ datapoints from three SLB embryos. I then used Eq. (1.4) to relate the measured contact angles to the steady state tension ratios obtained from simulating the framework of signal processing droplets (see below for details). In particular, I used simulation-based inference (SBI) to infer parameters describing the distributions $p_{\mathrm{WT}}(\cos(\theta/2))$ and $p_{\mathrm{SLB}}(\cos(\theta/2))$ shown in Fig. 3.12(b).

3.7.4 Modeling tissues as wet-limit foams with fixed topology in the small contact angle limit

Camilla Autorino measured the number of in-plane contacts per cell across the blastoderm from 2D microscopy images (as described in [165]), and obtained 4.05 ± 0.05 in the WT and 3.77 ± 0.07 in the SLB mutant [Fig. 3.13(e)](mean±standard error). Extrapolating from these in-plane measurements suggests that blastoderm cells have an average of six neighbors in three dimensions, and that the system is close to the rigidity percolation threshold [165]. Therefore, I model the non-confluent 3D blastoderm tissue as a fixed-topology configuration of droplets with $n = 6$ contacts, which corresponds to the contact number of disordered wet-limit foams close to the jamming/unjamming transition [174]. For the cubic lattice, higher order junctions form at contact angles $\theta \geq 90°$ [Fig. 3.13(b)], corresponding to $\cos(\theta/2) < 1/\sqrt{2}$. Our contact angle measurements show that more than 95% of all data points fall above this point [Fig. 3.13(d, e)]. In this small-angle regime, contact areas are well approximated by linearizing Eq. (1.7) around the tension ratio at detachment $\gamma_{\mathrm{c}}/2\gamma_{\mathrm{f}} = 1$ [Fig. 3.13(d)]

$$\frac{A_{\mathrm{c}}}{A_0} = n 2^{1/3} \left(1 - \frac{\gamma_{\mathrm{c}}}{2\gamma_{\mathrm{f}}}\right) + \mathcal{O}\left(\left(1 - \frac{\gamma_{\mathrm{c}}}{2\gamma_{\mathrm{f}}}\right)^2\right), \tag{3.30}$$

which I used for the parameter estimations.

3.7.5 Cell state dynamics are governed by an external signaling gradient

The blastoderm cells respond to extracellular Nodal signals [72, 173], which I model as an exponentially decaying stochastic concentration field [Fig. 3.12(b)] [173] $\phi(y) = \langle\phi(y)\rangle + \eta(y)$ including a Poissonian noise term to account for molecule fluctuations [177, Appendix III]. For each position y_j at which a contact-angle measurement is available, I solve Eqs. (2.68),(2.72),(2.82) in the local approximation, i.e.

$$\tau_u \frac{du}{dt} = \frac{\left(\chi\phi(y_j)\frac{A_c}{A_0}\right)^h}{1+\left(\chi\phi(y_j)\frac{A_c}{A_0}\right)^h} - u, \tag{3.31}$$

whereby I neglect differences in the external signal received by neighboring cells, and nearest-neighbor variations in the contact areas. The steady states of Eq. (3.31) depend on the parameters $\gamma_0/2\gamma_f$, γ_A/γ_0, the product $\chi\phi$, and the Hill coefficient h.

3.7.6 Simulation-based inference analysis

I used simulation-based inference (SBI) to infer the unknown parameters from the statistics of the measured contact angles across positions and samples [Fig. 3.12(b)]. SBI is particularly suitable for scenarios where the likelihood function is intractable or difficult to compute, but where simulating data from the model is straightforward. Given a set of observations $\mathbf{x}_{obs}$ (here the summary statistics of measured contact angles, see below), SBI relies on Bayes' theorem for the probable set of parameters ϑ describing the data. In particular, I am interested in the posterior distribution

$$p(\vartheta|\mathbf{x}_{obs}) = \frac{p(\vartheta)p(\mathbf{x}_{obs}|\vartheta)}{p(\mathbf{x}_{obs})} \tag{3.32}$$

with $p(\vartheta)$ the prior over the parameters, and $p(\mathbf{x}_{obs}|\vartheta)$ probed by stochastic simulations.

Simulation step. Given a set of model parameter values (Hill coefficient h, the ratios of tension coefficients $\gamma_0/2\gamma_f$ and γ_A/γ_0, and the product $\chi\phi$), my simulator evaluates the steady state of Eq. (3.31) using (2.68) and (3.30), starting from random initial conditions $u(t=0) \in [0,1]$ using *solve_ivp* with the *RK45*-method (explicit fourth order Runge-Kutta) from the *scipy* python package. For each position y at which a contact angle was measured, one simulation was performed. To account for the Poissonian statistics of fluctuating concentrations in the external signal gradient, $\chi\phi$ was drawn from a Γ-distribution with mean $\mu_{\chi\phi} = \langle\chi\phi(y)\rangle$ and variance $\sigma_{\chi\phi} = \langle\chi\phi(y)\rangle$. I used Eq. (1.4) to calculate contact angles from steady state tension ratios and added a relative error of

15% to account for experimental measurement errors by drawing a new contact angle from a normal distribution centered at μ_θ equal to the simulated steady state angle and standard deviation $\sigma_\theta = 0.15\mu_\theta$.

My preliminary analysis revealed that in contrast to the tension and susceptibility parameters, the Hill coefficient was not well constrained by the data, but the shape of the inferred posterior suggests values of $h > 2$ to be most suitable, with a broad peak around $h = 7$ [Fig. 3.15(a)]. Following common convention for biological signaling models, I therefore fixed the Hill coefficient to $h = 4$ [107, 108, 159].

There remain three parameters $\vartheta = (\gamma_0/2\gamma_\mathrm{f}, \gamma_\mathrm{A}/\gamma_0, \chi\phi)$, which can be identified from the measurements and which are assumed distributed with uniform priors

$$\begin{aligned} p(\gamma_0/2\gamma_\mathrm{f}) &= \mathcal{U}([0.7, 1]), \\ p(\gamma_\mathrm{A}/\gamma_0) &= \mathcal{U}([0, 1]), \\ p(\chi\phi) &= \mathcal{U}([0, 20]), \end{aligned} \tag{3.33}$$

where $\mathcal{U}([a, b])$ denotes a uniform distribution on the interval $[a, b]$. The range of baseline tension ratios $\gamma_0/2\gamma_\mathrm{f}$ was chosen such that—considering Eqs. (1.4), (2.68) and $\gamma_\mathrm{A} = 0$—the corresponding values of contact angles cover the range of measurements. I also tested that a broader prior $p(\gamma_0/2\gamma_\mathrm{f}) = \mathcal{U}([0, 1])$ yields the same results, but considerably slows down the inference procedure. The adaptive tension ratio γ_A/γ_0 was sampled from the full domain in which the theory is valid. For $\chi\phi$ I chose an upper limit of 20 (an order of magnitude above $(\chi\phi)_\mathrm{Cusp}$, [Fig. 3.12(a),(c)]), however, the same results were obtained with a larger prior range of $p(\chi\phi) = \mathcal{U}([0, 100])$.

For the analysis of genetically perturbed embryos (SLB mutant), $\gamma_0/2\gamma_\mathrm{f}$ and $\chi\phi$ were fixed to the values inferred from the wildtype data, leaving $\gamma_\mathrm{A}/\gamma_0$ as the only free parameter.

Training As the summary statics $\boldsymbol{x}_\mathrm{obs}$—the features extracted from the measurements or results of simulations—I used the moments

$$\ell_m = \langle \mathcal{L}_m(\cos(\theta/2)) \rangle$$

of the *shifted Legendre polynomials* $\mathcal{L}_m$ of orders $m = 1, 2, ...8$ (order $m = 0$ yields 1 due to the normalization of the probability density), which characterize the marginal distribution of the contact angles $p_\mathrm{WT}(\cos(\theta/2))$ and $p_\mathrm{SLB}(\cos(\theta/2))$ [Fig. 3.14(a,b)].

To include information about the spatial structure in the data, I additionally computed four cross-moments

$$c_{\alpha\beta} = \frac{1}{N} \sum_{j=1}^{N} y_j^\alpha \cos^\beta \left[\frac{\theta(y_j)}{2} \right], \tag{3.34}$$

with $\alpha, \beta \in \{1, 2\}$ and N being the number of data points.

In total, I thus obtained twelve degrees of freedom $\boldsymbol{x}_{\text{obs}}$(8 Legendre moments and 4 cross-moments), which I used to train the posterior estimator $p(\vartheta|\boldsymbol{x}_{\text{obs}})$. To this end, I leveraged the python implementation of the SBI method [171]. In particular, I used the sequential neural posterior estimator (SNPE) with the neural-spline flow representation of distribution functions.

The training set included 5×10^5 simulations of wildtype embryos with three variable parameters sampled from Eq. (3.33), and 10^5 simulations of the *silberblick* embryos. The expected values of the inferred parameters were calculated over 2000 samples from the obtained posterior distribution $p(\vartheta|\boldsymbol{x}_{\text{obs}})$ [Fig. 3.14(c-d)].

To assess the error of the parameter inference arising from sample-to-sample variability between different embryos (reported in the main text and Fig. 3.12(c)), I used cross-validation. Specifically, I computed the standard error of inferred parameter ϑ using *jackknife resampling* [181]

$$\text{std}_\vartheta = \sqrt{\frac{1}{M(M-1)} \sum_{k=1}^{M} \left(\vartheta_{\text{k}} - \langle\vartheta\rangle\right)^2}, \tag{3.35}$$

where M is the number of embryos, ϑ_{k} is the inferred parameter value obtained using all but the data from the k-th embryo for training the neural network to estimate the posterior and $\langle\vartheta\rangle$ is the mean of the M different inferred parameter values.

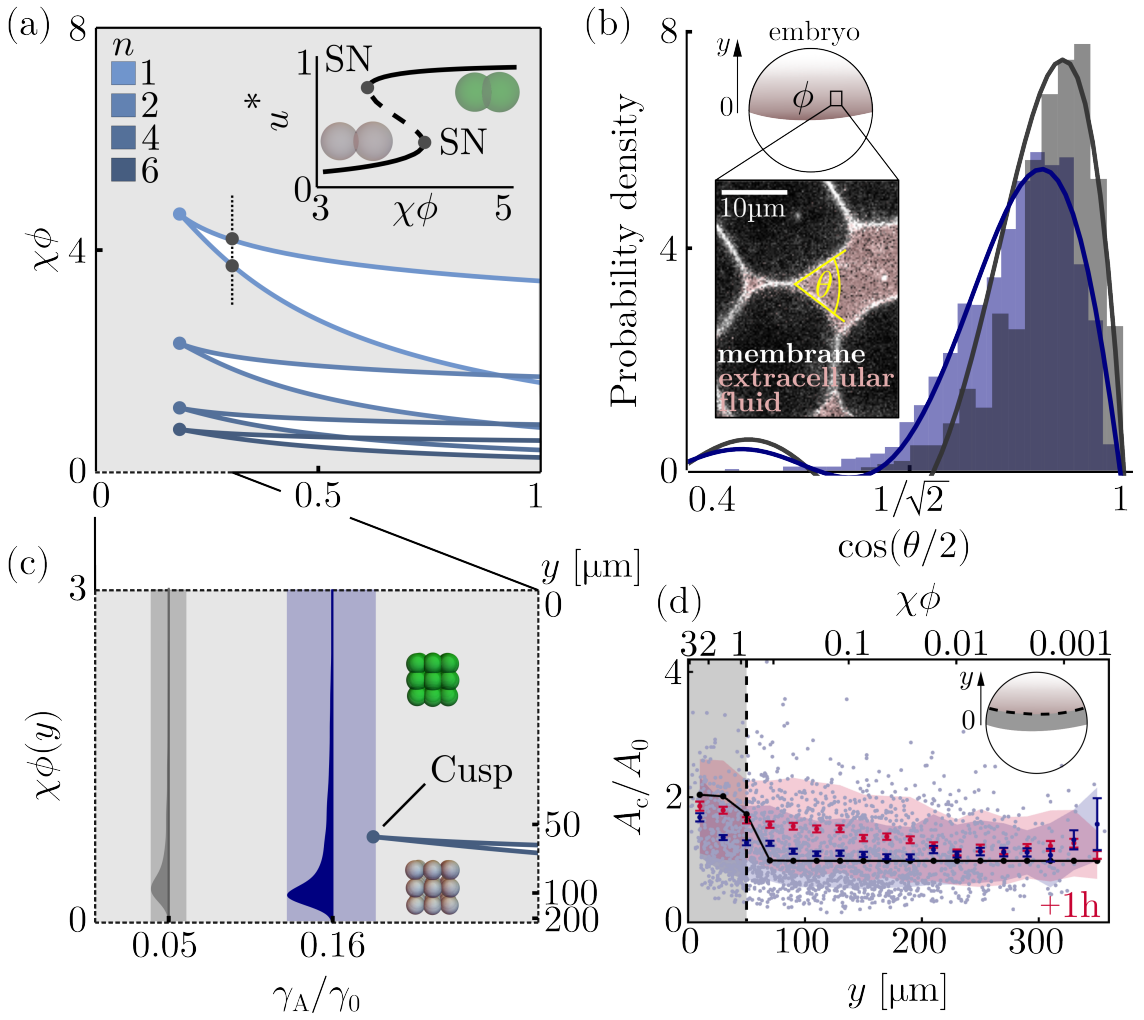

Figure 3.12. Adaptive tension produces a shape transition supporting patterning in zebrafish embryos. (a) Positive feedback between contact-dependent signals and adaptive adhesion produces bistability between small- and large-contact configurations (inset: bifurcation curve along dotted line, n: number of neighbors, blue points: cusps). (b) Cell-cell contact angle measurements θ from fluorescence microscopy images (inset) of blastoderm in unperturbed wildtype zebrafish embryos (blue, 2132 cells from 5 embryos) and *silberblick* mutants with disrupted adhesion regulation (gray, 806 cells from 3 embryos) allow the estimation of parameters $\gamma_0/2\gamma_f$, γ_A/γ_0, and $\chi\phi$ using simulation-based inference ([171] and Section 3.7.6) (solid lines: best fit).(c) The inferred parameter distributions locate wildtype embryos close to the cusp, whereas mutants lose adaptive adhesion (shaded regions: standard error from cross-validation (Section 3.7.6), images for $\gamma_c/2\gamma_f = \{0.87, 0.71\}$). (d) Mapping external signal levels to spatial positions (also right axis in (c)), I predict—without further fitting—a switch from high- to low-contact configurations at $\sim$ 50–70 μm above the tissue margin (inset), matching the size of the subsequently forming rigid tissue (dark blue and red: experimental mean and standard error at consecutive timepoints, shaded areas: standard deviations, dots: individual data points, black: theoretical profile for inferred $\gamma_A/\gamma_0 = 0.16$). (a)–(d) computed using Eq. (3.30).

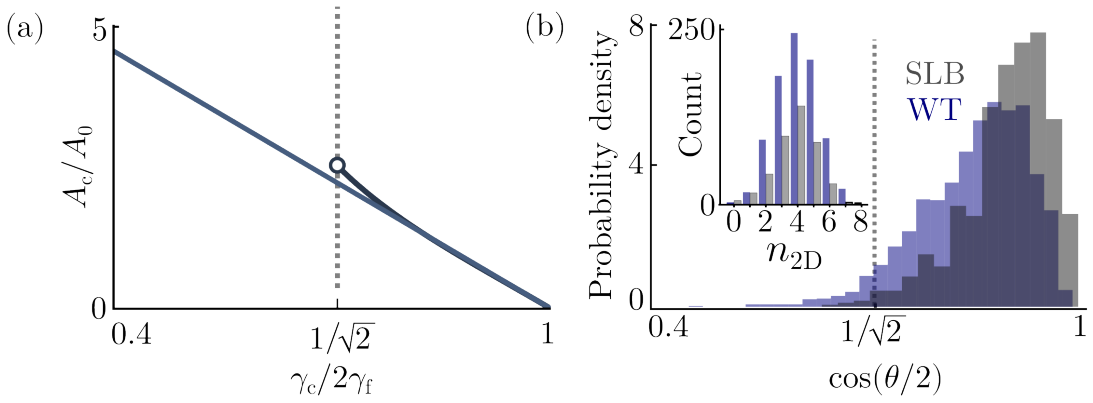

Figure 3.13. (a) Linearization of Eq. (1.7) (solid curve, $n = 6$) around $\gamma_c/2\gamma_f = 1$ (dashed line) provides a good approximation for small contact angles, where the tension ratios are near 1 [Eq. (3.30)]. (b) Contact angle measurements in zebrafish embryos show that the data is well described by the small angle limit for cubic droplet configurations (95.22% of WT and 98.75% of SLB data points are above $1/\sqrt{2}$, the threshold for higher order junction formation). Inset: Histogram of the number of contacts per cell measured from 2D microscopy images n_{2D}. WT: $N = 871$, SLB: $N = 429$. Data acquired by Camilla Autorino (Petridou group, EMBL).

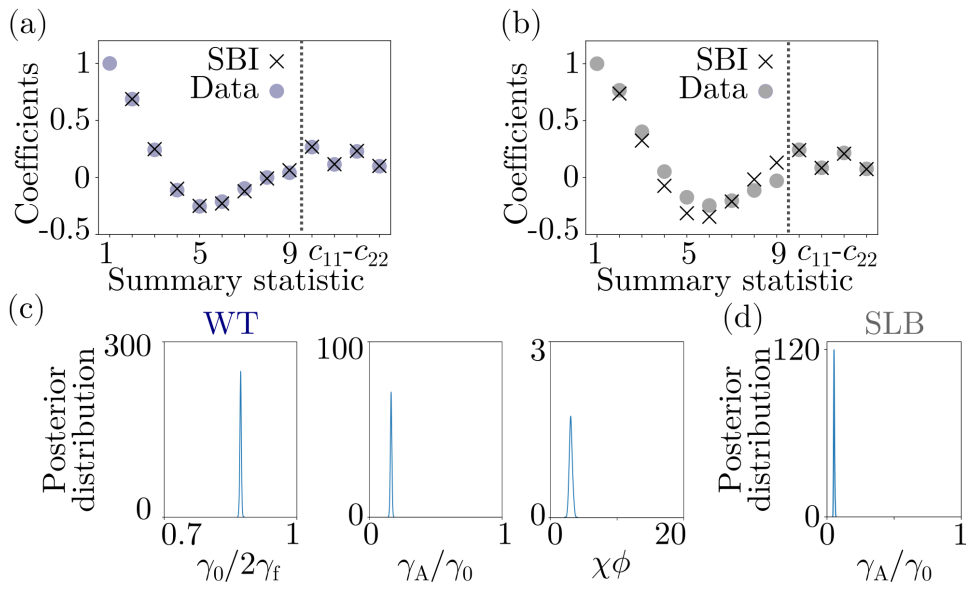

Figure 3.14. SBI analysis of contact angle distributions. (a, b) Data: Legendre and cross-moment coefficients [Eq. (3.34)] of the measured distribution of $\cos(\theta(y)/2)$ [Fig. 3.12(b)], SBI: Inferred parameters were used to simulate distributions of $\cos(\theta(y)/2)$, from which Legendre and cross-moment coefficients were computed. Error bars representing the standard deviation of the posterior are too small to be displayed due to the narrow posterior distributions (compare to c, d). (c, d) Distribution of parameter predictions from sampling the trained posterior 2000 times for the wild type (c) and SLB mutant data (d).

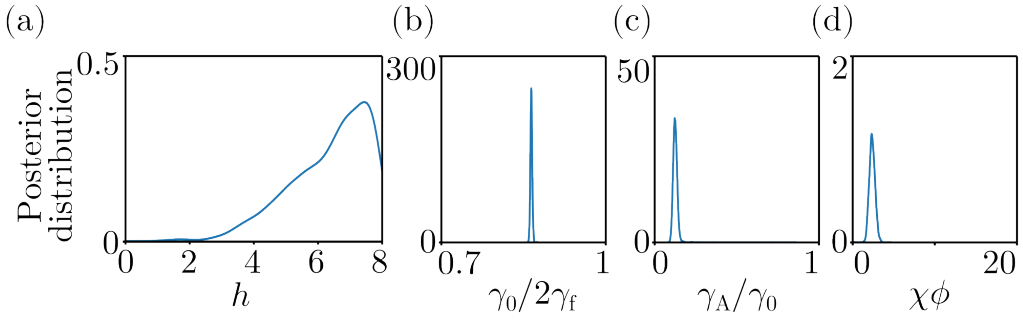

Figure 3.15. Posterior distributions of four model parameters inferred using simulation-based inference (SBI) on WT data. (a) Hill coefficient h, (b) ratio $\gamma_0/2\gamma_f$ (c) ratio γ_A/γ_0, and (d) $\chi\phi$. While parameters (b–d) are well constrained by the data ($\gamma_0/2\gamma_f = 0.864 \pm 0.002$, $\gamma_A/\gamma_0 = 0.13 \pm 0.03$, $\chi\phi = 2.3 \pm 0.4$, errors are the standard deviations of the posterior), the Hill coefficient h remains poorly constrained, though the analysis suggests that $h > 2$ best describes the system. Distributions were obtained by sampling the posterior 2000 times. I used priors as given in Eq. (3.33) for parameters (b-d) and a prior of $p(h) = \mathcal{U}([0, 8])$ for the Hill coefficient, otherwise SBI analysis was performed as described in Section 3.7.6.

Chapter 4

Contact topology-driven signaling dynamics

In the previous chapter, I analyzed the feedback dynamics between contact-based signaling and shape adaptation on the level of adherent droplets, droplet pairs, and regular droplet lattices. In physical systems, e.g. multicellular structures and tissues, contact topologies can be much more diverse, i.e. spatially heterogeneous and dynamically evolving over time. In proliferating matter, even the number of interacting constituents can vary over time, adding another level of complexity [26].
In this chapter, I study this additional layer of complexity by focusing on systems where the contact topology is a fixed parameter or a data-derived, autonomously developing function over time. In particular, motivated by the Notch lateral inhibition pathway [69], I start with a linear stability analysis of a minimal model of mutually inhibitory contact-dependent signaling. I show how the patterning of states depends on the coupling strength, the length scale of coupling, and how coupling asymmetries can generate traveling pattern defects.

To generalize long-range coupling interactions, I introduce a kernel function that represents the distance over which cells can interact, i.e. send and receive signals from other units, and I apply this framework to describe cell fate patterns observed in the developing neuromasts, a sensory organ in the skin of fish.

Moreover, together with collaborators from the Jacobo group (CZ Biohub, San Francisco), I have analyzed realistic contact networks derived from live microscopy data of developing neuromasts. I will show that simulations of contact-dependent signaling on these networks suggest that cell differentiation patterns can be predicted in time and space.

4.1 Contact-based fate patterning in one dimension

Consider a periodic system of N interacting cells, each with an internal state $u_i \in [0,1]$ [Fig. 4.1]. Cell states u_i change over time according to a set of N differential equations

$$\tau_u \frac{d\vec{u}}{dt} = \begin{pmatrix} f_1(u_1, u_2, ...) \\ ... \\ f_N(u_1, u_2, ...), \end{pmatrix} \tag{4.1}$$

where the vector $\vec{u} = (u_1, u_2, ..., u_N)$ contains the states of all N cells. In the following, I assume that

$$f_i(u_1, u_2, ...u_N) = \frac{1 + \tanh(k(u_i - s_i))}{2} - u_i, \tag{4.2}$$

where $s_i \in \mathbb{R}^+$ denotes the signal that a cell i receives from all other cells and $k > 0$ is a free parameter that determines the degree of nonlinearity—i.e. the steepness—of the cellular response to the received signal s_i [67]. The minus sign assures that signals are inhibitory: signals prevent a cell from reaching a signal-sending high u state. Eq. (4.2) has been used successfully to model the Notch signaling pathway [67, 68], where a high u value describes a signal sending state (high ligand expression), while low u corresponds to a signal receiving state (low ligand expression). It differs from Eq. (2.73) derived in Chapter 2 in two aspects: (i) the nonlinear response function uses a hyperbolic instead of a Hill function and (ii) the response function contains the internal state of the signal receiving cell. While the choice of the sigmoid response function is somewhat arbitrary and only has minor impact on the results—as long as the degree of nonlinearity is comparable—the latter aspect introduces a crucial difference. In [67], including u in the response function was motivated by *Cis-inhibition*: ligands expressed on a cell surface can laterally bind to receptors of the same cell, preventing them to bind and be activated by ligands of neighboring cells (*Trans-activation*). Thereby, two cells expressing higher levels of Notch ligand can form physical contacts without breaking symmetry: their ligands inhibit their own receptors, effectively decoupling the two interacting cells. Cis-inhibition creates a positive feedback loop: increasing the ligand expression increases the fraction of impaired receptors, which prevents the cell from receiving inhibitory signals and promotes further

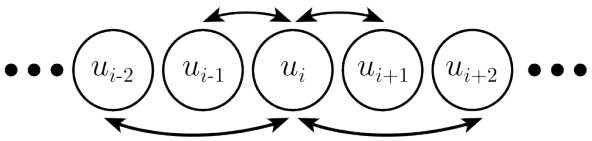

Figure 4.1. Periodic chain of N interacting units, each with an internal state u_i, which can be coupled over arbitrary distances.

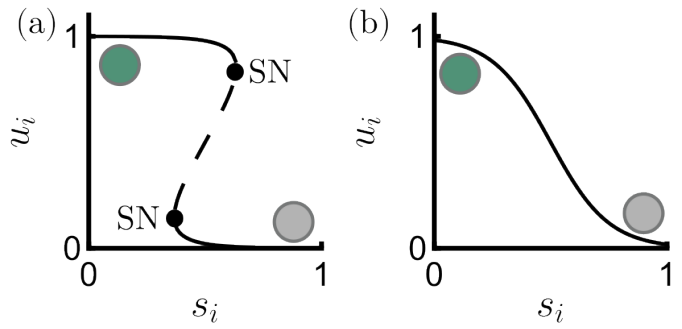

Figure 4.2. (a) The steady-state solutions of Eq. (4.2) for varying signal s_i show a bistable regime. (b) Without the positive feedback from Cis-inhibition, no bistability is observed (shown are the solutions of $u_i = (1 + \tanh(4(0.5 - s_i)))/2$).

expression of ligands. If the positive feedback is strong enough, it creates a bistability, where the same input signal can drive a cell into a signal-sending or -receiving state [Fig. 4.2]. However, this bistability is not necessary to achieve symmetry-breaking of states between interacting cells. The signal

$$s_i = \chi \sum_j u_j c_{ij} \tag{4.3}$$

is defined as the sum over all cells, where c_{ij} is a symmetric matrix describing how cell i is coupled to cell j. In the following, I generally assume that $c_{ii} = 0$ for all i, because cells are not self-signaling, however, the Cis-inhibition term could also be introduced as negative, diagonal elements in the coupling matrix. The coupling is multiplied by the respective signaling state u_j and the signal susceptibility χ. Equation (4.3) is similar to the definition of the signal presented in [67], but with a linear ligand activity, i.e. the potential of a cell to send signals is proportional to its state u.

In the following sections, I consider different coupling topologies c_{ij} for a periodic chain of cells, and I study how state patterning changes with varying signal susceptibility. Specifically, I use linear stability analysis around uniform and patterned states to distinguish patterning and non-patterning regimes and to determine patterning length scales.

4.2 Linear stability analysis of state patterning

Assume that $\vec{u}^* = (u^*, u^*, \ldots, u^*)$ is a uniform steady state with $du^*/dt = 0$. It can be shown that for each combination of parameters k and χ a unique uniform stationary state exists [Appendix L]. Close to the uniform state, the time evolution of a small perturbation

δu_i from the uniform state follows

$$\delta \dot{u}_i = \Gamma \delta u_i + \sum_{j \neq i} \omega_{ij} \delta u_j, \tag{4.4}$$

where I defined the partial derivatives

$$\Gamma = \left.\frac{\partial f_i}{\partial u_i}\right|_{\vec{u}^*} = \frac{k}{2\cosh^2(k(u_i - s_i))} - 1, \tag{4.5}$$

$$\omega_{ij} = \left.\frac{\partial f_i}{\partial u_j}\right|_{\vec{u}^*} = \frac{-k}{2\cosh^2(k(u_i - s_i))} \frac{\partial s_i}{\partial u_j}, \tag{4.6}$$

to shorten the notation. Introducing the N discrete Fourier components η_q corresponding to the wave numbers q/N with $q \in (0, 1, \ldots, N-1)$ allows to express perturbations around the uniform state as

$$\delta u_i = \sum_{q=0}^{N-1} \exp\left(\frac{2\pi I}{N} iq\right) \eta_q, \tag{4.7}$$

where I represents the imaginary unit. From Eqs. (4.4),(4.7) follows

$$\frac{d\eta_q}{dt} = \frac{\Gamma}{N} \sum_{r=0}^{N-1} \sum_{i=1}^{N} \exp\left(\frac{2\pi I}{N} i(r-q)\right) \eta_r + \frac{1}{N} \sum_{r=0}^{N-1} \sum_{i=1}^{N} \sum_{j \neq i} \omega_{ij} \exp\left(\frac{2\pi I}{N}(jr - iq)\right) \eta_r. \tag{4.8}$$

Using the relation

$$\sum_{i=1}^{N} \exp\left(\frac{2\pi I}{N} ir\right) = \begin{cases} 0, & \text{if } 0 < r < N \\ N, & \text{if } r \equiv 0 \pmod N \end{cases} \tag{4.9}$$

allows to rewrite Eq. (4.8) as

$$\dot{\eta}_q = \Gamma \eta_q + \frac{1}{N} \sum_{r=0}^{N-1} \sum_{i=1}^{N} \sum_{j \neq i} \omega_{ij} \exp\left(\frac{2\pi I}{N}(jr - iq)\right) \eta_r. \tag{4.10}$$

In the following, I compute the dispersion relation, i.e. the growth rates of the discrete Fourier components, for different examples of coupling c_{ij}.

4.3 Coupling to nearest neighbors

First, consider that each cell i only receives signals from its direct neighbours $i+1$ and $i-1$, represented by the coupling matrix

$$c_{ij} = \begin{cases} 1, & \text{if } |i-j| = 1 \\ 0, & \text{otherwise.} \end{cases} \tag{4.11}$$

It follows for the evolution of small perturbations around the uniform state

$$\delta\dot{u}_i = \Gamma\delta u_i + \omega(\delta u_{i-1} + \delta u_{i+1}) \tag{4.12}$$

with

$$\omega = \frac{-k\chi}{2\cosh^2(ku^*(1-2\chi))}. \tag{4.13}$$

Using Eq. (4.9), it follows for the dynamics in Fourier space

$$\dot{\eta}_q = \Gamma\eta_q + 2\omega\cos\left(\frac{2\pi}{N}q\right)\eta_q. \tag{4.14}$$

Dynamics for the Fourier modes are completely decoupled, thus, they are eigenmodes of the linearized, differential system. Using the ansatz $\eta_q \propto \exp(\sigma_q t)$ yields the dispersion relation

$$\sigma_q = \Gamma + 2\omega\cos\left(\frac{2\pi}{N}q\right) \tag{4.15}$$

for the exponential growth rate σ_q.

From $\omega < 0$ follows that σ_q is maximal at $q = N/2$ ($(N \pm 1)/2$ for odd N) [Fig. 4.3], i.e. the condition for patterning is $0 < \Gamma + 2\omega$ and the fastest growing mode is that of a period two pattern with alternating high and low state values [Fig. 4.3(a)], as typical for Notch lateral inhibition. Note that changing the sign in front of the signal s in Eq. (4.2) would correspond to a system where cells exchange activating instead of inhibitory signals. Such a mutual positive feedback favors uniform states, and accordingly in that case σ_q is maximal for $q = 0$.

The linear stability analysis, performed here around uniform states, can analogously be conducted for any patterned state, for example, for alternating patterns of high and low value states. In that case, however, the Fourier modes are not the eigenmodes of the linearized system. Note that the uniform state is a special case of an alternating pattern in which the alternating states are identical. Thus, linear stability analysis of the alternating pattern allows to identify the bifurcation types that mark the transition between uniform and patterned regimes [Fig. 4.4]. The bifurcation type depends on whether the positive feedback due to Cis-inhibition is included in Eq. 4.2. Without the feedback, the system transitions from uniform to patterned state via a supercritical pitchfork bifurcation [Fig. 4.4(c, d)]. However, including the feedback leads to a bistable regime [Fig. 4.4(a, b)], in which uniform and patterned states coexist, with a transition between uniform and patterned state that is marked by a combination of subcritical pitchfork and saddle node bifurcations. Note that the scope of patterned states explored in this brief analysis is not exhaustive: depending on the parameters other steady state patterns can exist that deviate from a perfectly regular alternating state pattern.

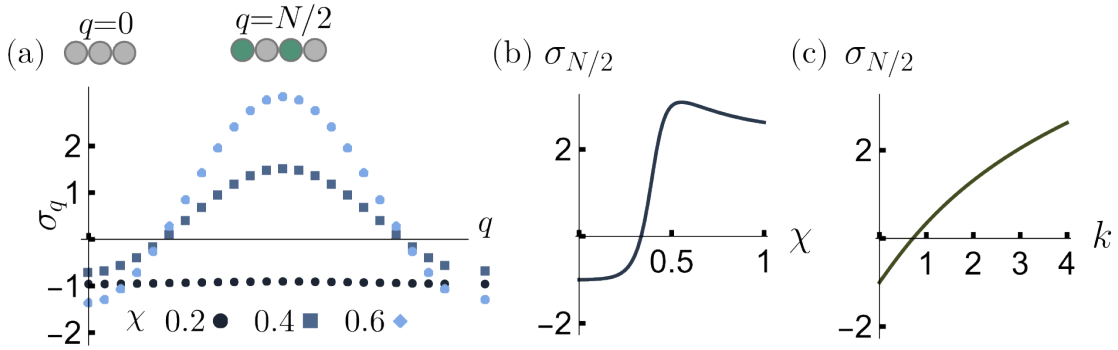

Figure 4.3. The growth rate of the discrete Fourier modes σ_q, given symmetric nearest neighbor coupling [Eq. (4.11)], is maximal at $q = N/2$ (a) and generally increases with the signal susceptibility (b) and the degree of nonlinearity k (c). N=24, $k = 4$ (b), $\chi = 1$ (c).

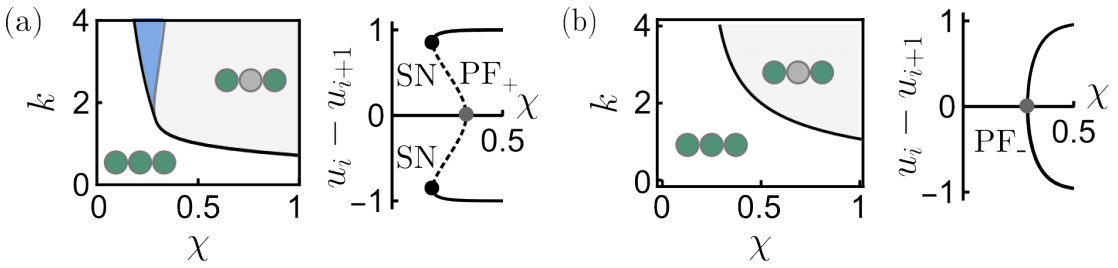

Figure 4.4. (a) State diagram (left) and bifurcation diagram ($k = 4$) for contact-signaling with Cis-inhibition. White: stable uniform state. Gray: stable alternating patterns, blue: multistability of uniform and patterned states. The bifurcation diagram shows a subcritical pitchfork at the transition between uniform and patterned states. (b) Without Cis-inhibition term, the transition is marked by a supercritical pitchfork bifurcation (here $k = 4$).

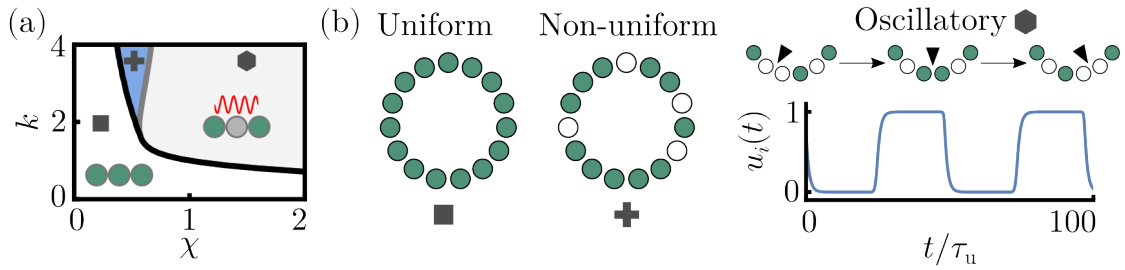

Figure 4.5. (a) State diagram for asymmetric coupling [Eq. (4.16)]. The system can oscillate if the total number of cells N is odd. (b) Steady states (Square, Plus) from simulations with random initial conditions $u_i \in [0, 1]$ for parameters as marked in (a). Traveling defects cause cell state oscillations with non-sinusoidal wave form (Hexagon).

4.4 Asymmetric coupling

Active processes allows cells to break spatial symmetries, for instance, to recruit molecules to specific cell site. In the following, I consider such an asymmetrically coupled system, e.g. polarized cells, where each cell recruits its receptor and ligand molecules to opposite poles. In particular, I consider the coupling matrix

$$c_{ij} = \begin{cases} 1, \text{ if } j = i - 1 \\ 0, \text{otherwise,} \end{cases} \tag{4.16}$$

where each cell only receives signal from one of its neighbors. The corresponding dispersion relation is

$$\sigma_q = \Gamma + \omega \cos\left(\frac{2\pi}{N} q\right) - \omega I \sin\left(\frac{2\pi}{N} q\right). \tag{4.17}$$

The imaginary term indicates that the system can experience global oscillations. However, in case of even N, the fastest growing mode $q = N/2$ has vanishing angular frequency, and simulations confirm that the alternating pattern of high and low state values is indeed a stable state for sufficiently large χ and k. In case of odd N, the $N/2$ mode does not exist. Because all unstable modes have a non-zero imaginary part, the system is expected to undergo sustained oscillations. Indeed, for sufficiently large k and χ, simulations show self-sustained oscillations with non-sinusoidal wave form due to traveling patterning defects [Fig. 4.5(b)]. Note that the imaginary part of the dispersion relation [Eq. (4.17)] is insufficient to capture the oscillation period, as it only captures dynamics close to the uniform state, but not the strong nonlinearities underlying the wave form [Fig. 4.5(b)]. In the bistable regime, where uniform and non-uniform stable states coexist, most simulations converge to heterogeneous steady states [Fig. 4.5, plus]. Because of the bistability that originates from the Cis-inhibition term [Fig. 4.2(a)], steady states

can maintain mutually interacting signal-sending cells, which promotes the stability of heterogeneous patterns [Fig. 4.5(b)].

4.5 Coupling beyond nearest neighbors

Even in densely packed systems, cells can exchange contact-based signals over a distance of several cell diameters due to the formation of signaling protrusions [94, 182]. In the following, I consider a corresponding scenario by introducing the coupling term

$$c_{ij} = \begin{cases} \dfrac{1}{1+\beta}, & \text{if } |i-j| = 1 \\ \dfrac{\beta}{1+\beta}, & \text{if } |i-j| = 2 \\ 0, \text{otherwise}, \end{cases} \tag{4.18}$$

where β describes the ratio between short and longer range coupling [Fig. 4.6(a)]. Linearization of the state dynamics around the uniform state leads to the dispersion relation

$$\sigma_q = \Gamma + \frac{2\omega}{1+\beta}\cos\left(\frac{2\pi}{N}q\right) + \frac{2\omega\beta}{1+\beta}\cos\left(\frac{2\pi}{N}2q\right). \tag{4.19}$$

The discrete Fourier modes are still the eigenmodes of the linearized system, independent of the length scale over which cells interact. Because of the additional cosine term in Eq. (4.19), the fastest growing Fourier mode

$$\frac{q_{\max}}{N} = \frac{\arccos\left(-\frac{1}{4\beta}\right)}{2\pi} \tag{4.20}$$

depends on the ratio between short and long range coupling β [Fig. 4.6(b, c)]. From Eqs. (4.19), (4.20) follows for $\beta > 0.25$ the stability criterion of the uniform state

$$0 < \frac{k}{2\cosh(ku^*(1-2\chi))^2}\left(1 + \chi\frac{1+8\beta^2}{4(\beta+\beta^2)}\right). \tag{4.21}$$

Interestingly, close to the instability threshold of the uniform state, patterned states are observed for small or large coupling ratio β (with different fastest growing modes leading to different types of pattern), but disappear for intermediate values of β, where long and short range coupling are comparable [Fig. 4.6(c, d)].

4.6 Generalized, non-local signaling interactions

When the signal processing time scale is slow or comparable to the time scale of cellular movements, then cells can interact over even longer distances via migration and integration of signals. To describe such scenarios, in which cells can effectively communicate over

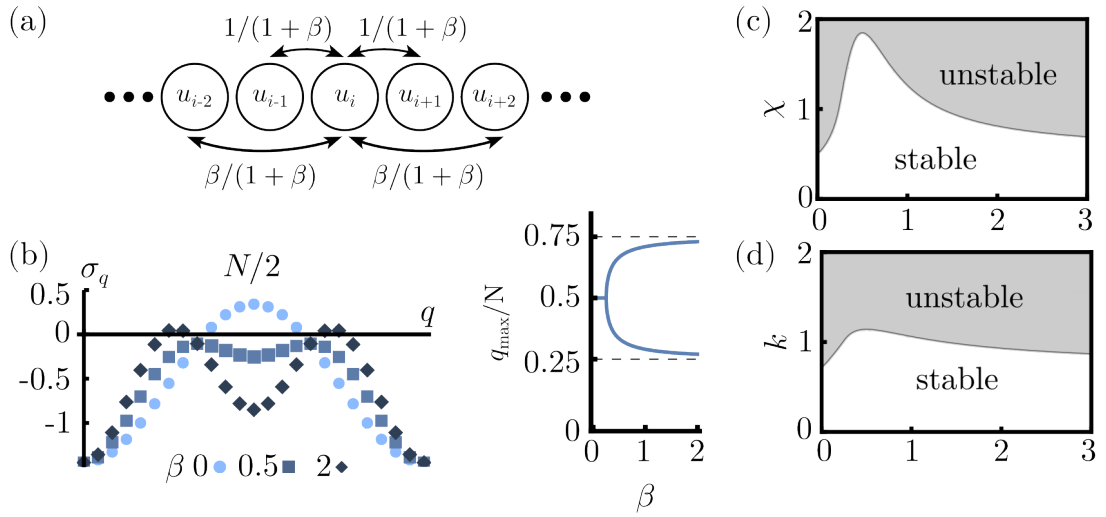

Figure 4.6. Short vs. long range coupling [Eq. (4.18)]. (a) β describes the ratio between short and longer range signaling interactions. (b) The dispersion relation (left) and the fastest growing Fourier mode $q_{\max}$ (right) close to the uniform state depend on β, $k = 1, \chi = 1$. (c,d) Linear stability diagram of the uniform state ($k = 1$ (c), $\chi = 1$ (d)).

much longer distances, I consider that the location probability of each cell i is represented by a *kernel* of the form

$$k_i(x) = \frac{1}{\sqrt{2\pi\lambda^2}} e^{-\frac{(x-x_i)^2}{2\lambda^2}}, \tag{4.22}$$

a normalized Gaussian centered at position x_i with variance λ^2. The coupling c_{ij} between two cells i and j is calculated as the convolution of their respective kernels in space

$$c_{ij} = \int k_i(x) k_j(x) dx = \frac{1}{\sqrt{4\pi\lambda^2}} e^{-\frac{(x_i-x_j)^2}{4\lambda^2}}. \tag{4.23}$$

It represents the spatially integrated interaction probability of two cells, given that their kernels are independent. Within the 1D chain model [Fig. 4.1], I assume that the centers of the cellular kernels are equally spaced with distance Δx and that every cells has the same kernel of variance λ^2. It is natural to assume that the kernel function $k_i(x)$ decays on a length scale much smaller than the system size ($\lambda << (N/2)\Delta x$), as otherwise cells would be coupled multiple times due to the periodic boundary condition. The above assumptions imply that

1. $c_{ii} = 0 \,\forall\, i$
2. $c_{ij} = c_{ji} \,\forall\, i, j$
3. $c_{ij} = c_{i+n,j+n} \,\forall\, n \in \mathbb{Z}, \forall\, i, j,$

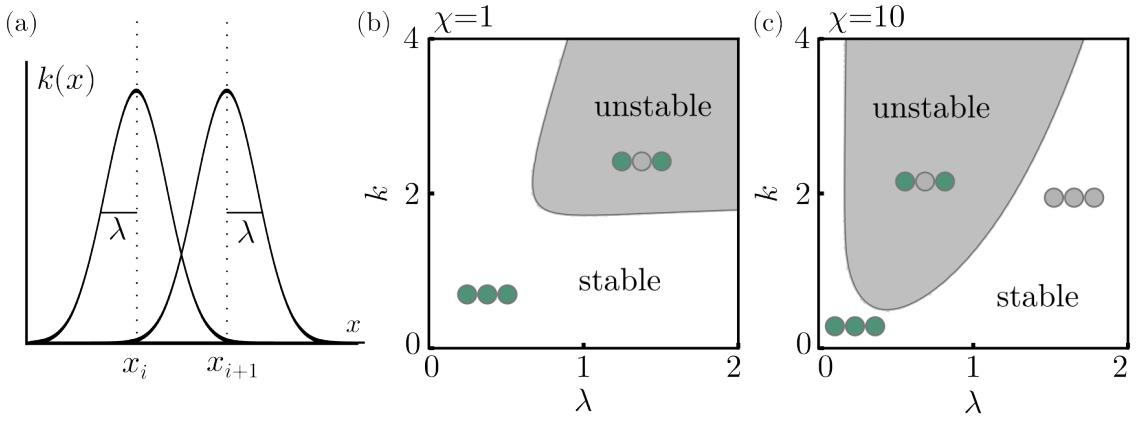

Figure 4.7. Non-local signal interactions described by kernel functions. (a) Each cell is represented by a Gaussian probability function in space centered around its mean position x_i and with standard deviation λ defining a coupling length scale. (b) For sufficiently large signal susceptibility, short and long range coupling between cells can stabilize the uniform states, while intermediate values of λ induce pattern formation.

where the last two conditions can also be expressed as $c_{ij} = c_{ij}(|i-j|)$, i.e. the coupling is symmetric and only depends on the absolute distance $|i-j|\Delta x$. From Eq. (4.10) follows for the dynamics in Fourier space

$$\dot{\eta}_q = \Gamma\eta_q + \frac{1}{N}\sum_{r=0}^{N-1}\sum_{i=1}^{N}\sum_{\alpha=-\frac{N}{2}+1}^{\frac{N}{2}-1}\omega_{i(i+\alpha)}\exp\left(\frac{2\pi I}{N}i(r-q)\right)\exp\left(\frac{2\pi I}{N}\alpha q\right)\eta_r, \tag{4.24}$$

in which I defined the new variable $\alpha = j - i \in \mathbb{Z}$. Due to property 3. of c_{ij} (and ω_{ij}), $\omega_{i(i+\alpha)}$ only depends on α, and we can shorten the notation as $\omega_\alpha = \omega_{0\alpha}$. Using Eq. (4.9) and the symmetry of ω_{ij} yields the dispersion relation

$$\sigma_q = \Gamma + \sum_{\alpha=1}^{\frac{N}{2}-1} 2\omega_\alpha \cos\left(\frac{2\pi}{N}\alpha q\right). \tag{4.25}$$

The stability diagram for the coupling term Eq. (4.23) is shown in Fig. 4.7. Interestingly, when the signal susceptibility is sufficiently strong, a similar trend as for the coupling Eq. (4.18) can be observed: for very small λ, i.e. short range interactions, cells are decoupled and all acquire a high u state. In the intermediate coupling range, uniform states are unstable, however, for large values of λ, the uniform state is stable again with signals sufficiently strong and spread through the system such that all cells are kept in the same low u state.

4.7 Non-local signaling interactions in 2D

While the one-dimensional model allows to explore first principles of topology-driven patterning, the full complexity emerges at the multicellular stage in higher dimensions. One can easily generalize the coupling term Eq. 4.23 to d-dimensional space by considering probability functions $k(\vec{x})$ with $\vec{x} \in \mathcal{R}^d$ and integration over d dimensions. Here, patterning becomes more complex, for instance, when cell-cell coupling is anisotropic. Note that a single signaling kernel does not need to represent individual cells, but could also describe the spatial signaling activity of groups of cells as one unit.

Figure 4.8 presents simulations with different, but constant kernel size parameters $\vec{\lambda}$ (which is now a vector given that higher dimensional kernels can be anisotropic). Cells at the boundary were fixed to $u = 1$ and isotropic kernel parameter $\vec{\lambda} = (0.6, 0.6)$, thus, preventing other units to reach high u values in their vicinity. Note that in systems with open, non-periodical boundary conditions, cells at the boundary reach high u values as they have less neighbors sending an inhibitory signal. Similarly, it was shown for the mechanosensory epithelium of the chick inner ear that smaller cells, which share an accordingly smaller contact area with their neighbors, have a higher probability to acquire the primary cell fate [73]. For identical, isotropic kernels, the framework recovers the typical mosaic patterns of lateral inhibition, where cells of high state u are surrounded by cells of low u [Fig. 4.8, left] [140]. Introduction of anisotropic kernels with $\lambda_x \neq \lambda_y$ translates into globally anisotropic patterns, e.g. a different average spacing of high u cells in x and y directions [Fig. 4.8, center]. In biological systems, these axes can be considered as previously established symmetries maintained by external cues or complementary signaling fields like the PCP pathway [78]. Instead of anisotropic cell morphologies, such kernels can also represent the effects of biased intracellular recruitment of receptors and ligands to particular regions of the membrane. Alternatively, signaling dynamics can vary locally due to lateral diffusion or clustering of receptors and ligands at the membrane [74, 167]. Spatially varying properties of the cellular environment, e.g. the ECM composition, could influence the signaling dynamics either directly [183] or indirectly due to changes in cellular morphology, motility or proliferation [184], and result in patterns differing on comparable length scales. In the signaling kernel, this is reflected by a spatially varying kernel parameter [Fig. 4.8, right], which leads to patterns changing along similar distances.

The simulation framework confirms that the kernel model can capture established modes of contact-dependent Notch signaling like the mosaic patterns typical for lateral inhibition. Moreover, the simulations show that the model contains the flexibility to explore

a broader range that arises from consideration of cellular morphology and cell dynamics on timescales that are small compared to the signaling dynamics. In the following sections I introduce my collaboration on fate patterning in the zebrafish neuromast. Here, I also exploited the capacity of the kernel model to predict how the orientation of cells with anisotropic morphology translates into a global bilateral organ symmetry through contact-dependent signaling (Section 4.13).

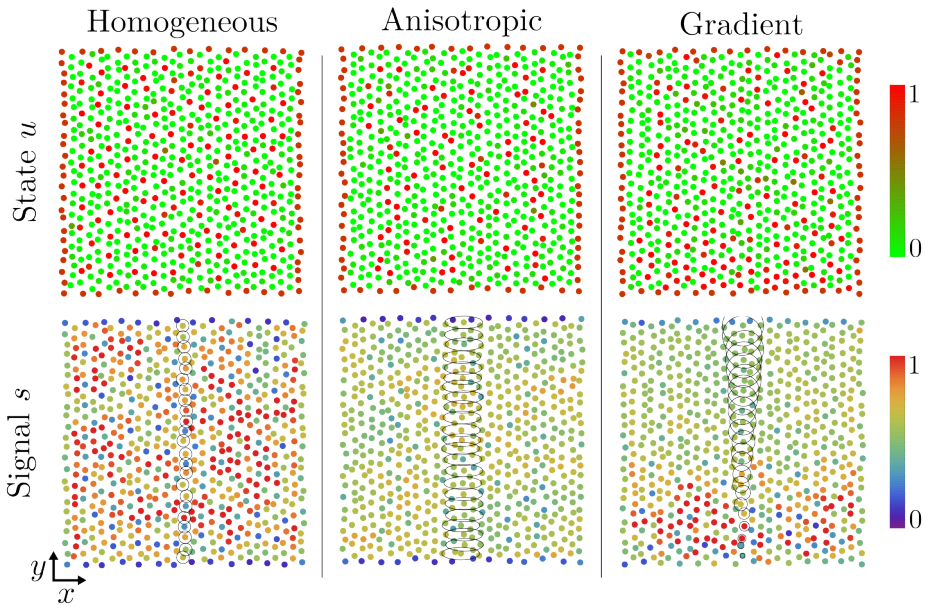

Figure 4.8. (a) Simulations of the two-dimensional kernel model. Cells were initialized on a perturbed hexagonal grid with random initial $u \in [0.1, 0.3]$ and fixed $u = 1$ at the boundary. Top row shows the cell states u, the bottom row the received signal s after a simulation time $t_{\max}$. Kernels are indicated for the vertical midline cells - units with the same y coordinate share the same kernel geometry. Simulations were run with isotropic (left), anisotropic (center) or spatially varying (right) signaling kernels.

4.8 Simulation-based analysis of data-derived contact networks

The lateral line, a mechanosensory epithelium in the skin of fish, has emerged as a model system to study sensory organ development and regeneration (Section 1.2.5) [76, 77, 78]. Distributed along the lateral line are small organs called neuromasts that allow the fish to detect changes in the surrounding water flow [Fig. 4.9(a)]. Neuromasts are initially deposited by a migrating group of cells—the primordium—that originates near the otic vesicle. As it moves posteriorly along the trunk of the developing fish embryo, clusters

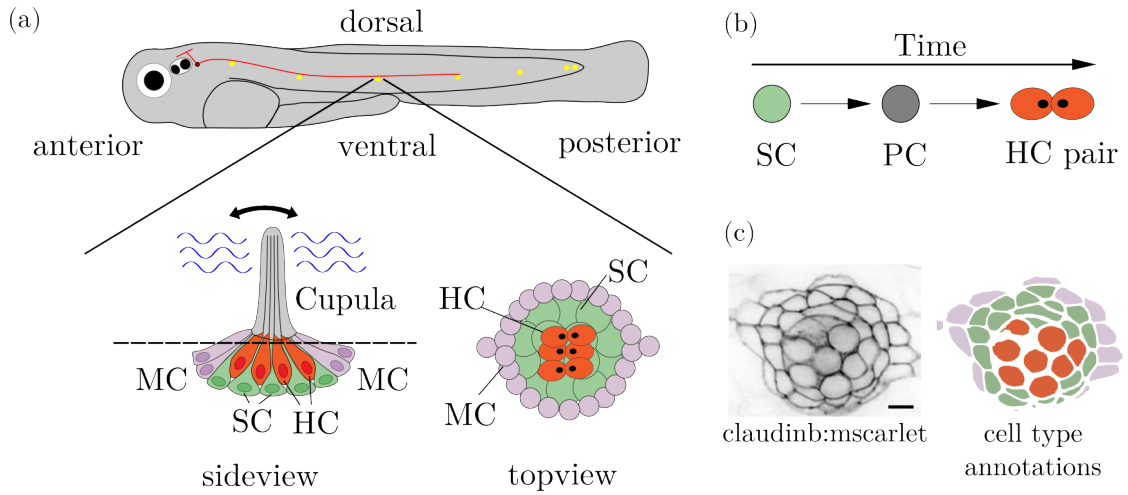

Figure 4.9. (a) Top: Schematic of a larval zebrafish. The red line indicates the lateral line, the yellow dots the neuromasts. A neuromast is a mechanosensitive organ in the skin that consist of hair cells (HC), supporting cells (SC) and surrounding mantle cells (MC). The HC sense deflections of the cupula due to water currents. The topview presents the perspective gained from imaging the plane indicated in the sideview. (b) During development and regeneration, some support cells (SC) develop into progenitor cells (PC), performing a single cell division and producing a pair of sensory hair cells that aligns along the anteroposterior axis. (c) Left: Microscopy image of a zebrafish neuromast with fluorescently marked cell membranes. Right: manual cell-type annotation of segmented cell volumes. Scale bar: 5 µm. Image and annotations by Akilandeswari Balasubramanian (Jacobo group).

of cells are periodically deposited which later form the neuromasts. The migration and patterning of the primordium as well as the further growth and development of the neuromasts are tightly regulated by a complex interplay of signaling pathways, including Wnt, Fgf, and Notch [185].

Within each neuromast, a group of sensory cells called hair cells (HC) occupies the central region [Fig. 4.9(a)]. On their apical surface, hair cells possess mechanosensitive structures called hair bundles, which extends into a gelatinous cap (*cupula*) that protrudes into the surrounding water. Bending of the hair bundles elicits a neuronal response and enables the fish to detect minute water movements. The hair cells are surrounded by supporting cells (SC), which play a crucial role in maintaining the functional structure of the neuromast and serve as progenitors for hair cell development and regeneration [185]. A subtype of support cells, called mantle cells (MC), forms the outer most layer of these organs.

4.9 Hair cell differentiation

The specification of hair cells within the zebrafish neuromast is a tightly regulated process that involves the interplay of multiple signaling pathways, including Notch [78, 185]. The differentiation process follows a characteristic sequence [Fig. 4.9(b)]: a supporting cell (SC) first transitions into a progenitor cell (PC), which then divides symmetrically to form two daughter cells. Initially, both daughter cells are equivalent, but through Notch-mediated lateral inhibition, they break symmetry to develop into two distinct sensory subtypes [68]. Once specified, these two hair cells undergo physical separation, facilitated by intercalation of neighboring supporting cells and possibly guided by heterotypic interactions [87] (Section 1.2.5, Fig. 1.2(c)). This process ensures that hair cells are properly arranged in the neuromast while maintaining an appropriate balance between sensory hair cells and supporting cells.

The ratio between hair and supporting cells has been shown to depend on contact-mediated Notch signaling [78]. In particular, this balance is thought to be maintained through lateral inhibition, where differentiating hair cells express Delta ligands (e.g. deltaA, deltaD [186]), which activate Notch receptors in neighboring cells and suppress their differentiation potential [86, 187]. Ensuring that only a subset of supporting cells adopts the hair cell fate preserves the structural and functional integrity of the neuromast. Inhibition of Notch signaling using $\gamma-$secretase inhibitors like N-[N-(3,5-Difluorophenacetyl)-L-alanyl]-S-phenylglycine t-butyl ester (DAPT) results in an overproduction of hair cells at the expense of supporting cells [86]. Conversely, overactivation of Notch signaling leads to a reduction in hair cell numbers [188]. During development, Notch3 is the predominant receptor expressed in supporting cells [86]. Its activation leads to the transcriptional repression of atoh1a, a key proneural gene required for hair cell commitment. As the neuromast grows, Notch signaling becomes spatially compartmentalized, with lower Notch activity observed in dorsal and ventral compartments, where hair cells predominantly differentiate [78, 189].

4.10 Regeneration of hair cells

The zebrafish lateral line system has a remarkable ability to regenerate hair cells following damage. Unlike many other mechanosensory epithelia (e.g. the mammalian inner ear), zebrafish can rapidly and efficiently replace lost hair cells throughout their lifetime [83]. Following hair cell death, support cells in the neuromast proliferate and differentiate to replace the lost hair cells, and Notch signaling has been shown to play a crucial role in regulating hair cell regeneration. The expression of pathway components is rapidly

upregulated following hair cell damage, including notch3, deltaA, and atoh1a within the first 24 h post-injury [86], coinciding with the period of maximum support cell proliferation and hair cell progenitor formation. Inhibition of Notch signaling during regeneration leads to an overproduction of hair cells, suggesting that Notch indeed acts to limit the number of hair cells [86].

4.11 Fate patterning depends on mechanochemical feedback

Notch signaling depends on the size and geometry of physical contacts between cells [73, 93, 190] and several studies have demonstrated that Notch signaling is sensitive to cellular rearrangements [17]. A combination of space-dependent signaling interactions and Potts model of heterotypic mechanical interactions was used successfully to model the size and cell-type ratio of regenerating neuromasts [191]. These findings raise the question of whether the contact topology, i.e. knowledge about all cell-cell contacts within the organ, and how they dynamically evolve during development, suffices to predict hair cell differentiation.

Together with experimental experts from the Jacobo group (Adrian Jacobo, Akilandeswari Balasubramanian and Tiger Lao, CZ Biohub, San Francisco), I have investigated whether a minimal model of contact-based signaling can predict hair cell differentiation patterns. In particular, I analyzed the location of sensory cell differentiation events, confirming the bias towards dorsal and ventral organ regions reported in literature [78]. Moreover, I computed contact networks from segmented *in vivo* fluorescent microscopy videos of developing zebrafish neuromasts, and I used them to inform simulations of contact-based signaling and to predict the experimentally observed differentiation patterns.

4.12 Hair cells differentiate in the dorsal and ventral compartments

To investigate the spatial organization of hair cell differentiation in the zebrafish neuromast, live imaging was performed on 2-day-old zebrafish embryos by the Jacobo group using Tg(myo6b:actb1-EGFP) zebrafish, in which β-actin-GFP is expressed under the control of the hair cell-specific myo6b promoter. This reporter line enables the selective visualization of differentiating hair cells against a background of supporting cells. Imag-

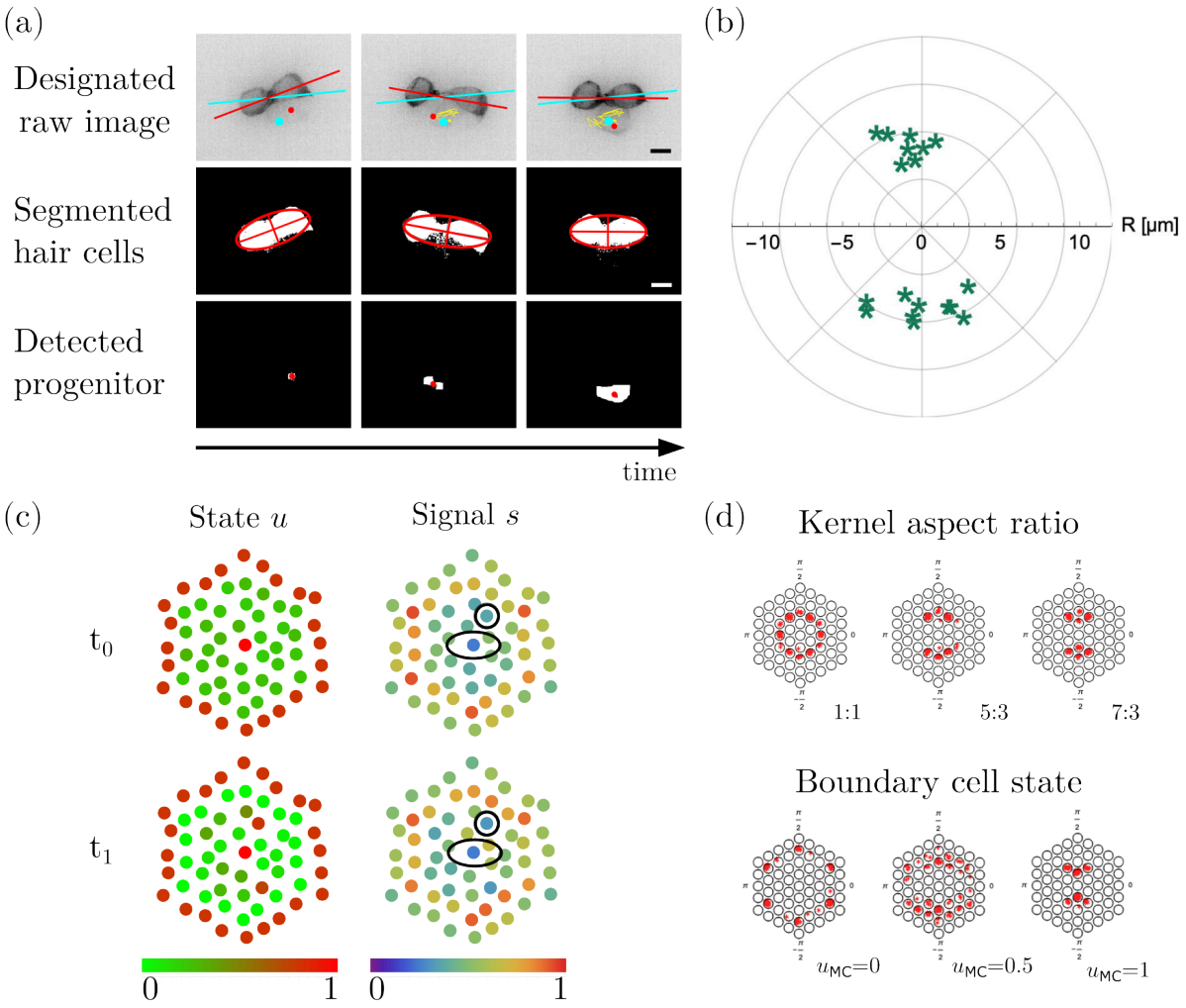

Figure 4.10. Location of sensory cell differentiation. (a) Analysis of live images from developing progenitor hair cells. Middle row depicts segmentation and ellipse fitting of the already established hair cell pair, the bottom row shows the segmentation and tracking (red dot) of the new progenitor cell. Top row summarizes the results for each frame. red line: major axis current frame, blue line: average major axis over all frames, red dot: progenitor cell position current frame, blue dot: average progenitor cell position from several frames (averaging the yellow trajectory). Scale bar: 5 µm. (b) Polar plot summarizing the detection of progenitor cells relative to the anterio-posterior, $N = 18$. (c) Simulation of kernel-based signaling following the neuromast geometry for initial conditions (t_0) and after simulation time (t_1). Left: cell state u, right: received signal s. The central unit has an anisotropic kernel shape, all others units isotropic shapes as indicated on the right. (d) Parameter analysis of the kernel model, each panel summarizes 100 simulations as shown in (c). Red dots mark the position of the first cell reaching a state $u > 0.8$ in a simulation. 1st row: variation of the center kernel aspect ratio. 2nd row: variation of fixed boundary state u_{MC}.

ing was conducted in the apical plane of the neuromast using a super-resolution confocal microscopy system (details, see [68]).

To extract the location of differentiating cells from the microscopy data, I developed a custom macro for ImageJ [192]. Mature hair cell pairs were segmented using intensity thresholding, and their orientation was determined by fitting a second-moment ellipse [Fig. 4.10(a)]. As mature hair cell pairs align along the anteroposterior axis of the neuromast [68], this axis was defined as the average orientation of the mature hair cell pair over up to ten successive frames preceding the emergence of a new hair cell progenitor (imaging performed in 5 min intervals). The appearance of new progenitor cells was identified based on the first detectable expression of the hair cell-specific fluorescent marker in a previously non-fluorescent cell, which was determined using a combination of intensity thresholding and morphological filtering [Fig. 4.10(a)]. Figure 4.10(b) summarizes the spatial distribution of $N = 18$ differentiation events relative to the anteroposterior axis, demonstrating a pronounced localization bias toward the dorsal and ventral compartments of the neuromast. These results confirmed that hair cell differentiation occurs in a compartmentalized manner—in the dorsal and ventral region—in line with previous findings [78, 185].

4.13 Kernel-based simulations recapitulate differentiation patterns

Based on the evidence that compartmentalized differentiation of hair cells in the neuromast depends on Notch lateral inhibition, I explored if the spatiotemporal patterns and the emergent organ axis can be explained on the basis of morphological feedback effects. In particular, I tested the hypothesis that the polarity-dependent oriented division of ligand-expressing progenitor hair cells creates and maintains the bilateral organ symmetry. To address this question, I started to implement simulations of the neuromast based on the discrete kernel model as introduced in Section 4.6 [Fig. 4.10(c-d)]. The geometry is shown in Fig. 4.10(c): I initialized signaling units on a hexagonal grid, adding small random displacements. A single signaling unit in the center of the system was defined with a high u value and anisotropic signaling kernel. It represents a first pair of (premature) hair cells sending inhibitory Notch signals and its kernel anisotropy reflects the orientation of the hair cell pair. Moreover, it has been reported that these cells exhibit outward cytoskeletal protrusions along the anterior-posterior axis [68]. All other cells in the simulation possess the same, isotropic kernel. Mantle cells are not observed to differentiate [78, 186], thus, their state u was assumed constant over time. Units at the

boundary, corresponding to the MC, were defined with a fixed and non-changing state u. After a certain simulation time, new units start to acquire a high u state in the ventral and dorsal compartments, which are interpreted as differentiation events in the neuromast [Fig. 4.10(c)]. The influence of various model parameters was tested systematically. Results from a subset are summarized in Fig. 4.10(d). For each set of parameters, 100 simulations were computed. The red stars in each panel represent the first differentiation event (i.e. the first cell reaching a value $u > 0.8$) in a given simulation run. Changing the aspect ratio of the central signaling kernel transforms the system from isotropic to a dorsal-ventral oriented differentiation as observed in experimental data [Fig. 4.10(d), top row]. Due to the small size of the organ, it is strongly influenced by its boundary conditions. High values of u at the boundary (i.e. strong inhibitory signal) prevent differentiation events at the periphery and forces them in the center region [Fig. 4.10(d), bottom row]. In conclusion, the data and simulations presented here confirm that the kernel model can recover the general symmetry of the neuromast and the biased localization of progenitor cell differentiation.

4.14 Derivation of cell-cell contact networks from live microscopy data

To further test the hypothesis, that the contact-topology of the neuromast governs the differentiation patterns of sensory cells, the next step was to quantitatively analyze the cellular organization and contact dynamics within the epithelium.

For this analysis, the Jacobo group used structured illumination microscopy to acquire high-resolution live imaging data from a zebrafish transgenic line expressing fluorescently labeled claudin-b, a membrane marker that highlights all cell boundaries [Fig. 4.11]. To detect cellular volumes and the contacts between them, I setup an image segmentation pipeline combining the image segmentation softwares PlantSeg [194] and Cellpose [195] to enhance the contrast of cell boundaries (PlantSeg) and subsequently segment the cell volumes (Cellpose) (Appendix K). Tracking of cells was then performed using a custom written ImageJ macro based on the ImageJ plugin TrackMate [196]. Despite additional training of the Cellpose segmentation model, after manually correcting segmentation errors, artifacts like split cell volumes and small segmentation fragments could not be removed completely. Therefore, the segmentations of cellular volumes from which I derived the contact networks used for the simulations presented in this thesis were performed by the Jacobo group using an alternative neural network-assisted pipeline [197], followed by manual refinement to correct errors and ensure high-quality cell volume de-

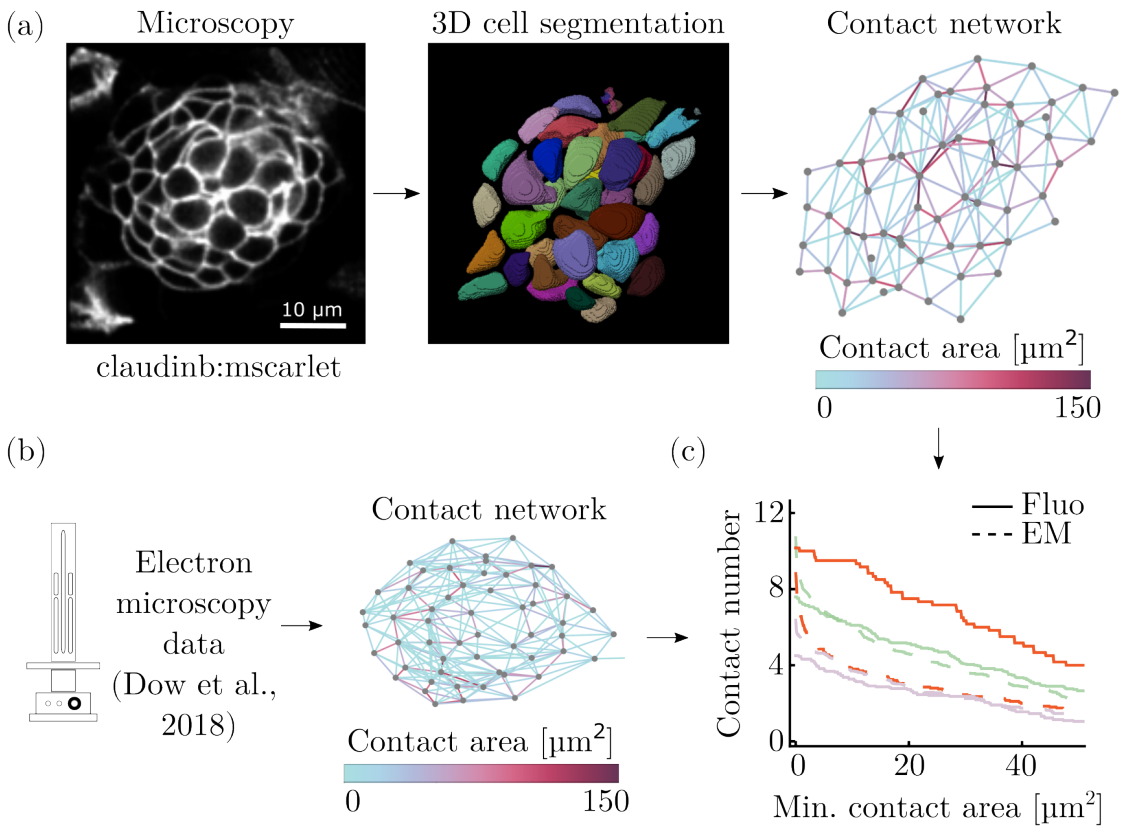

Figure 4.11. (a) Cell-cell contact-networks were derived from segmentations of 3D fluorescent microscopy images. The vertices denote cell centroids and the color code of the connections indicates the size of mutual contacts. (b) Contact-networks were derived from segmented EM datasets of zebrafish neuromasts [193]. (c) Average number of cell-cell contacts found for supporting cells (green), mantle cells (purple), and hair cells (orange) in EM ($N = 3$) and fluorescent microscopy datasets ($N = 3$) as a function of minimum cut-off area (smallest area still counted as a contact). For mantle and support cells, more small contacts ($< 5\,\mu m$) are found in the EM datasets.

tection. Moreover, based on the cellular morphology [198], the three cell types—support cells, hair cells, and mantle cells—were manually annotated by members of the Jacobo group. [Fig. 4.9(c)]. Maturing hair cells are distinct by acquiring a spherical shape and by forming an apical hair bundle structure, which is clearly visible in the microscope. The segmented datasets exhibited gaps between adjacent cells. To address these gaps, I dilated the segmented cell volumes in order to bring them into direct contact and to enable the measurement of contact areas between the cells [Appendix K]. Following volume dilation, a custom Python script was used to compute the contact areas between cells by computation of the 6-neighborhood of each voxel (i.e., the six nearest neighbor voxels). All contact areas between adjacent volumes were stored in a symmetric matrix $c_{i,j}$, where

entry (i, j) represented the total measured contact area between cell i and cell j, taking into account the non-isotropic voxel dimensions. While highly irregular surfaces (e.g. due to segmentation errors) could, in principle, lead to (artificially) increased contact areas, the initial segmentation volumes were already smooth [Figs. 4.9(c), 4.11(a)], and the applied isotropic expansion further contributed to smoothing.

I applied the same pipeline to segmented electron microscopy (EM) data, published in [193], to derive cell-cell contact networks of higher resolution. While fluorescent microscopy is typically limited to a resolution of ∼200 nm in the xy-plane and ∼1–2 µm along the imaging axis due to the diffraction limit, electron microscopy can resolve structures down to the atomic scale [199, 200], however, it does not allow for live imaging.

4.15 Statistics of cell-cell contacts

Figure. 4.11(c) compares the average number of contacts found for support, mantle, and hair cells in fluorescence and electron microscopy data. Mantle cells have the lowest contact number, because they form the outer most layer of the organ. From the fluorescent microscopy data ∼ 8 contacts were found per supporting cell, with ∼ 6 contacts $\geq 10\,\mu m^2$. For mantle and support cells, the numbers of large contacts are comparable between fluorescent and EM data, however, $\sim 3-4$ additional small contacts $\leq 5\,\mu m^2$ were found in the EM data, indicating that cell-cell contacts at small protrusions could be missing in the diffraction-limited fluorescence data. The additional hair cell contacts include

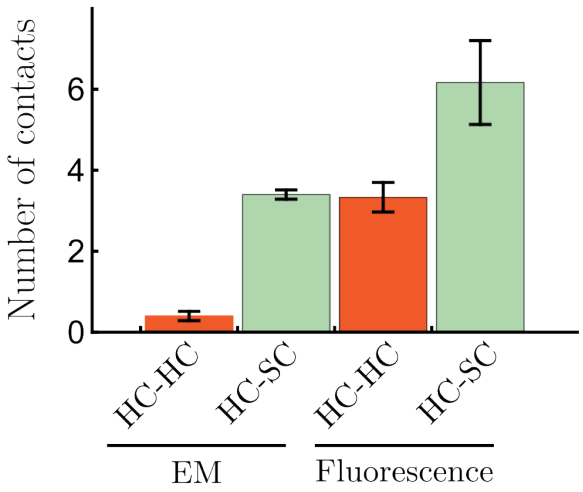

Figure 4.12. Number of hair cell - hair cell (HC-HC) and hair cell - supporting cell (HC-SC) contacts > 1 µm computed from three EM and three fluorescence microscopy datasets. More contacts were found in the fluorescence data.

HC-HC as well as HC-SC contacts [Fig. 4.12]. As no information is available about the subcellular location of receptor and ligand molecules, it generally cannot be said for sure which cell-cell contacts contribute to signaling.
After division of a progenitor hair cell, daughter cells move apart and are separated by intercalation of supporting cell protrusions [68], thus, the nearly vanishing number of HC-HC contacts found in EM datasets is indeed expected. When analyzing simulations of contact-based signaling on data-derived contact network, it is important to keep in mind that the fluorescence microscopy data might miss contacts. As mature hair cells experienced an irreversible fate decision, I assume in the following sections that their signaling state is independent of their received signals, thus, results are independent of HC-HC contacts. HC-SC contacts, however, that are missing in the contact networks could affect the analysis outcome.

4.16 Modeling contact-based signaling on contact-networks

To simulate contact-dependent Notch signaling, I use the dynamic equation

$$\frac{du_i}{dt} = \frac{1}{1+s_i^h} - u_i \tag{4.26}$$

with Hill coefficient h, similar to the framework introduced in Chapter 2 [Eq. (2.72)], where each cell is represented by a single signaling state variable u_i changing due to the received signal s_i. Because each cell has multiple contacts, the total signal received by a cell i is computed by summing over all cells in the system

$$s_i = \chi \sum_j c_{ij} u_j + \xi(t) \tag{4.27}$$

with c_{ij} the data-derived contact network multiplied by the state-dependent potential to send inhibitory signals, χ is the signal susceptibility, and ξ a Gaussian noise term with $\langle \xi(t), \xi(t') \rangle = \eta^2 \delta(t-t')$ and noise amplitude η. Note that this definition of the signal differs from Eq. (2.72) (Chapter 2) in the sign of u, however, the Hill function Eq. (4.26) is also flipped compared to Eq. 2.73, thus, the logic of the symmetry-breaking mutually inhibitory feedback is conserved. The mantle cells are not observed to differentiate, thus, their state u is assumed constant over time. Single cell RNA expression studies suggest that mantle cells express the Notch ligands jagged2a and jagged2b [201]. Delta-Notch signaling is typically associated with lateral inhibition mosaic patterning, because the expression of the Delta ligand is decreased by Notch receptor activation. In contrast, Notch signals typically stimulate the expression of ligands from the Jagged family, leading

to a positive feedback [159]. Considering that I fix the state of the mantle cells and only consider their role as signal sending cells for fate patterning, it does not matter if the signal is transmitted through Delta or Jagged ligands, and I can represent the mantle cell state with the same signaling state variable u. Similarly, the state u_{HC} of sensory hair cells is fixed as they already differentiated. Whenever a support cell is observed to divide into a pair of hair cells, then the states of both of these cells are set and fixed to the hair cell state for the remaining simulation. Simulations are performed with $c_{ij}(t)$ informed from the dynamically evolving contact networks derived from the data (images taken in 5 min intervals).

To this end, I screen parameters of the model to identify regimes in which unique differentiation events are predicted, in particular adjusting the signal susceptibility χ, the signaling time scale τ_u, the Hill coefficient h in the signal response function [Eq. (2.73)] and the noise amplitude. Hill coefficients of 2-4 are commonly used in models of biochemical signaling feedback, including Notch [67, 107, 108, 159, 191]. In the following, I thus use a Hill coefficient of $h = 4$ unless otherwise stated. Using larger Hill coefficients does not impact the results, while smaller Hill coefficients (i.e. $2 \leq h \leq 4$) alter the number of predicted differentiation events unless the susceptibility χ is adjusted. The signal susceptibility χ is empirically adjusted to create sufficient signal s in the model for effective lateral inhibition ($\chi \in \mathcal{O}(10^1)$ after normalizing c_{ij} against the largest contact). The signaling time scale τ_{u} was varied from less than a minute to 1 hour and more [Fig. 4.14(a)]. Longer time scales act as a low pass filter against fluctuations of the contact network topology. Good predictions of differentiation patterns where achieved for $\tau_{\mathrm{u}} \geq 15$ min. Considering the underlying biological processes changing the regulation of genes, time scales of tenth of minutes are indeed expected [114].

4.17 Signaling simulations on contact networks can predict cell differentiation patterns

Interestingly, simulations on the data-derived networks allow to predict regions of sensory cell differentiation. Events of progenitor cells dividing into pairs of hair cells correlated with neighboring supporting cells reaching a high u state within the same dorsal or ventral region [Fig. 4.13]. Periods in which high u-state support cells appear, spaced around 500–1000 min apart, are separated by longer periods without support cells reaching a high u state [Fig. 4.13(b)]. Deterministic simulations without noise ($\eta = 0$) quickly converge for almost arbitrary initial support cell states $u \in [0, 1]$, indicating that the contact network-topology in combination with the imposed hair cell and mantle cell states

strongly constrains the system.

The observation that the actual progenitor cell which divides into a hair cell pair is in contact with a high u-state cell while maintaining a low u value itself is surprising. Progenitor cells and maturing hair cells are found to increase the expression of the Delta ligand, thus, I expected that progenitor cells undergoing divisions would reach the signal sending high u states. In contrast, all six progenitor cell divisions observed in two different neuromast organs correlate with low u-values in the progenitor cell and a high u-value in one or two neighboring cells preceding the division [Fig. 4.13]. It is important to note, however, that neuromast cells express different types of notch receptor and ligand molecules [186], thus, it is possible that a more detailed model with multiple variables and parameters, and including combinations of positive (Jagged ligand) and negative feedbacks (Delta ligand) could resolve this conundrum.

The mutually inhibitory feedback of Notch signaling is thought to amplify small initial differences between interacting cells, such that the cell with highest initial ligand concentration further increases the amount of ligands, while the ligand production in contacting cells is diminished [143]. This means signaling can amplify small noise-induced differences [202], and it raises the question whether cell fate decisions cannot be predicted with single cell precision based on the contact topology alone, because signaling amplifies small random fluctuations, for instance, of intracellular molecule concentrations. To test this, I performed simulations with varying noise amplitude [Fig. 4.14(b)]. Interestingly, even for noise amplitudes up to $\eta = 0.5\,\mathrm{min}^{-1/2}$, the true progenitor cells are not predicted to reach a signal sending high u state. This is independent of whether contact networks are weighted according to the contact area or binarized (i.e. $c_{ij} = 1$ for every cell pair i and j that shares a contact, otherwise $c_{ij} = 0$).

In conclusion, the simulation results suggest that the contact-topology contains sufficient information to predict time windows and regions in which support cells differentiate into sensory hair cells. It indicates that through the local interactions, cells are able to identify their own position relative to global organ coordinates. Moreover, it suggests that the local interactions allow these proliferative organs to sense the cell density and to initiate differentiation events at time intervals that maintain a functional ratio between hair and support cells. In the future, it will be exciting to study if the predicted differentiation patterns are consistent for a larger amount of data sets. Moreover, studying perturbations like laser ablation and optogenetic manipulation of hair and mantle cells would allow to interrogate the fixed signaling states that I assumed in the simulations.

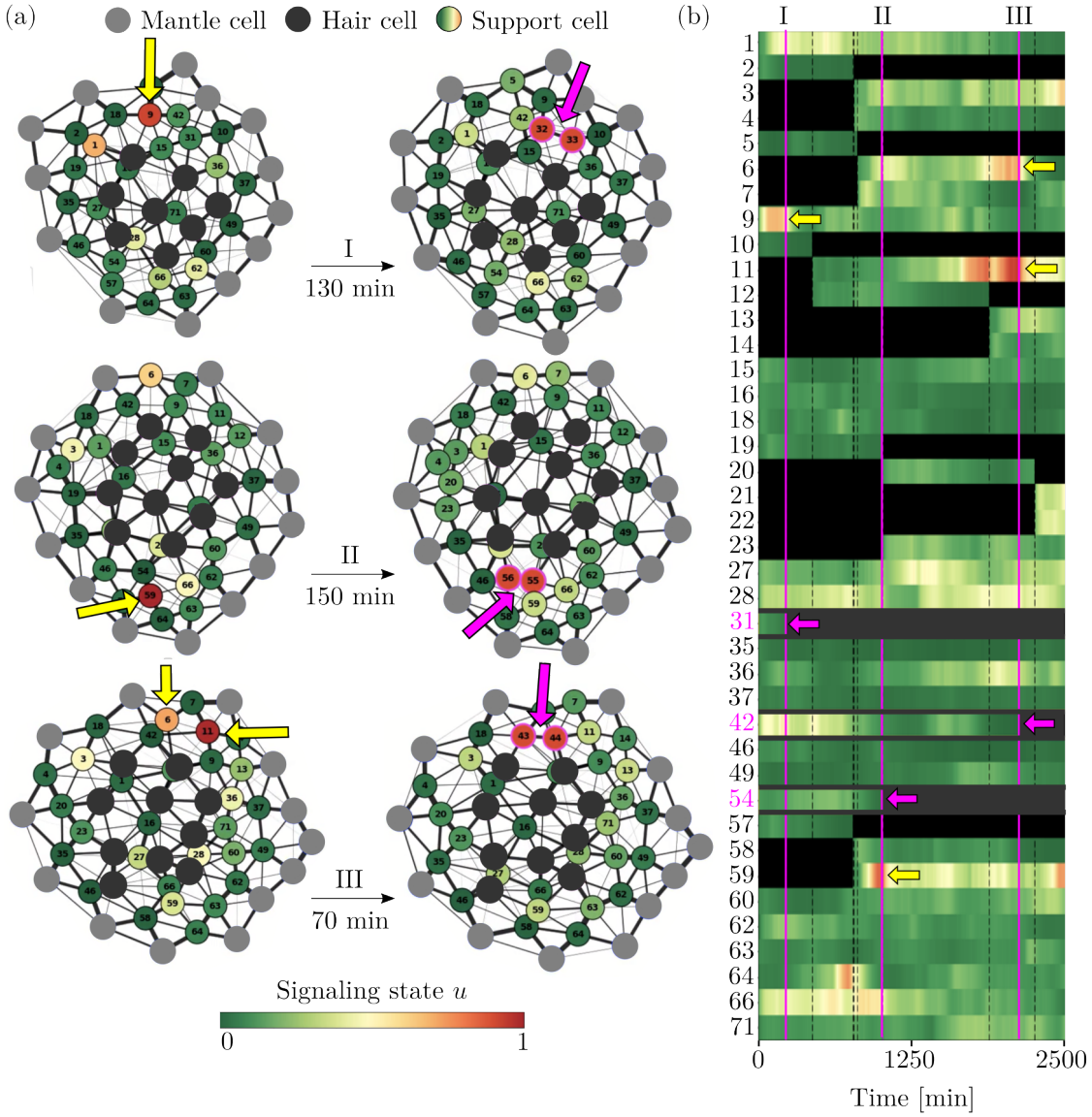

Figure 4.13. Contact-dependent signaling simulations predict regions of differentiation. (a) Three snap shots of data-derived contact networks before (left) and after (right) the division of a progenitor cell into a hair cell pair (magenta arrows). Prior to each division, a neighboring support cell reached a high u signal sending state (yellow arrow) within the same dorsal or ventral pocket. Vertices are cell centroids, edge thickness proportional to contact sizes (b) State diagram of support cell signaling states averaged over 20 simulations with varying initial conditions $u_{\mathrm{SC}} \in [0, 0.5]$. Each row corresponds to one cell label. Magenta vertical lines: progenitor division I-III as shown in (a)), black dashed line: support cell division, yellow arrows indicate support cells with high u states that were in contact with a subsequently dividing progenitor cell (magenta arrows). States of cells are black before they are born and after they disappear through division. $\chi = 1, h = 4, \tau_{\mathrm{u}} = 30\,\mathrm{min}$, $\eta = 0$, c_{ij} was normalized against the largest contact found in the data set ($158.6\,\mu\mathrm{m}^{-2}$).

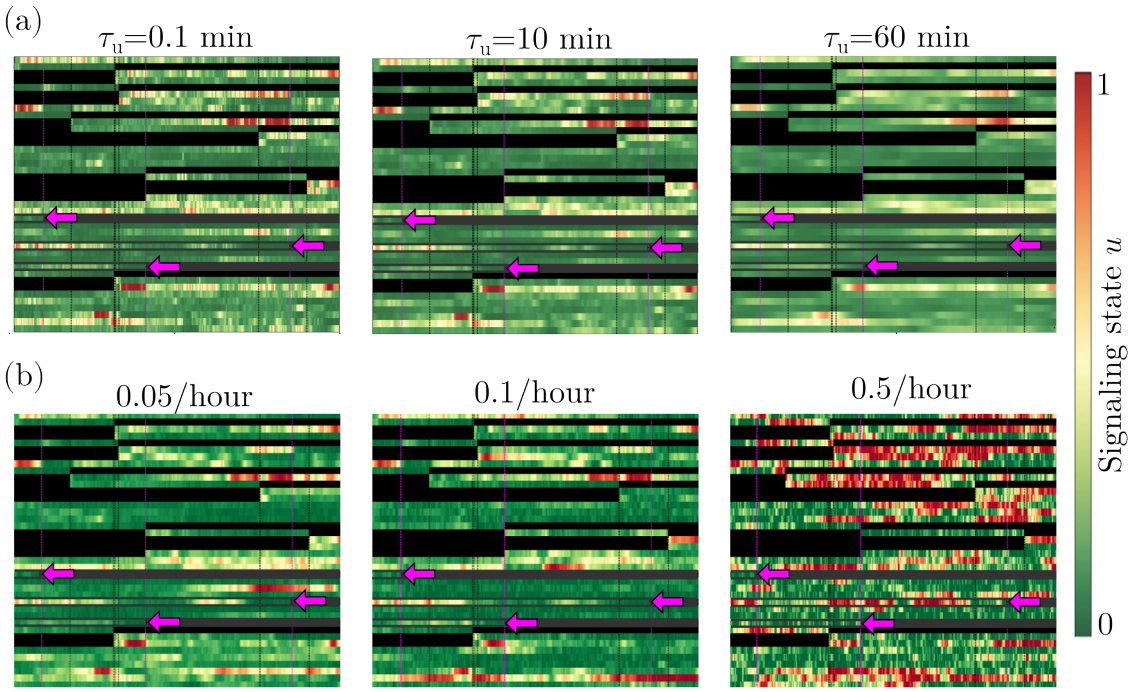

Figure 4.14. (a) Simulated support cell states averaged over 20 simulations, under variation of the signaling time scale τ_u. Long signaling time scales act as a low pass filter against fluctuations of the contact topology. (b) To provide intuition, the noise amplitude is expressed in terms of standard deviation of signaling states after one hour, if state changes were purely noise driven without signaling. Even for strong noise, progenitor cells show low signaling states u prior to their division into hair cell pairs (magenta arrows). Parameters and total simulation time (2500 min) as in Fig.4.13.

Chapter 5

Summary and Outlook

Investigating the physics of capillarity has established how surface tension and curvature control liquid interfaces, providing a formal understanding of diverse phenomena, including droplet dynamics, thin films, and flows in porous media. In non-equilibrium systems moreover, interfaces undergo dynamic, adaptive changes. When shape changes are driven by environmental cues, materials can exhibit functional, responsive behavior. These effects are especially common in living matter: cells for example continuously adapt their morphology in response to mechanical and biochemical signals, which themselves depend on cell shape. Motivated by this phenomenon, my thesis investigated the new physics that arises in systems of interacting droplets that tune their interfacial tensions in response to contact-dependent signals–from microscopic scales to single droplets and foams.

Deriving and analyzing the microscopic dynamics of contact-dependent signaling and adhesion molecules (Chapter 2), I identified several limits in which analytical expressions for the surface and bulk densities of these particles can be obtained. I showed how the molecular turnover—considering specific reactions and kinetics as reported for contact-dependent Notch signaling—leads to non-uniform spatial distributions, resulting in non-linear relations between contact size and transmitted signal. Furthermore, my results reveal how the geometrical and physical constraints, such as system size and transport coefficients, modulate the field dynamics of adhesion and signaling molecules on different interfacial configurations.

From these microscopic dynamics, I derived coarse-grained equations that represent adaptive droplets, which adjust their interfacial tension in response to contact-dependent signals. Using the separation of timescales in systems driven by molecular turnover, I simplified expressions to two key parameters: an adaptive adhesion coefficient, which describes how signaling modulates interfacial tension, and the signal susceptibility, which governs how physical contacts regulate signal levels. This minimal framework enabled a comprehensive analysis of the system's nonlinear dynamics and critical points (Chapter

3), revealing a rich phenomenology, including multistability, oscillations, and excitability. Notably, by comparison of the underlying bifurcation topology, I found that shape changes can act analogously to electrical signals in neurons, suggesting a broader role for mechanochemical computation in biological systems.

Extending the framework to multicellular, foam-like structures enabled the application of my theoretical results to experimental data. In particular, using imaging data from zebrafish embryos in collaboration with developmental biologists (Petridou group, EMBL), I inferred the two mechanochemical feedback parameters from cellular contact-angle measurements in this system. Our results revealed that the system operates near the critical point associated with shape bistability, leading to the emergence of a sharp boundary between tissue regions with distinct rheological properties, which later give rise to different parts of the organism. These results show how shape-dependent feedback can convert a chemical signal gradient into spatially organized mechanical states—an example of signal processing in active matter.

Moreover, using fully data-derived contact topologies, obtained in collaboration with the Jacobo group (CZ Biohub, San Francisco), I successfully predicted cell fate decision events in time and space in developing zebrafish mechanosensory epithelia. Our results highlight how cell-cell contact topology can encode spatial information, enabling individual cells to infer their relative position through local interactions, and they contribute to our understanding of tissue self-organisation in developing and regenerating organs.

Some of the nonlinear behaviors observed at the droplet scale could give rise to additional collective regimes, such as traveling waves or synchronized oscillations. Such phenomena have been observed in various biological and synthetic systems. For instance, intracellular signaling networks exhibit oscillatory and wave-like patterns [203], while collective oscillations and waves emerge in bacterial suspensions due to motility [204]. Theoretical studies suggest that excitable mechanical feedback can drive similar behaviors in vertex-based models of tissues [205] and in pulsatory wave models driven by diffusing molecules [206]. In soft matter physics, active solids can generate wave-like responses through selective activation of elastic modes [207], providing an example for how active force generation and adaptive material properties can produce dynamic patterns. The precise nature of these wave-like behaviors depends on how activity is introduced into the system. While active tension fluctuations, self-propulsion, or volume regulation have been considered as specific non-equilibrium terms in vertex models, my work focuses on an alternative mechanism, in which internal production and degradation processes drive the system out of equilibrium. A possible experimental platform for observing the predicted collective dynamics is provided by engineered synthetic systems that mimic contact-dependent signaling [121]. A promising approach involves switchable adhesion substrates, where droplets or cells

adhere dynamically in response to external stimuli, allowing for the implementation of feedback-controlled adhesion [38]. Similarly, optogenetic tools could be used to control cell adhesion, while signaling is simulated in silico [90], providing a quantitative testbed for the interplay of shape and signal processing. Another direction is to leverage genetic engineering [52], to express adhesion molecules downstream of contact-dependent signaling. In particular in combination with tools that allow to control the system's geometry like micropatterned substrates [208] or micropipette aspiration could provide ways to directly test additional predictions of the theory of mechanochemical matter developed in this thesis.

In cells, the production of functional proteins is controlled through transcriptional and translational regulation, relying on relatively slow cellular processes that evolve on a timescale from 10 min to 1 h and longer [114, 209]), defining the time scale for the large-scale dynamics of living matter, including development, regeneration and homeostasis [68, 81, 146, 210]. While my analyses focus on the corresponding parameter regime, in which regulatory timescales are much larger than the frictional timescale determining the response dynamics of surface shape changes, other biochemical processes, including the local phosphorylation of compounds, or the (dis)assembly of macromolecular, cytoskeletal filaments can be much faster, and could give rise to novel mechanochemical feedback phenomena. The frictional time scale of cell shape relaxations depends on the strength and duration of the deforming stresses, because most living materials are viscoelastic: while forces applied for a few seconds trigger an elastic response, force applied over longer times usually induce the rearrangement of cytoskeletal structures, thus, inducing irreversible shape changes. In cases, where signaling and frictional timescales are comparable, shape can serve as a form of mechanical memory, encoding past states of the system.

In conclusion, by developing a theory of mechanochemical dynamics from microscopic to macroscopic scales, this work reveals novel modes of collective self-organisation in adaptive materials. I demonstrated the relevance of these principles for the biology of developing and regenerating living systems by investigating specific instances of mechanochemical self-organisation in collaboration with experimental experts. Together, our findings contribute to a broader understanding of how biological systems compute, self-organize, and adapt to changing environments. Moreover, this work opens up future lines of investigation at the interface of physics, material science, and biology. In particular, my findings could inform and motivate the implementation of mechanochemical principles in synthetic systems, towards translating insights from the physics of living matter into new applications in bio-inspired materials design.

Appendix

A - Numerical surface energy minimization

To numerically verify Eq. (1.7), I used the finite-element based software *surface evolver* to minimize surface energy [Eq. (1.3)] by the gradient descent method [29]. Initialization and procedural-control scripts were implemented in Mathematica [211]. To numerically verify Eq. (1.7), I computed the minimal energy configurations for a pair of droplets ($n = 1$), a line of 7 droplets ($n = 2$), a 5×5 lattice ($n = 4$) and a $5 \times 5 \times 5$ droplet lattice ($n = 6$) and measured the contact area of the central droplet. Bash scripts to rerun this analysis are published at [105].

B - Geometrical relations for spherical caps

The energy of an adherent Young-Laplace droplet in contact with a solid surface is

$$H = (\gamma_\mathrm{c} - \gamma_\mathrm{m})A_\mathrm{c} + \gamma_\mathrm{f} A_\mathrm{f} - pV \tag{5.1}$$

with volume, areas, surface tensions and pressure as introduced in Section 1.1 [Fig. 1.1(b)]. Minimizing the energy leads to the equilibrium shape of a spherical cap with a base radius r_max and a height z. The surface areas and the volume are

$$A_\mathrm{f} = \pi \left(r_\mathrm{max}^2 + z^2\right), \quad A_\mathrm{c} = \pi r_\mathrm{max}^2, \quad V = \frac{\pi}{6} h (3 r_\mathrm{max}^2 + z^2). \tag{5.2}$$

The equilibrium shape is determined by the conditions

$$\frac{\partial H(r_\mathrm{max}, z)}{\partial r_\mathrm{max}} = 0, \qquad \frac{\partial H(r_\mathrm{max}, z)}{\partial z} = 0, \qquad V(r_\mathrm{max}, z) = const \tag{5.3}$$

assuming conserved volume. From Eq. (5.2) one can derive a depressed cubic equation

$$z^3 + 3 r_\mathrm{max}^2 h - \frac{6}{\pi} V = 0, \tag{5.4}$$

with a discriminant that is strictly negative for $r_\mathrm{max} > 0$ and $V > 0$ and yields an expression $z = z(r_\mathrm{max}|V)$ [Eq. (2.22)]. The equilibrium shape is therefore determined by

a single equation

$$\frac{\partial}{\partial r_{\max}} H[r_{\max}, z(r_{\max})] = 0. \tag{5.5}$$

From Pythagoras

$$\rho^2 = r_{\max}^2 + (z - \rho)^2 \tag{5.6}$$

follows Eq. (2.21).

C - Signaling without cleavage

Similar to Section 2.2.1, consider a single cell in contact with a solid substrate that is functionalized with immobile ligands at a fixed uniform density $m_{\mathrm{L}}^{\max}$. The cell contains receptor molecules with bulk concentration c_{R}, with dynamics coupled to the ligand density via binding and unbinding reactions at the contact surface. In contrast to Section 2.2.1, assume that receptor-ligand complexes are not cleaved ($k_{\mathrm{s}} = 0$) and signals are transmitted to the interior without the loss of receptor molecules, e.g. through enzymatic activity of the receptor-ligand complex [48, Chapter 15]. In that case, the reaction terms are [Eq. (2.2)]

$$\mathcal{R}_{m_{\mathrm{R}}} = k_{\mathrm{on}}^{\mathrm{R}} c_{\mathrm{R}} - (k_{\mathrm{off}}^{\mathrm{R}} + k_+ m_{\mathrm{L}}) m_{\mathrm{R}} + k_- m_{\mathrm{RL}}, \tag{5.7}$$

$$\mathcal{R}_{m_{\mathrm{L}}} = k_- m_{\mathrm{RL}} - k_+ m_{\mathrm{L}} m_{\mathrm{R}}, \tag{5.8}$$

$$\mathcal{R}_{m_{\mathrm{RL}}} = k_+ m_{\mathrm{L}} m_{\mathrm{R}} - k_- m_{\mathrm{RL}}, \tag{5.9}$$

with densities and rates as defined in Section 2.2.1. The steady state relations of Eq. (2.2) then fulfill

$$m_{\mathrm{RL}} = \frac{m_{\mathrm{R}}}{\frac{k_{\mathrm{s}}}{k_+} + m_{\mathrm{R}}} m_{\mathrm{L}}^{\max} \tag{5.10}$$

$$0 = \frac{D_{m_{\mathrm{R}}}}{r} \frac{\partial}{\partial r} \left(r \frac{\partial m_{\mathrm{R}}}{\partial r} \right) + k_{\mathrm{on}}^{\mathrm{R}} c_{\mathrm{R}}^0 - k_{\mathrm{off}}^{\mathrm{R}} m_{\mathrm{R}} \tag{5.11}$$

where the latter is identical to Eq. (2.26)

D - Integration constants for receptor surface densities

In Section 2.2.1, I study the steady state receptor distribution in the limit of small $(k_{\mathrm{s}} + k_-)/(k_+ m_{\mathrm{R}^0})$ [Eq. (2.29)], leading to the steady state solutions Eq. (2.18), (2.31) at

the free and contact surface, respectively. Solving for the integration constants using the boundary conditions Eq. (2.23), (2.24)yields

$$\begin{aligned}\mathcal{C}_1 &= \frac{\rho k_\mathrm{s} m_\mathrm{L}^{\max} I_1\left(\frac{r_{\max}}{l_{\mathrm{D,f}}}\right)\sin\vartheta_{\max}}{k_\mathrm{on}^\mathrm{R} c_\mathrm{R}^0\left[l_{\mathrm{D,f}}(\lambda+1)I_0\left(\frac{r_{\max}}{l_{\mathrm{D,f}}}\right)\mu_1-\rho I_1\left(\frac{r_{\max}}{l_{\mathrm{D,f}}}\right)P_\lambda\left(\cos\theta_{\max}\right)\sin\vartheta_{\max}\right]}\\ \mathcal{C}_3 &= \frac{k_\mathrm{s} m_\mathrm{L}^{\max} l_{\mathrm{D,f}}(\lambda+1)\mu_1}{k_\mathrm{on}^\mathrm{R} c_\mathrm{R}^0\left[l_{\mathrm{D,f}}(\lambda+1)I_0\left(\frac{r_{\max}}{l_{\mathrm{D,f}}}\right)\mu_1-\rho I_1\left(\frac{r_{\max}}{l_{\mathrm{D,f}}}\right)P_\lambda\left(\cos\theta_{\max}\right)\sin\vartheta_{\max}\right]}\end{aligned} \tag{5.12}$$

where I shortened the notation using

$$\mu_1 = [\cos\theta_{\max} P_\lambda(\cos\vartheta_{\max}) - P_{\lambda+1}(\cos\vartheta_{\max})] \tag{5.13}$$

and where the angle $\theta_{\max}$ is related to the contact radius via $r_{\max} = \rho\sin\theta_{\max}$.

In Section 2.2.1, I study the steady state receptor distribution in the limit of fast cleavage rate k_s, leading to the steady state solutions Eq. (2.18), (2.34) at the free and contact surface, respectively. Solving for the integration constants using the boundary conditions Eqs. (2.23), (2.24) yields

$$\begin{aligned}\mathcal{C}_1 &= \frac{\rho\mu_2 I_1\left(\frac{r_{\max}\sqrt{1+\mu_2}}{l_{\mathrm{D,f}}}\right)\sin\vartheta_{\max}}{l_{\mathrm{D,f}}(1+\lambda)\sqrt{1+\mu_2}I_0\left(\frac{r_{\max}\sqrt{1+\mu_2}}{l_{\mathrm{D,f}}}\right)\mu_1-\rho(1+\mu_2)\mu_3\sin\theta_{\max}}\\ \mathcal{C}_4 &= \frac{l_{\mathrm{D,f}}(1+\lambda)\mu_2}{l_{\mathrm{D,f}}(1+\lambda)\sqrt{1+\mu_2}I_0\left(\frac{r_{\max}\sqrt{1+\mu_2}}{l_{\mathrm{D,f}}}\right)\mu_1-\rho(1+\mu_2)\mu_3\sin\theta_{\max}}\end{aligned} \tag{5.14}$$

with μ_1 as defined above[Eq. (5.13)],

$$\mu_2 = \frac{k_+ k_\mathrm{s} m_\mathrm{L}^{\max}}{(k_\mathrm{s}+k_-)k_\mathrm{off}^\mathrm{R}} \tag{5.15}$$

and

$$\mu_3 = I_1\left(\frac{r_{\max}\sqrt{1+\mu_2}}{l_{\mathrm{D,f}}}\right)P_\lambda(\cos\theta_{\max}). \tag{5.16}$$

to shorten the notation.

E - Steady state receptor surface densities for fixed boundary flux

In Section 2.2.2, I analyze the normalized steady state surface receptor densities for fixed boundary conditions, e.g. due to active processes at the contact line. For a fixed boundary

flux $j_{\mathrm{R}}|_{\partial\Gamma_{\mathrm{c}}} = -D_{m_{\mathrm{R}}}\frac{\partial m_{\mathrm{R}}}{\partial r}$, the steady state solutions are:
Limit 1 [Eq. (2.25)]

$$M_{\mathrm{R}} = 1 - \frac{j_{\mathrm{R}}|_{\partial\Gamma_{\mathrm{c}}}\, l_{\mathrm{D,f}}}{D_{m_{\mathrm{R}}}} \frac{I_0\left(r/l_{\mathrm{D,f}}\right)}{I_1\left(r_{\max}/l_{\mathrm{D,f}}\right)}, \tag{5.17}$$

Limit 2 [Eq. (2.55)]

$$M_{\mathrm{R}} = \left(1 - \frac{k_{\mathrm{s}} m_{\mathrm{L}}^{\max}}{k_{\mathrm{on}}^{\mathrm{R}} c_{\mathrm{R}}^{0}}\right) - \frac{j_{\mathrm{R}}|_{\partial\Gamma_{\mathrm{c}}}\, l_{\mathrm{D,f}}}{D_{m_{\mathrm{R}}}} \frac{I_0\left(r/l_{\mathrm{D,f}}\right)}{I_1\left(r_{\max}/l_{\mathrm{D,f}}\right)}, \tag{5.18}$$

Limit 3 [Eq. (2.32)]

$$M_{\mathrm{R}} = \frac{1}{1 + \dfrac{k_{+} k_{\mathrm{s}} m_{\mathrm{L}}^{\max}}{(k_{\mathrm{s}} + k_{-}) k_{\mathrm{off}}^{\mathrm{R}}}} - \frac{j_{\mathrm{R}}|_{\partial\Gamma_{\mathrm{c}}}\, l_{\mathrm{D,f}}}{D_{m_{\mathrm{R}}} \sqrt{1 + \dfrac{k_{+} k_{\mathrm{s}} m_{\mathrm{L}}^{\max}}{(k_{\mathrm{s}} + k_{-}) k_{\mathrm{off}}^{\mathrm{R}}}}} \frac{I_0\left(r/l_{\mathrm{D,c}}\right)}{I_1\left(r_{\max}/l_{\mathrm{D,c}}\right)}. \tag{5.19}$$

F - Statistical physics of adhesion molecule binding

At steady state, the flux coupling bulk and surface concentrations [Eq. (2.3)] vanishes and the surface can be considered to be in chemical and thermal equilibrium with a constant temperature T and in contact with a bath of constant chemical potential $\mu = \mu(c_{\mathrm{N}})$ set by the steady state bulk concentration. Note that the chemical potential is kept constant through a non-equilibrium process—the turnover of adhesion molecules. Each binding site at the interface is a two-state system: a binding site is either occupied or unoccupied. If n is the number of occupied binding sites, $n^{\max}$ the total number of available binding sites at the surface and ϵ the binding energy, then the grand canonical partition sum for the whole surface reads

$$\Xi = \sum_{n=0}^{n^{\max}} \binom{n^{\max}}{n} e^{\beta n(\mu-\epsilon)} = \left(1 + e^{\beta(\mu-\epsilon)}\right)^{n^{\max}} \tag{5.20}$$

with $\beta = (k_{\mathrm{B}}T)^{-1}$. The ensemble average of the number of occupied binding sites is

$$\langle n \rangle = \frac{1}{\beta}\frac{\partial \ln \Xi}{\partial \mu} = \frac{n^{\max}}{1 + e^{\beta(\epsilon-\mu)}}, \tag{5.21}$$

showing that the system follows Fermi-Dirac statistics. In the chemical equilibrium, the rates of binding and unbinding must be equal for each binding site. The binding rate of adhesion molecules is

$$k_{\mathrm{binding}} = k_{\mathrm{on}}^{\mathrm{N}} c_{\mathrm{N}} p_{\mathrm{uoc}} \tag{5.22}$$

with $p_{\mathrm{uoc}} = 1/(1 + e^{\beta(\mu-\epsilon)})$ the probability that a binding site is not occupied, while the unbinding rate is

$$k_{\mathrm{unbinding}} = k_{\mathrm{off}}^{\mathrm{N}} p_{\mathrm{oc}} \tag{5.23}$$

with $p_{\mathrm{oc}} = e^{\beta(\mu-\epsilon)}/(1+e^{\beta(\mu-\epsilon)})$ the probability that a binding site is occupied. From $k_{\mathrm{binding}} = k_{\mathrm{unbinding}}$ and Eqs. (5.22)–(5.23) follows

$$\frac{k_{\mathrm{off}}^{\mathrm{N}}}{k_{\mathrm{on}}^{\mathrm{N}} c_{\mathrm{N}}} = e^{\beta(\epsilon-\mu)}. \tag{5.24}$$

From $m_{\mathrm{N}} = \langle n \rangle / A_{\mathrm{c}}$ and $m_{\mathrm{N}}^{\max} = n^{\max}/A_{\mathrm{c}}$ together with Eq. (5.21) and $c_{\mathrm{N}} = k_{\mathrm{p}}^{\mathrm{N}}/k_{\mathrm{d}}^{\mathrm{N}}$ follows then Eq. (2.64).

G - Numerical Continuation

The state and bifurcation diagrams presented in Chapters 3 were computed via continuation with the MATLAB-based software package MatCont (MatCont7p4 [212] and MATLAB R2021a [213], custom-written scripts with details and numerical settings are published with [17, 105] and are available at https://git.embl.de/dullwebe/dullweber2024). In general, fixpoints to initialize the continuation were computed by integration over time using the Integrator Method ode45. Results of the continuation were confirmed using simulations and analysis in Mathematica 13.0 [211] (notebooks with a step-by-step explanation of the analysis are published with [105, 106] and are available at https://git.embl.de/dullwebe/dullw
Specifically, I tested the number and types of stable attractors in different parameter regimes with simulations using NDSolve and ParametricNDSolve with the equation simplification method *Residuals*. Fixpoints shown in the phase plots Figs. 3.3, 3.7, 3.9 were computed numerically in Mathematica from the intersections of nullclines. Oscillation amplitudes and periods [Figs. 3.3, 3.4, 3.9, 3.10] were computed from the extrema of simulated trajectories, and checked against the dominant Fourier components.

H - Symmetry-breaking of states is promoted by adaptive adhesion

In many biological systems, Notch signals are mutually inhibitory, i.e. signals suppress the production of ligands [143]. Strong mutual inhibitory interactions generically lead to spontaneous symmetry-breaking [155], whereby small initial differences in the signaling states are amplified and diverge to high- and low-value steady states. At the onset of symmetry-breaking, the uniform steady-state solution of Eq. (2.72) becomes unstable. To derive an approximation for the onset of symmetry-breaking, I expand $\sigma(s_i)$ [Eq. (2.73)] for a general Hill coefficient h to first order around the inflection point $s_i = 1$

$$\sigma(s_i) = \frac{1}{2} + \frac{h}{4}(s_i - 1) + \mathcal{O}((s_i-1)^2) \tag{5.25}$$

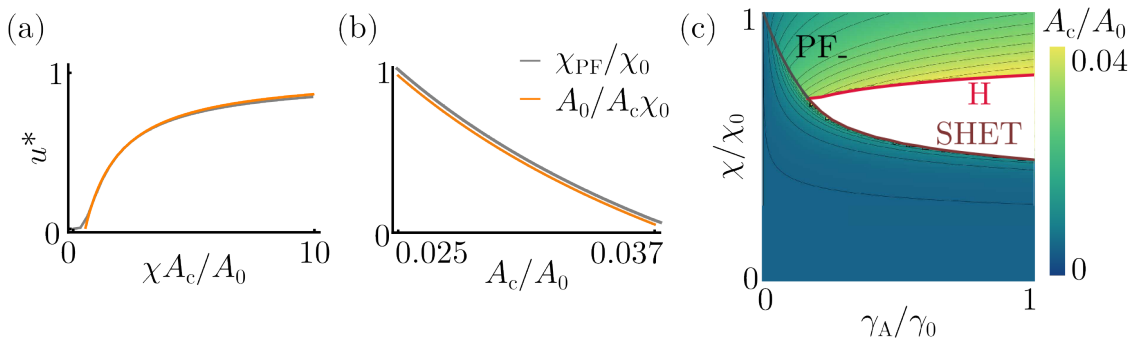

Figure 5.1. Uniform fixpoints of Eq. (2.72) computed numerically (gray) and approximation from linearization of the response function $\sigma(s_{ij})$ around $s_{ij} = 1$ [Eq. (5.27)], (orange), $h = 4$. (b) Comparison between Eq. (5.28) (orange) and the steady state contact area computed numerically along the supercritical pitchfork bifurcation line derived via continuation in MatCont (gray). (c) State diagram as shown in Fig. 3.3(a) for $\gamma_0/2\gamma_f = 0.98$. The color code indicates the normalized contact area at the fixpoint, i.e. at the uniform fixpoint state below the PF and SHET line and at the symmetry-broken fixpoints above the PF and Hopf line. The oscillatory regime between Hopf and SHET line is white as it does not contain any stable fixpoints.

yielding the dynamic equation

$$\tau_u \frac{du_i}{dt} = \frac{1}{2} + \frac{h}{4}(s_i - 1) - u_i \tag{5.26}$$

and using the definition of the signal Eq. (2.80) the uniform steady-state is

$$u^* = 1 - \frac{2+h}{4 + h\chi\dfrac{A_c}{A_0}}. \tag{5.27}$$

Linear stability analysis shows that this uniform steady state looses stability at

$$\chi_{PF} = \frac{4A_0}{hA_c}, \tag{5.28}$$

with $A_c = A_c(\gamma_c)$ and $\gamma_c = \gamma_0 - \gamma_A(u^*)^2$. Comparison with the steady-state contact area computed numerically along the supercritical pitchfork bifurcation line that was derived via continuation in MatCont shows good agreement [Fig. 5.1(b)]. Moreover, Figure 5.1(c) shows the normalized steady-state contact area A_c/A_0 in the state space of feedback parameters.

Timescale of symmetry-breaking

The time of symmetry-breaking T_{sym} [Fig. 3.2(b),blue curve] was computed as the simulation time (Mathematica) until 99% of the steady-state internal state difference $|u_1 - u_2|$

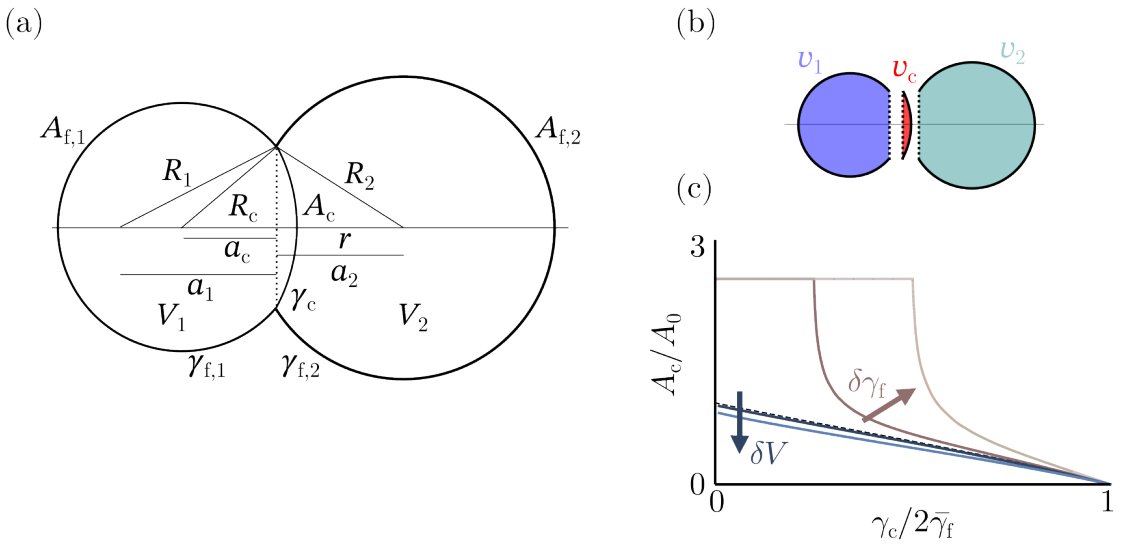

Figure 5.2. (a) Parameterization of a pair of asymmetric droplets adapted from [150]. (b) The droplet volumes can be expressed in terms of the three spherical cap volumes v_1, v_2, v_c. (c) Differences in droplet volumes $\delta V/\bar{V} = \{0.25, 0.5\}$ (blue) or outer interfacial tensions $\delta\gamma_f/\bar{\gamma}_f = \{0.25, 0.5\}$ (brown) change how the contact area between the droplets depends on the tension ratio $\gamma_c/2\bar{\gamma}_f$. Curves are obtained by numerically minimizing Eq. (5.36).

is reached, starting from initial conditions $(u_1, u_2) = (0.01, 0.02)$. The saddle and its eigenvalues [Fig. 3.2(b),red crosses] were found numerically in Mathematica from the intersections of nullclines. Eigenvalues were normalized against the maximum saddle eigenvalue at $\chi/\chi_0^{\mathrm{PF}} = 2, \gamma_A/\gamma_0 = 1$.

I - Equilibrium shapes of droplet pairs with asymmetric mechanical properties

For pairs of droplets with unequal volumes ($V_1 \neq V_2$) or outer surface tensions ($\gamma_{f,1} \neq \gamma_{f,2}$), Eq. (1.7) does not describe the size of the contact area. To derive the equilibrium shape and contact size of asymmetric droplets, I computed the minimum of the surface energy

$$E = \gamma_c A_c + \gamma_{f,1} A_{f,1} + \gamma_{f,2} A_{f,2} \tag{5.29}$$

under constant volume constraint. I followed the approach and used the parameterization introduced in [150], which is shown in Fig. 5.2(a). The droplet volumes can be expressed in terms of three spherical cap volumes v_i with $i \in \{1, 2, c\}$ [Fig. 5.2(b)] such that

$$V_1 = v_1 + v_c \tag{5.30}$$

$$V_2 = v_2 - v_c. \tag{5.31}$$

Given the radii of curvature R_i and the radius r as shown in Fig. 5.2(a), I can define the length scales

$$a_i = \sqrt{R_i^2 - r^2} \tag{5.32}$$

and surfaces

$$H_i(a_i, r) = \frac{1}{2}\left(a_i^2 + r^2 + a_i\sqrt{a_i^2 + r^2}\right), \tag{5.33}$$

which allows to express the spherical cap volumes as

$$v_i(a_i, r) = \frac{\pi}{3}\left(a_i + \sqrt{a_i^2 + r^2}\right)^2\left(2\sqrt{a_i^2 + r^2} - a_i\right) \tag{5.34}$$

and the different droplet surfaces as

$$A_i(a_i, r) = 4\pi H_i(a_i, r). \tag{5.35}$$

Using these definitions and expressing the outer surface tensions as $\gamma_{\mathrm{f},1} = \bar{\gamma}_\mathrm{f} + \delta\gamma_\mathrm{f}, \gamma_{\mathrm{f},2} = \bar{\gamma}_\mathrm{f} - \delta\gamma_\mathrm{f}$, I can rewrite Eq. (5.29) as

$$\begin{aligned}\frac{E}{4\pi\bar{\gamma}_\mathrm{f}} = &\left(1 + \frac{\delta\gamma_\mathrm{f}}{\bar{\gamma}_\mathrm{f}}\right)H_1(a_1, r) + \left(1 - \frac{\delta\gamma_\mathrm{f}}{\bar{\gamma}_\mathrm{f}}\right)H_2(a_2, r)\\ &+ 2\left(\frac{\gamma_\mathrm{c}}{2\bar{\gamma}_\mathrm{f}}\right)H_\mathrm{c}(a_\mathrm{c}, r)\end{aligned} \tag{5.36}$$

with $\bar{\gamma}_\mathrm{f} = (\gamma_{\mathrm{f},1} + \gamma_{\mathrm{f},2})/2$. The minima in terms of the four parameters $(a_1, a_2, a_\mathrm{c}, r)$ under constant volume constraints $V_1 = \bar{V} - \delta V, V_2 = \bar{V} + \delta V$ were computed numerically, allowing to derive the size of the contact area $A_\mathrm{c} = 4\pi H_c(a_c, r)$.

Specifically, to obtain estimates of the equilibrium shapes, I numerically computed the minimum of Eq. (5.36) in Mathematica [211]. I computed the contact area $A_\mathrm{c} = 4\pi H_c$ for values of $\gamma_\mathrm{c}/2\bar{\gamma}_\mathrm{f}$ evenly spaced on the interval $[0, 1]$. From these results, I fit the contact area as a function of the tension ratio [Fig. 5.2(c)], because my implementation of the numerical continuation method to obtain bifurcation lines required an explicit expression that relates the contact area to the interfacial tensions. For unequal volumes ($V_1 \neq V_2$), but identical outer surface tensions, I used a 5th order polynomial to fit a function $A_\mathrm{c} = A_\mathrm{c}(\gamma_\mathrm{c}/2\bar{\gamma}_\mathrm{f})$ on the interval $[0, 1]$ using Mathematica's function *Fit* with the default *LevenbergMarquardt* method [Fig. (5.2)(c)]. For droplets with asymmetric outer tension, but equal volumes, the droplet with higher outer tension is completely internalized if $\gamma_\mathrm{c}/2\bar{\gamma}_\mathrm{f} \leq \delta\gamma_\mathrm{f}$ [150], thus, I used a piecewise function to fit the contact area with $A_\mathrm{c} = 2^{4/3}A_0$ on the interval $[0, \delta\gamma_\mathrm{f}]$. The interval $[\delta\gamma_\mathrm{f}, 1]$ was fitted with a combination of a rational function of the form $a + b/(\gamma_\mathrm{c}/2\gamma_\mathrm{f} - c)^d$ close to the threshold of internalization with fit parameters $a - d$ and a 5th order polynomial [Fig. 5.2(c)]. Fits of the contact area were then used for continuation in MatCont and simulations in Mathematica to derive the state diagrams shown in Fig. 3.6.

J - Chapter 3 parameter values

The following table contains parameter values used in different figure panels of Chapter 3.

Physical quantity	Symbol	Values
Base line interfacial tension relative to outer surface tension in a single adherent droplet	$(\gamma_0 - \gamma_m)/2\gamma_f$	Fig. 3.1(a,c): 0.95
Base line interfacial tension relative to outer surface tension	$\gamma_0/2\gamma_f$	Fig. 3.2(a): 0.9 Fig. 3.2(c): 0.7 Fig. 3.3-3.7, 3.2, 5.1
Reference susceptibility	χ_0	Fig. 3.1: $\chi_0^{cusp} = 2.8612$ Fig. 3.2: $\chi_0^{PF} = 16.629$ Fig. 3.3-3.7, 5.1(c): $\chi_0 = 40.604$
Adaptive adhesion coefficient relative to outer surface tension	$\gamma_A/2\gamma_f$	Fig. 3.1(a, inlet): 0.9 Fig. 3.2(a, inlet): 0.8 Fig. 3.3(b): {square, triangle: 0.15, quarterfoil:0.21, star:0.23, cross:0.2352, pentagon:0.5} Fig. 3.3(d): 0.8 Fig. 3.3(e,f): {0.4, 0.6, 0.8} Fig. 3.7(b): 0.637 Fig. 3.7(c): {0.245, 0.637}
Relative signal susceptibility	χ/χ_0	Fig. 3.2(a, inset): 2.8 Fig. 3.3(b): {square:0.1, quarterfoil:0.61, star:0.604, cross:0.6021, pentagon:0.6, triangle:0.95} Fig. 3.3(c): {0.62,0.665,0.68} Fig. 3.3(d): {0.4704, 0.7388} Fig. 3.7(c): {0.3,0.465,0.4885 0.5,0.5221 0.6, 0.74,0.9 }
Volume asymmetry	$\delta V/\bar{V}$	Fig. 3.6: {0.25, 0.5}
Tension asymmetry	$\delta\gamma_f/\bar{\gamma}_f$	Fig. 3.6: {0.25, 0.5}
Hill coefficient	h	Fig. 3.1(a,b): 2 Fig. 3.2(a-c): 2 Fig. 3.3-3.7: 4

K - Computation of contact networks from neuromast live imaging data

Image segmentation

I implemented and tested an image segmentation pipeline for the live fluorescence microscopy data of neuromasts from a claudinb:mscarlet transgenic zebrafish line [Fig. 5.3], where a fluorophore is attached to proteins associated with the cell membrane, allowing to visualize the cell boundaries in the neuromast. The neural network based software PlantSeg [194] was used to enhance the membrane signal, which then served as input for the image segmentation software Cellpose [195]. Additional training of the Cellpose

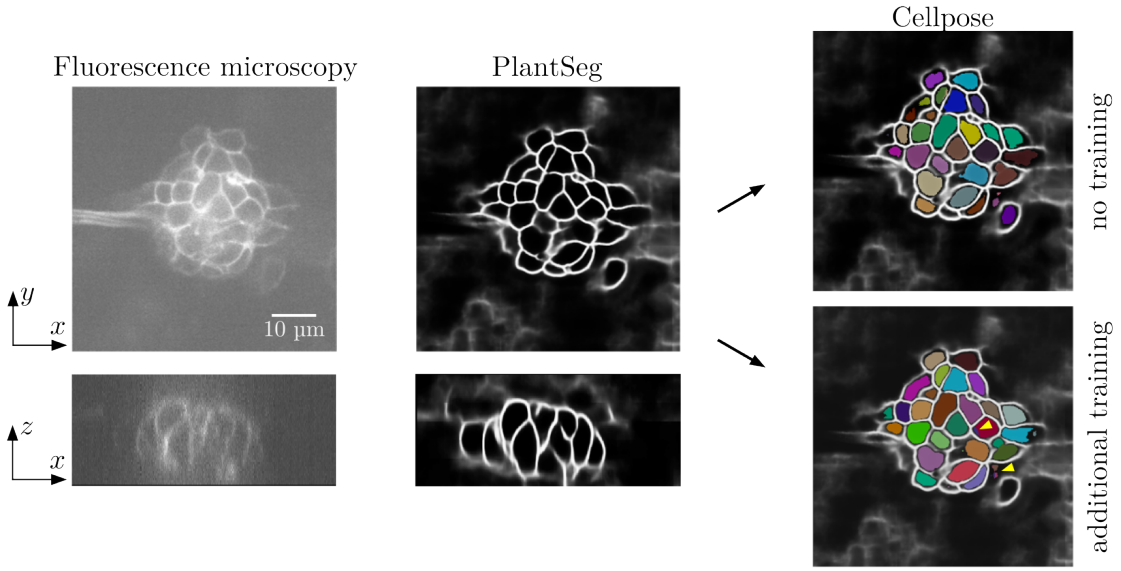

Figure 5.3. 3D segmentation pipeline for fluorescence microscopy data - The neural network based software PlantSeg [194] was used to enhance the membrane signal in fluorescence microscopy images (left) of a claudinb:mscarlet transgenic zebrafish line (images acquired by Adrian Jacobo, Biohub), which then served as input for the image segmentation software Cellpose [195]. Additional training of the cell pose model improved the segmentation results (bottom right), but did not suffice to completely remove artifacts like split cell volumes and small segmentation fragments (yellow arrow heads)

model improved the segmentation results [Fig. 5.3, bottom right] but did not suffice to completely remove artifacts like split cell volumes and small segmentation fragments (yellow arrow heads). The contact networks and simulations of contact-based signaling presented in this thesis (Section 4.8) were thus derived from images, segmented by Adrian Jacobo, Akilandeswari Balasubramanian and Tiger Lao (Biohub, San Francisco), using an alternative neural network-assisted pipeline [197], followed by manual refinement to correct errors and ensure high-quality cell volume detection.

Computing contact networks

All segmented datasets exhibited gaps between adjacent cells [Fig. 5.3]. To address these gaps, I applied a custom Python script dilating the segmented cell volumes to bring them into direct contact and to enable the measurement of cell-cell contact areas. Specifically, labeled volumes were iteratively convolved using the (*binary_dilation* function from the

scipy package [214]) with an isotropic mask (ball) of the form

$$\begin{bmatrix} 0 & 0 & 0 \\ 0 & 1 & 0 \\ 0 & 0 & 0 \end{bmatrix} \quad \begin{bmatrix} 0 & 1 & 0 \\ 1 & 1 & 1 \\ 0 & 1 & 0 \end{bmatrix} \quad \begin{bmatrix} 0 & 0 & 0 \\ 0 & 1 & 0 \\ 0 & 0 & 0 \end{bmatrix} \tag{5.37}$$

until volumes were in contact. Dilation with larger kernels (e.g. 5×5) only introduced minor differences in the contact networks, however, it enhances the bias through the selection of the labels expanded first in an iteration. Therefore, I chose the smallest possible convolution kernel. Images had a voxel resolution of $0.075\,\mu m \times 0.075\,\mu m \times 0.25\,\mu m$. To facilitate subsequent processing, images were binned in the x and y dimensions down to a voxel size of $0.3\,\mu m \times 0.3\,\mu m \times 0.25\,\mu m$, which is close to isotropic and justifies the usage of the above kernel.

L - Proof of existence of unique uniform states

In the following, I explain why for every parameter combination $k, \chi \in \mathcal{R}^+$, a unique uniform steady state solution of Eq. (4.2) exists [Chapter 4]. Let's define the function $h(u, \alpha) = (1 + \tanh(\alpha u))/2$, where $\alpha = k(1 - \chi \sum_j c_{ij})$. If u^* is a uniform steady state, then $h(\alpha, u^*) = u^*$. From the second derivative

$$\frac{\partial^2 h(\alpha, u)}{\partial u^2} = -\alpha^2 \frac{\sinh(\alpha u)}{\cosh^3(\alpha u)} \tag{5.38}$$

and $u \in [0, 1]$ follows that $h(u, \alpha)$ is strictly concave for $\alpha > 0$ and strictly convex for $\alpha < 0$ [Fig. 5.4]. Moreover, $h(0, \alpha) = 0.5\,\forall\alpha$ and $0 < h(\alpha, u) < 1\,\forall u \in [0, 1]$. It follows that for each $\alpha \in \mathbb{R}$, $h(\alpha, u^*) = u^*$ has a unique solution and thus Eq. (4.2) a unique uniform steady state.

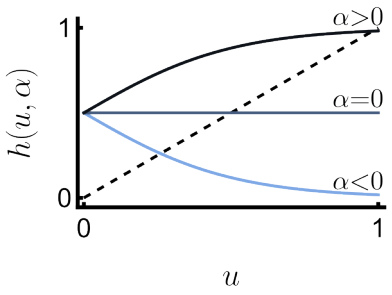

Figure 5.4. $h(u, \alpha) = u$ has a unique solution $u \in [0, 1]\ \forall\alpha \in \mathcal{R}$

List of publications

1	**Tim Dullweber**, Anna Erzberger **Mechanochemical feedback loops in contact-dependent fate patterning** *Current Opinion in Systems Biology* 2023 Mar:32-33 doi.org/10.1016/j.coisb.2023.100445	Chapter 1
2	**Tim Dullweber**, Roman Belousov, Anna Erzberger **Feedback between microscopic activity and macroscopic dynamics drives excitability and oscillations in mechanochemical matter** *Accepted at Physical Review E* doi.org/10.48550/arXiv.2411.15165	Chapter 2, Chapter 3
3	**Tim Dullweber**, Roman Belousov, Camilla Autorino, Nicoletta Petridou, Anna Erzberger **Shape Switching and Tunable Oscillations of Adaptive Droplets** *Under revision at Physical Review Letters* doi.org/10.48550/arXiv.2402.08664	Chapter 3
4	**Tim Dullweber**, Roman Belousov, Ergin Kohen Sagner, Anna Erzberger **Neuron-like signal processing in shape-adapting droplets** *In preparation*	Chapter 3

Bibliography

[1] Daniel Needleman and Zvonimir Dogic. Active matter at the interface between materials science and cell biology. *Nature reviews materials*, 2(9):1–14, 2017.

[2] Shiladitya Banerjee, Margaret L Gardel, and Ulrich S Schwarz. The actin cytoskeleton as an active adaptive material. *Annual review of condensed matter physics*, 11(1):421–439, 2020.

[3] Peter Fratzl, Michael Friedman, Karin Krauthausen, and Wolfgang Schäffner. *Active materials*. de Gruyter, 2021.

[4] Lars Onsager. Reciprocal relations in irreversible processes. i. *Physical review*, 37(4):405, 1931.

[5] Lars Onsager. Reciprocal relations in irreversible processes. ii. *Physical review*, 38(12):2265, 1931.

[6] Sara Dal Cengio, Demian Levis, and Ignacio Pagonabarraga. Linear response theory and green-kubo relations for active matter. *Physical review letters*, 123(23):238003, 2019.

[7] Frank Jülicher, Stephan W Grill, and Guillaume Salbreux. Hydrodynamic theory of active matter. *Reports on Progress in Physics*, 81(7):076601, 2018.

[8] Rita Mateus, Jana F Fuhrmann, and Natalie A Dye. Growth across scales: Dynamic signaling impacts tissue size and shape. *Current opinion in cell biology*, 73:50–57, 2021.

[9] Katharina F Sonnen, Volker M Lauschke, Julia Uraji, Henning J Falk, Yvonne Petersen, Maja C Funk, Mathias Beaupeux, Paul François, Christoph A Merten, and Alexander Aulehla. Modulation of phase shift between wnt and notch signaling oscillations controls mesoderm segmentation. *Cell*, 172(5):1079–1090, 2018.

[10] Alexis Pietak and Michael Levin. Bioelectrical control of positional information in development and regeneration: a review of conceptual and computational advances. *Progress in biophysics and molecular biology*, 137:52–68, 2018.

[11] Daniel J Cohen, W James Nelson, and Michel M Maharbiz. Galvanotactic control of collective cell migration in epithelial monolayers. *Nature materials*, 13(4):409–417, 2014.

[12] Fernando Ferreira, Sofia Moreira, Min Zhao, and Elias H Barriga. Stretch-induced endogenous electric fields drive directed collective cell migration in vivo. *Nature Materials*, pages 1–9, 2025.

[13] Min Zhao, Bing Song, Jin Pu, Teiji Wada, Brian Reid, Guangping Tai, Fei Wang, Aihua Guo, Petr Walczysko, Yu Gu, et al. Electrical signals control wound healing through phosphatidylinositol-3-oh kinase-γ and pten. *Nature*, 442(7101):457–460, 2006.

[14] Jan Rombouts, Jenna Elliott, and Anna Erzberger. Forceful patterning: theoretical principles of mechanochemical pattern formation. *EMBO reports*, page e57739, 2023.

[15] Tom Burkart, Manon C Wigbers, Laeschkir Würthner, and Erwin Frey. Control of protein-based pattern formation via guiding cues. *Nature Reviews Physics*, 4(8):511–527, 2022.

[16] Jacob Halatek, Fridtjof Brauns, and Erwin Frey. Self-organization principles of intracellular pattern formation. *Philosophical Transactions of the Royal Society B: Biological Sciences*, 373(1747):20170107, 2018.

[17] T Dullweber and A Erzberger. Mechanochemical feedback loops in contact-dependent fate patterning. *Current Opinion in Systems Biology*, page 100445, 2023.

[18] Peter Gross, K Vijay Kumar, and Stephan W Grill. How active mechanics and regulatory biochemistry combine to form patterns in development. *Annual review of biophysics*, 46(1):337–356, 2017.

[19] Edouard Hannezo and Carl-Philipp Heisenberg. Mechanochemical feedback loops in development and disease. *Cell*, 178(1):12–25, 2019.

[20] Yonit Maroudas-Sacks and Kinneret Keren. Mechanical patterning in animal morphogenesis. *Annual Review of Cell and Developmental Biology*, 37:469–493, 2021.

[21] Anaïs Bailles, Emily W Gehrels, and Thomas Lecuit. Mechanochemical principles of spatial and temporal patterns in cells and tissues. *Annual review of cell and developmental biology*, 38:321–347, 2022.

[22] Manon Valet, Eric D Siggia, and Ali H Brivanlou. Mechanical regulation of early vertebrate embryogenesis. *Nature Reviews Molecular Cell Biology*, 23(3):169–184, 2022.

[23] Sundar R Naganathan and Andrew C Oates. Mechanochemical coupling and developmental pattern formation. *Current Opinion in Systems Biology*, 5:104–111, 2017.

[24] Jacques Prost, Frank Jülicher, and Jean-François Joanny. Active gel physics. *Nature physics*, 11(2):111–117, 2015.

[25] Mark J Bowick, Nikta Fakhri, M Cristina Marchetti, and Sriram Ramaswamy. Symmetry, thermodynamics, and topology in active matter. *Physical Review X*, 12(1):010501, 2022.

[26] Oskar Hallatschek, Sujit S Datta, Knut Drescher, Jörn Dunkel, Jens Elgeti, Bartek Waclaw, and Ned S Wingreen. Proliferating active matter. *Nature Reviews Physics*, 5(7):407–419, 2023.

[27] National Academies of Sciences, Engineering, and Medicine. *Physics of Life*. The National Academies Press, Washington, DC, 2022.

[28] Pierre-Gilles Gennes, Françoise Brochard-Wyart, David Quéré, et al. *Capillarity and wetting phenomena: drops, bubbles, pearls, waves*. Springer, 2004.

[29] Kenneth A Brakke. The surface evolver. *Experimental mathematics*, 1(2):141–165, 1992.

[30] Daniel Bonn, Jens Eggers, Joseph Indekeu, Jacques Meunier, and Etienne Rolley. Wetting and spreading. *Reviews of modern physics*, 81(2):739–805, 2009.

[31] Bruno Andreotti and Jacco H Snoeijer. Statics and dynamics of soft wetting. *Annual review of fluid mechanics*, 52(1):285–308, 2020.

[32] Hans-Jürgen Butt and Michael Kappl. Normal capillary forces. *Advances in colloid and interface science*, 146(1-2):48–60, 2009.

[33] Bernardo Gouveia, Yoonji Kim, Joshua W Shaevitz, Sabine Petry, Howard A Stone, and Clifford P Brangwynne. Capillary forces generated by biomolecular condensates. *Nature*, 609(7926):255–264, 2022.

[34] J Arthur Thomson. On growth and form, 1917.

[35] Anahita Fathi-Azarbayjani, Abolghasem Jouyban, and Sui Yung Chan. Impact of surface tension in pharmaceutical sciences. *Journal of Pharmacy and Pharmaceutical Sciences*, 12(2):218–228, 2009.

[36] Kam Sang Kwok, Qi Huang, Massimo Mastrangeli, and David H Gracias. Self-folding using capillary forces. *Advanced Materials Interfaces*, 7(5):1901677, 2020.

[37] Thomas Young. Iii. an essay on the cohesion of fluids. *Philosophical transactions of the royal society of London*, (95):65–87, 1805.

[38] Chang Li, Ming Li, Zhongshi Ni, Qingwen Guan, Bamber RK Blackman, and Eduardo Saiz. Stimuli-responsive surfaces for switchable wettability and adhesion. *Journal of the Royal Society Interface*, 18(179):20210162, 2021.

[39] Bingwei Xin and Jingcheng Hao. Reversibly switchable wettability. *Chemical Society Reviews*, 39(2):769–782, 2010.

[40] Tatyana F Svitova and Meng C Lin. Dynamic interfacial properties of human tear-lipid films and their interactions with model-tear proteins in vitro. *Advances in colloid and interface science*, 233:4–24, 2016.

[41] David Quéré. Wetting and roughness. *Annu. Rev. Mater. Res.*, 38(1):71–99, 2008.

[42] Nicholas D Blelloch, Hana J Yarbrough, and Katherine A Mirica. Stimuli-responsive temporary adhesives: enabling debonding on demand through strategic molecular design. *Chemical science*, 12(46):15183–15205, 2021.

[43] Fei Guo and Zhiguang Guo. Inspired smart materials with external stimuli responsive wettability: a review. *RSC advances*, 6(43):36623–36641, 2016.

[44] Christine Selhuber, Jacques Blümmel, Fabian Czerwinski, and Joachim P Spatz. Tuning surface energies with nanopatterned substrates. *Nano letters*, 6(2):267–270, 2006.

[45] Guillaume Salbreux and Frank Jülicher. Mechanics of active surfaces. *Physical Review E*, 96(3):032404, 2017.

[46] Ewa Sitarska and Alba Diz-Muñoz. Pay attention to membrane tension: Mechanobiology of the cell surface. *Current opinion in cell biology*, 66:11–18, 2020.

[47] Erich Sackmann and Ana-Sunčana Smith. Physics of cell adhesion: some lessons from cell-mimetic systems. *Soft matter*, 10(11):1644–1659, 2014.

[48] Bruce Alberts, Rebecca Heald, Alexander Johnson, David Morgan, Martin Raff, Keith Roberts, and Peter Walter. *Molecular Biology of the Cell*. WW Norton & Company, 2022.

[49] Ulrich S Schwarz and Samuel A Safran. Physics of adherent cells. *Reviews of Modern Physics*, 85(3):1327, 2013.

[50] Jean-Léon Maître and Carl-Philipp Heisenberg. Three functions of cadherins in cell adhesion. *Current Biology*, 23(14):R626–R633, 2013.

[51] Tony Y-C Tsai, Rikki M Garner, and Sean G Megason. Adhesion-based self-organization in tissue patterning. *Annual Review of Cell and Developmental Biology*, 38:349–374, 2022.

[52] Satoshi Toda, Lucas R Blauch, Sindy KY Tang, Leonardo Morsut, and Wendell A Lim. Programming self-organizing multicellular structures with synthetic cell-cell signaling. *Science*, 361(6398):156–162, 2018.

[53] Jean-Léon Maître, Hélène Berthoumieux, Simon Frederik Gabriel Krens, Guillaume Salbreux, Frank Jülicher, Ewa Paluch, and Carl-Philipp Heisenberg. Adhesion functions in cell sorting by mechanically coupling the cortices of adhering cells. *science*, 338(6104):253–256, 2012.

[54] Ekaterina Papusheva and Carl-Philipp Heisenberg. Spatial organization of adhesion: force-dependent regulation and function in tissue morphogenesis. *The EMBO journal*, 29(16):2753–2768, 2010.

[55] Karen E Kasza, Amy C Rowat, Jiayu Liu, Thomas E Angelini, Clifford P Brangwynne, Gijsje H Koenderink, and David A Weitz. The cell as a material. *Current opinion in cell biology*, 19(1):101–107, 2007.

[56] Chii J Chan, Carl-Philipp Heisenberg, and Takashi Hiiragi. Coordination of morphogenesis and cell-fate specification in development. *Current Biology*, 27(18):R1024–R1035, 2017.

[57] Sirio Dupont and Sara A Wickström. Mechanical regulation of chromatin and transcription. *Nature Reviews Genetics*, 23(10):624–643, 2022.

[58] Shayan Shamipour, Silvia Caballero-Mancebo, and Carl-Philipp Heisenberg. Cytoplasm's got moves. *Developmental Cell*, 56(2):213–226, 2021.

[59] Masatoshi Nishikawa, Sundar Ram Naganathan, Frank Jülicher, and Stephan W Grill. Controlling contractile instabilities in the actomyosin cortex. *Elife*, 6:e19595, 2017.

[60] Mirjam Mayer, Martin Depken, Justin S Bois, Frank Jülicher, and Stephan W Grill. Anisotropies in cortical tension reveal the physical basis of polarizing cortical flows. *Nature*, 467(7315):617–621, 2010.

[61] Sven K Vogel, Zdenek Petrasek, Fabian Heinemann, and Petra Schwille. Myosin motors fragment and compact membrane-bound actin filaments. *Elife*, 2:e00116, 2013.

[62] Laeschkir Würthner, Andriy Goychuk, and Erwin Frey. Geometry-induced patterns through mechanochemical coupling. *Physical Review E*, 108(1):014404, 2023.

[63] Arnab Datta, Sagnik Ghosh, and Jane Kondev. How to assemble a scale-invariant gradient. *Elife*, 11:e71365, 2022.

[64] Naoki Tamemoto and Hiroshi Noguchi. Pattern formation in reaction–diffusion system on membrane with mechanochemical feedback. *Scientific reports*, 10(1):19582, 2020.

[65] Alexander Mietke, Frank Jülicher, and Ivo F Sbalzarini. Self-organized shape dynamics of active surfaces. *Proceedings of the National Academy of Sciences*, 116(1):29–34, 2019.

[66] Alexander Mietke, V Jemseena, K Vijay Kumar, Ivo F Sbalzarini, and Frank Jülicher. Minimal model of cellular symmetry breaking. *Physical review letters*, 123(18):188101, 2019.

[67] Francis Corson, Lydie Couturier, Hervé Rouault, Khalil Mazouni, and François Schweisguth. Self-organized notch dynamics generate stereotyped sensory organ patterns in drosophila. *Science*, 356(6337):eaai7407, 2017.

[68] A Erzberger, A Jacobo, A Dasgupta, and AJ Hudspeth. Mechanochemical symmetry breaking during morphogenesis of lateral-line sensory organs. *Nature physics*, 16(9):949–957, 2020.

[69] David Sprinzak and Stephen C Blacklow. Biophysics of notch signaling. *Annual review of biophysics*, 50:157–189, 2021.

[70] Sarah J Bray. Notch signalling in context. *Nature reviews Molecular cell biology*, 17(11):722–735, 2016.

[71] Laura Blackie, Melda Tozluoglu, Mateusz Trylinski, Rhian F Walther, François Schweisguth, Yanlan Mao, and Franck Pichaud. A combination of notch signaling, preferential adhesion and endocytosis induces a slow mode of cell intercalation in the drosophila retina. *Development*, 148(10):dev197301, 2021.

[72] Vanessa Barone, Moritz Lang, SF Gabriel Krens, Saurabh J Pradhan, Shayan Shamipour, Keisuke Sako, Mateusz Sikora, Călin C Guet, and Carl-Philipp Heisenberg. An effective feedback loop between cell-cell contact duration and morphogen signaling determines cell fate. *Developmental cell*, 43(2):198–211, 2017.

[73] Oren Shaya, Udi Binshtok, Micha Hersch, Dmitri Rivkin, Sheila Weinreb, Liat Amir-Zilberstein, Bassma Khamaisi, Olya Oppenheim, Ravi A Desai, Richard J Goodyear, et al. Cell-cell contact area affects notch signaling and notch-dependent patterning. *Developmental cell*, 40(5):505–511, 2017.

[74] Itzhak Khait, Yuval Orsher, Ohad Golan, Udi Binshtok, Nadav Gordon-Bar, Liat Amir-Zilberstein, and David Sprinzak. Quantitative analysis of delta-like 1 membrane dynamics elucidates the role of contact geometry on notch signaling. *Cell reports*, 14(2):225–233, 2016.

[75] Shahar Kasirer and David Sprinzak. Interplay between notch signaling and mechanical forces during developmental patterning processes. *Current Opinion in Cell Biology*, 91:102444, 2024.

[76] Pamela J Lanford, Yu Lan, Rulang Jiang, Claire Lindsell, Gerry Weinmaster, Thomas Gridley, and Matthew W Kelley. Notch signalling pathway mediates hair cell development in mammalian cochlea. *Nature genetics*, 21(3):289–292, 1999.

[77] Annette K Lewis, Gretchen D Frantz, David A Carpenter, Frederic J de Sauvage, and Wei-Qiang Gao. Distinct expression patterns of notch family receptors and ligands during

development of the mammalian inner ear. *Mechanisms of development*, 78(1-2):159–163, 1998.

[78] Indra Wibowo, Filipe Pinto-Teixeira, Chie Satou, Shin-ichi Higashijima, and Hernán López-Schier. Compartmentalized notch signaling sustains epithelial mirror symmetry. *Development*, 138(6):1143–1152, 2011.

[79] Hideru Togashi, Kanoko Kominami, Masazumi Waseda, Hitomi Komura, Jun Miyoshi, Masatoshi Takeichi, and Yoshimi Takai. Nectins establish a checkerboard-like cellular pattern in the auditory epithelium. *Science*, 333(6046):1144–1147, 2011.

[80] Roie Cohen, Liat Amir-Zilberstein, Micha Hersch, Shiran Woland, Olga Loza, Shahar Taiber, Fumio Matsuzaki, Sven Bergmann, Karen B Avraham, and David Sprinzak. Mechanical forces drive ordered patterning of hair cells in the mammalian inner ear. *Nature communications*, 11(1):5137, 2020.

[81] Roie Cohen, Shahar Taiber, Olga Loza, Shahar Kasirer, Shiran Woland, and David Sprinzak. Mechano-signaling feedback underlies precise inner hair cell patterning in the organ of corti. bioRxiv, 2022. doi: 10.1101/2019.12.11.123456.

[82] Jeffrey T Corwin and Douglas A Cotanche. Regeneration of sensory hair cells after acoustic trauma. *Science*, 240(4860):1772–1774, 1988.

[83] Filipe Pinto-Teixeira, Oriol Viader-Llargués, Elen Torres-Mejía, Melissa Turan, Estela González-Gualda, Laura Pola-Morell, and Hernán López-Schier. Inexhaustible hair-cell regeneration in young and aged zebrafish. *Biology open*, 4(7):903–909, 2015.

[84] GW Rouse and JO Pickles. Paired development of hair cells in neuromasts of the teleost lateral line. *Proceedings of the Royal Society of London. Series B: Biological Sciences*, 246(1316):123–128, 1991.

[85] Hernán López-Schier and AJ Hudspeth. A two-step mechanism underlies the planar polarization of regenerating sensory hair cells. *Proceedings of the National Academy of Sciences*, 103(49):18615–18620, 2006.

[86] Eva Y Ma, Edwin W Rubel, and David W Raible. Notch signaling regulates the extent of hair cell regeneration in the zebrafish lateral line. *Journal of Neuroscience*, 28(9):2261–2273, 2008.

[87] Adrian Jacobo, Agnik Dasgupta, Anna Erzberger, Kimberly Siletti, and AJ Hudspeth. Notch-mediated determination of hair-bundle polarity in mechanosensory hair cells of the zebrafish lateral line. *Current Biology*, 29(21):3579–3587, 2019.

[88] Eva L Kozak, Subarna Palit, Jerónimo R Miranda-Rodríguez, Aleksandar Janjic, Anika Böttcher, Heiko Lickert, Wolfgang Enard, Fabian J Theis, and Hernán López-Schier.

Epithelial planar bipolarity emerges from notch-mediated asymmetric inhibition of emx2. *Current Biology*, 30(6):1142–1151, 2020.

[89] Francis Corson and Eric D Siggia. Gene-free methodology for cell fate dynamics during development. *Elife*, 6:e30743, 2017.

[90] Melinda Liu Perkins, Dirk Benzinger, Murat Arcak, and Mustafa Khammash. Cell-in-the-loop pattern formation with optogenetically emulated cell-to-cell signaling. *Nature communications*, 11(1):1355, 2020.

[91] Shwan B Javdan and Tara L Deans. Design and development of engineered receptors for cell and tissue engineering. *Current Opinion in Systems Biology*, 28:100363, 2021.

[92] Leonardo Morsut, Kole T Roybal, Xin Xiong, Russell M Gordley, Scott M Coyle, Matthew Thomson, and Wendell A Lim. Engineering customized cell sensing and response behaviors using synthetic notch receptors. *Cell*, 164(4):780–791, 2016.

[93] Jonathan E Dawson, Abby Bryant, Breana Walton, Simran Bhikot, Shawn Macon, Amber Ajamu-Johnson, Trevor Jordan, Paul D Langridge, and Abdul N Malmi-Kakkada. Contact area and tissue growth dynamics shape synthetic juxtacrine signaling patterns. *Biophysical Journal*, 124(1):93–106, 2025.

[94] Zena Hadjivasiliou, Ginger L Hunter, and Buzz Baum. A new mechanism for spatial pattern formation via lateral and protrusion-mediated lateral signalling. *Journal of the Royal Society Interface*, 13(124):20160484, 2016.

[95] Daniel Boocock, Naoya Hino, Natalia Ruzickova, Tsuyoshi Hirashima, and Édouard Hannezo. Theory of mechanochemical patterning and optimal migration in cell monolayers. *Nature physics*, 17(2):267–274, 2021.

[96] Alexander Ziepke, Ivan Maryshev, Igor S Aranson, and Erwin Frey. Multi-scale organization in communicating active matter. *Nature communications*, 13(1):6727, 2022.

[97] Ranjith Viswanathan, Aleksandar Necakov, Mateusz Trylinski, Rohit Krishnan Harish, Daniel Krueger, Emilia Esposito, Francois Schweisguth, Pierre Neveu, and Stefano De Renzis. Optogenetic inhibition of delta reveals digital notch signalling output during tissue differentiation. *EMBO reports*, 20(12):e47999, 2019.

[98] ChangHwan Lee, Tina Lynch, Sarah L Crittenden, and Judith Kimble. Image-based single-molecule analysis of notch-dependent transcription in its natural context. In *Notch Signaling Research: Methods and Protocols*. Springer US, 2022. 131–149.

[99] Udi Binshtok and David Sprinzak. Modeling the notch response. *Molecular Mechanisms of Notch Signaling*, pages 79–98, 2018.

[100] Jose Negrete Jr and Andrew C Oates. Embryonic lateral inhibition as optical modes: An analytical framework for mesoscopic pattern formation. *Physical Review E*, 99(4):042417, 2019.

[101] JM Sancho and Marta Ibañes. Landau theory for cellular patterns driven by lateral inhibition interaction. *Physical Review E*, 102(3):032404, 2020.

[102] Supriya Bajpai, Ranganathan Prabhakar, Raghunath Chelakkot, and Mandar M Inamdar. Role of cell polarity dynamics and motility in pattern formation due to contact-dependent signalling. *Journal of The Royal Society Interface*, 18(175):20200825, 2021.

[103] Toshiki Oguma, Hisako Takigawa-Imamura, Tomoyasu Shinoda, Shuntaro Ogura, Akiyoshi Uemura, Takaki Miyata, Philip K Maini, and Takashi Miura. Analyzing the effect of cell rearrangement on delta-notch pattern formation. arXiv, 2021. doi: 10.48550/ARXIV.2112.00208.

[104] Supriya Bajpai, Raghunath Chelakkot, Ranganathan Prabhakar, and Mandar M Inamdar. Role of delta-notch signalling molecules on cell–cell adhesion in determining heterogeneous chemical and cell morphological patterning. *Soft Matter*, 18(18):3505–3520, 2022.

[105] Tim Dullweber, Roman Belousov, and Anna Erzberger. Shape switching and tunable oscillations of adaptive droplets. *arXiv preprint arXiv:2402.08664*, 2024.

[106] Tim Dullweber, Roman Belousov, and Anna Erzberger. Feedback between microscopic activity and macroscopic dynamics drives excitability and oscillations in mechanochemical matter. *arXiv preprint arXiv:2411.15165*, 2024.

[107] Xiaomin Shi and Jeffrey R Reimers. Understanding non-linear effects from hill-type dynamics with application to decoding of p53 signaling. *Scientific Reports*, 8(1):2147, 2018.

[108] Julien Dubrulle, Benjamin M Jordan, Laila Akhmetova, Jeffrey A Farrell, Seok-Hyung Kim, Lilianna Solnica-Krezel, and Alexander F Schier. Response to nodal morphogen gradient is determined by the kinetics of target gene induction. *Elife*, 4:e05042, 2015.

[109] Claudio Collinet and Thomas Lecuit. Programmed and self-organized flow of information during morphogenesis. *Nature Reviews Molecular Cell Biology*, 22(4):245–265, 2021.

[110] Stephan Hausberg and Matthias Röger. Well-posedness and fast-diffusion limit for a bulk–surface reaction–diffusion system. *Nonlinear Differential Equations and Applications NoDEA*, 25(3):17, 2018.

[111] Fridtjof Brauns, Jacob Halatek, and Erwin Frey. Phase-space geometry of mass-conserving reaction-diffusion dynamics. *Physical Review X*, 10(4):041036, 2020.

[112] Alison Barbara Ross, Julian David Langer, and Marko Jovanovic. Proteome turnover in the spotlight: approaches, applications, and perspectives. *Molecular & Cellular Proteomics*, 20, 2021.

[113] Christopher Buccitelli and Matthias Selbach. mrnas, proteins and the emerging principles of gene expression control. *Nature Reviews Genetics*, 21(10):630–644, 2020.

[114] Maya Shamir, Yinon Bar-On, Rob Phillips, and Ron Milo. Snapshot: Timescales in cell biology. *Cell*, 164(6):1302–1302.e1, 2016.

[115] Emma V Rusilowicz-Jones, Sylvie Urbé, and Michael J Clague. Protein degradation on the global scale. *Molecular Cell*, 2022.

[116] Tom Wyatt, Buzz Baum, and Guillaume Charras. A question of time: tissue adaptation to mechanical forces. *Current opinion in cell biology*, 38:68–73, 2016.

[117] Jagadish Sankaran, Manoj Manna, Lin Guo, Rachel Kraut, and Thorsten Wohland. Diffusion, transport, and cell membrane organization investigated by imaging fluorescence cross-correlation spectroscopy. *Biophysical journal*, 97(9):2630–2639, 2009.

[118] Stephan Hausberg and Matthias Röger. Well-posedness and fast-diffusion limit for a bulk–surface reaction–diffusion system. *Nonlinear Differential Equations and Applications NoDEA*, 25:1–32, 2018.

[119] Sivaramakrishnan Ramadurai, Andrea Holt, Victor Krasnikov, Geert Van Den Bogaart, J Antoinette Killian, and Bert Poolman. Lateral diffusion of membrane proteins. *Journal of the American Chemical Society*, 131(35):12650–12656, 2009.

[120] Lena Tveriakhina, Gustavo Scanavachi, Emily D Egan, Ricardo Bango Da Cunha Correia, Alexandre P Martin, Julia M Rogers, Jeremy S Yodh, Jon C Aster, Tom Kirchhausen, and Stephen C Blacklow. Temporal dynamics and stoichiometry in human notch signaling from notch synaptic complex formation to nuclear entry of the notch intracellular domain. *Developmental Cell*, 59(11):1425–1438, 2024.

[121] David T Gonzales, Surased Suraritdechachai, Christoph Zechner, and T-Y Dora Tang. Bidirectional communication between droplet interface bilayers driven by cell-free quorum sensing gene circuits. *ChemSystemsChem*, 5(6):e202300029, 2023.

[122] Benjamin L Beckstead, Jason C Tung, Katharine J Liang, Zarry Tavakkol, Marcia L Usui, John E Olerud, and Cecilia M Giachelli. Methods to promote notch signaling at the biomaterial interface and evaluation in a rafted organ culture model. *Journal of Biomedical Materials Research Part A: An Official Journal of The Society for Biomaterials, The Japanese Society for Biomaterials, and The Australian Society for Biomaterials and the Korean Society for Biomaterials*, 91(2):436–446, 2009.

[123] Ling-Gang Wu, Edaeni Hamid, Wonchul Shin, and Hsueh-Cheng Chiang. Exocytosis and endocytosis: modes, functions, and coupling mechanisms. *Annual review of physiology*, 76(1):301–331, 2014.

[124] Bruce Alberts, Rebecca Heald, Alexander Johnson, David Morgan, Martin Raff, Keith Roberts, and Peter Walter. *Molecular Biology of the Cell*. WW Norton & Company, 2022.

[125] Scott Berry and Lucas Pelkmans. Mechanisms of cellular mrna transcript homeostasis. *Trends in Cell Biology*, 32(8):655–668, 2022.

[126] Andrea Brigitta Alber and David Michael Suter. Dynamics of protein synthesis and degradation through the cell cycle. *Cell Cycle*, 18(8):784–794, 2019.

[127] Feyza Nur Arslan, Édouard Hannezo, Jack Merrin, Martin Loose, and Carl-Philipp Heisenberg. Adhesion-induced cortical flows pattern e-cadherin-mediated cell contacts. *Current Biology*, 34(1):171–182, 2024.

[128] Kentner L Singleton, Kole T Roybal, Yi Sun, Guo Fu, Nicholas RJ Gascoigne, Nicolai SC Van Oers, and Christoph Wülfing. Spatiotemporal patterning during t cell activation is highly diverse. *Science signaling*, 2(65):ra15–ra15, 2009.

[129] Ken Jacobson, Ping Liu, and B Christoffer Lagerholm. The lateral organization and mobility of plasma membrane components. *Cell*, 177(4):806–819, 2019.

[130] William S Trimble and Sergio Grinstein. Barriers to the free diffusion of proteins and lipids in the plasma membrane. *Journal of Cell Biology*, 208(3):259–271, 2015.

[131] Ekaterina Seib and Thomas Klein. The role of ligand endocytosis in notch signalling. *Biology of the Cell*, 113(10):401–418, 2021.

[132] Elenaé Vázquez-Ulloa, Kai-Lan Lin, Marcela Lizano, and Cecilia Sahlgren. Reversible and bidirectional signaling of notch ligands. *Critical Reviews in Biochemistry and Molecular Biology*, 57(4):377–398, 2022.

[133] Vasundhara Kandachar and Fabrice Roegiers. Endocytosis and control of notch signaling. *Current opinion in cell biology*, 24(4):534–540, 2012.

[134] Ana-Sunčana Smith and Udo Seifert. Vesicles as a model for controlled (de-) adhesion of cells: a thermodynamic approach. *Soft Matter*, 3(3):275–289, 2007.

[135] Ana-Sunčana Smith and Udo Seifert. Effective adhesion strength of specifically bound vesicles. *Physical Review E—Statistical, Nonlinear, and Soft Matter Physics*, 71(6):061902, 2005.

[136] Udo Seifert and Reinhard Lipowsky. Adhesion of vesicles. *Physical Review A*, 42(8):4768, 1990.

[137] Jean-Léon Maître and Carl-Philipp Heisenberg. The role of adhesion energy in controlling cell–cell contacts. *Current opinion in cell biology*, 23(5):508–514, 2011.

[138] Yeh-Shiu Chu, William A Thomas, Olivier Eder, Frederic Pincet, Eric Perez, Jean Paul Thiery, and Sylvie Dufour. Force measurements in e-cadherin–mediated cell doublets reveal rapid adhesion strengthened by actin cytoskeleton remodeling through rac and cdc42. *The Journal of cell biology*, 167(6):1183–1194, 2004.

[139] Moises Santillán. On the use of the hill functions in mathematical models of gene regulatory networks. *Mathematical Modelling of Natural Phenomena*, 3(2):85–97, 2008.

[140] Joanne R Collier, Nicholas AM Monk, Philip K Maini, and Julian H Lewis. Pattern formation by lateral inhibition with feedback: a mathematical model of delta-notch intercellular signalling. *Journal of Theoretical Biology*, 183(4):429–446, 1996.

[141] Ma Xenia G Ilagan, Sora Lim, Mary Fulbright, David Piwnica-Worms, and Raphael Kopan. Real-time imaging of notch activation with a luciferase complementation-based reporter. *Science signaling*, 4(181):rs7–rs7, 2011.

[142] Christy J Fryer, J Brandon White, and Katherine A Jones. Mastermind recruits cycc: Cdk8 to phosphorylate the notch icd and coordinate activation with turnover. *Molecular cell*, 16(4):509–520, 2004.

[143] Marika Sjöqvist and Emma R Andersson. Do as i say, not (ch) as i do: Lateral control of cell fate. *Developmental biology*, 447(1):58–70, 2019.

[144] Tim Dullweber, Roman Belousov, and Anna Erzberger. Shape switching and tunable shape oscillations of adaptive droplets. *arXiv preprint arXiv:2402.08664*, 2024.

[145] Roma Olsauskas-Kuprys, Andrei Zlobin, and Clodia Osipo. Gamma secretase inhibitors of notch signaling. *OncoTargets and therapy*, pages 943–955, 2013.

[146] Roie Cohen, Shahar Taiber, Olga Loza, Shahar Kasirer, Shiran Woland, and David Sprinzak. Precise alternating cellular pattern in the inner ear by coordinated hopping intercalations and delaminations. *Science Advances*, 9(8):eadd2157, 2023.

[147] Kazunori Yamamoto, Sacha Ichbiah, Joana Pinto, Fabrice Delbary, Nate Goehring, Hervé Turlier, and Guillaume Charras. Dissecting the subcellular forces sculpting early c. elegans embryos. *bioRxiv*, pages 2023–03, 2023.

[148] Benoit G Godard, Rémi Dumollard, Edwin Munro, Janet Chenevert, Céline Hebras, Alex McDougall, and Carl-Philipp Heisenberg. Apical relaxation during mitotic rounding promotes tension-oriented cell division. *Developmental Cell*, 55(6):695–706, 2020.

[149] Priyamvada Chugh, Andrew G Clark, Matthew B Smith, Davide AD Cassani, Kai Dierkes, Anan Ragab, Philippe P Roux, Guillaume Charras, Guillaume Salbreux, and Ewa K Paluch. Actin cortex architecture regulates cell surface tension. *Nature cell biology*, 19(6):689–697, 2017.

[150] Jean-Léon Maître, Hervé Turlier, Rukshala Illukkumbura, Björn Eismann, Ritsuya Niwayama, François Nédélec, and Takashi Hiiragi. Asymmetric division of contractile domains couples cell positioning and fate specification. *Nature*, 536(7616):344–348, 2016.

[151] Elisabeth Fischer-Friedrich, Anthony A Hyman, Frank Jülicher, Daniel J Müller, and Jonne Helenius. Quantification of surface tension and internal pressure generated by single mitotic cells. *Scientific reports*, 4(1):6213, 2014.

[152] Chloé Roffay, Chii J Chan, Boris Guirao, Takashi Hiiragi, and François Graner. Inferring cell junction tension and pressure from cell geometry. *Development*, 148(18):dev192773, 2021.

[153] Dagmar Fichtner, Bärbel Lorenz, Sinem Engin, Christina Deichmann, Marieelen Oelkers, Andreas Janshoff, Andre Menke, Doris Wedlich, and Clemens M Franz. Covalent and density-controlled surface immobilization of e-cadherin for adhesion force spectroscopy. *PLoS One*, 9(3):e93123, 2014.

[154] Dimitri Fabrèges, Bernat Corominas-Murtra, Prachiti Moghe, Alison Kickuth, Takafumi Ichikawa, Chizuru Iwatani, Tomoyuki Tsukiyama, Nathalie Daniel, Julie Gering, Anniek Stokkermans, et al. Temporal variability and cell mechanics control robustness in mammalian embryogenesis. *Science*, 386(6718):eadh1145, 2024.

[155] Alexander N Pisarchik and Alexander E Hramov. *Multistability in Physical and Living Systems*, volume 2. Springer, 2022.

[156] Nicholas Blackbeard, Simon Osborne, Stephen O'Brien, and Andreas Amann. Bursting: when a cusp and a pitchfork interact. *arXiv preprint arXiv:1210.4484*, 2012.

[157] Edward Yu Bormashenko. *Physics of wetting: phenomena and applications of fluids on surfaces*. Walter de Gruyter GmbH & Co KG, 2017.

[158] Jack Binysh, Thomas R Wilks, and Anton Souslov. Active elastocapillarity in soft solids with negative surface tension. *Science advances*, 8(10):eabk3079, 2022.

[159] Marcelo Boareto, Mohit Kumar Jolly, Eshel Ben-Jacob, and José N Onuchic. Jagged mediates differences in normal and tumor angiogenesis by affecting tip-stalk fate decision. *Proceedings of the National Academy of Sciences*, 112(29):E3836–E3844, 2015.

[160] Eugene M Izhikevich. *Dynamical systems in neuroscience*. MIT press, 2007.

[161] Isam Al-Darabsah and Sue Ann Campbell. M-current induced bogdanov–takens bifurcation and switching of neuron excitability class. *The Journal of Mathematical Neuroscience*, 11(1):1–26, 2021.

[162] Christoph Kirst, Julian Ammer, Felix Felmy, Andreas Herz, and Martin Stemmler. Gaba regulates resonance and spike rate encoding via a universal mechanism that underlies the modulation of action potential generation. *bioRxiv*, page 206581, 2017.

[163] Walter G Gall and Ying Zhou. An organizing center for planar neural excitability. *Neurocomputing*, 32:757–765, 2000.

[164] William Bialek. *Biophysics: searching for principles*. Princeton University Press, 2012.

[165] Nicoletta I Petridou, Bernat Corominas-Murtra, Carl-Philipp Heisenberg, and Edouard Hannezo. Rigidity percolation uncovers a structural basis for embryonic tissue phase transitions. *Cell*, 184(7):1914–1928, 2021.

[166] Isabella R. Graf and Benjamin B. Machta. A bifurcation integrates information from many noisy ion channels and allows for milli-kelvin thermal sensitivity in the snake pit organ. *Proceedings of the National Academy of Sciences*, 121(6):e2308215121, 2024.

[167] Nagarajan Nandagopal, Leah A Santat, Lauren LeBon, David Sprinzak, Marianne E Bronner, and Michael B Elowitz. Dynamic ligand discrimination in the notch signaling pathway. *Cell*, 172(4):869–880, 2018.

[168] Aneta Koseska and Philippe IH Bastiaens. Cell signaling as a cognitive process. *The EMBO journal*, 36(5):568–582, 2017.

[169] Jeremy E Purvis and Galit Lahav. Encoding and decoding cellular information through signaling dynamics. *Cell*, 152(5):945–956, 2013.

[170] Caroline S Hill. Spatial and temporal control of nodal signaling. *Current opinion in cell biology*, 51:50–57, 2018.

[171] Alvaro Tejero-Cantero, Jan Boelts, Michael Deistler, Jan-Matthis Lueckmann, Conor Durkan, Pedro J. Gonçalves, David S. Greenberg, and Jakob H. Macke. sbi: A toolkit for simulation-based inference. *Journal of Open Source Software*, 5(52):2505, 2020.

[172] Caroline S Hill. Establishment and interpretation of nodal and bmp signaling gradients in early vertebrate development. *Current topics in developmental biology*, 149:311–340, 2022.

[173] Patrick Müller, Katherine W Rogers, Ben M Jordan, Joon S Lee, Drew Robson, Sharad Ramanathan, and Alexander F Schier. Differential diffusivity of nodal and lefty underlies a reaction-diffusion patterning system. *Science*, 336(6082):721–724, 2012.

[174] Wiebke Drenckhan and Stefan Hutzler. Structure and energy of liquid foams. *Advances in colloid and interface science*, 224:1–16, 2015.

[175] Katherine W Rogers and Alexander F Schier. Morphogen gradients: from generation to interpretation. *Annual review of cell and developmental biology*, 27(1):377–407, 2011.

[176] Thomas Gregor, David W Tank, Eric F Wieschaus, and William Bialek. Probing the limits to positional information. *Cell*, 130(1):153–164, 2007.

[177] Subrahmanyan Chandrasekhar. Stochastic problems in physics and astronomy. *Reviews of modern physics*, 15(1):1, 1943.

[178] Sabine Witzel, Vitaly Zimyanin, Filipa Carreira-Barbosa, Masazumi Tada, and Carl-Philipp Heisenberg. Wnt11 controls cell contact persistence by local accumulation of frizzled 7 at the plasma membrane. *The Journal of cell biology*, 175(5):791–802, 2006.

[179] Florian Ulrich, Michael Krieg, Eva-Maria Schötz, Vinzenz Link, Irinka Castanon, Viktor Schnabel, Anna Taubenberger, Daniel Mueller, Pierre-Henri Puech, and Carl-Philipp Heisenberg. Wnt11 functions in gastrulation by controlling cell cohesion through rab5c and e-cadherin. *Developmental cell*, 9(4):555–564, 2005.

[180] Antonius L van Boxtel, John E Chesebro, Claire Heliot, Marie-Christine Ramel, Richard K Stone, and Caroline S Hill. A temporal window for signal activation dictates the dimensions of a nodal signaling domain. *Developmental cell*, 35(2):175–185, 2015.

[181] Bradley Efron. *The jackknife, the bootstrap and other resampling plans*. SIAM, 1982.

[182] Zena Hadjivasiliou and Ginger Hunter. Talking to your neighbors across scales: Long-distance notch signaling during patterning. *Current topics in developmental biology*, 150:299–334, 2022.

[183] Antonio Totaro, Martina Castellan, Giusy Battilana, Francesca Zanconato, Luca Azzolin, Stefano Giulitti, Michelangelo Cordenonsi, and Stefano Piccolo. Yap/taz link cell mechanics to notch signalling to control epidermal stem cell fate. *Nature communications*, 8(1):15206, 2017.

[184] Ovijit Chaudhuri, Justin Cooper-White, Paul A Janmey, David J Mooney, and Vivek B Shenoy. Effects of extracellular matrix viscoelasticity on cellular behaviour. *Nature*, 584(7822):535–546, 2020.

[185] Eric D Thomas, Ivan A Cruz, Dale W Hailey, and David W Raible. There and back again: development and regeneration of the zebrafish lateral line system. *Wiley Interdisciplinary Reviews: Developmental Biology*, 4(1):1–16, 2015.

[186] Sungmin Baek, Nhung TT Tran, Daniel C Diaz, Ya-Yin Tsai, Joaquin Navajas Acedo, Mark E Lush, and Tatjana Piotrowski. Single-cell transcriptome analysis reveals three sequential phases of gene expression during zebrafish sensory hair cell regeneration. *Developmental cell*, 57(6):799–819, 2022.

[187] Motoyuki Itoh and Ajay B Chitnis. Expression of proneural and neurogenic genes in the zebrafish lateral line primordium correlates with selection of hair cell fate in neuromasts. *Mechanisms of development*, 102(1-2):263–266, 2001.

[188] Agnė Kozlovskaja-Gumbrienė, Ren Yi, Richard Alexander, Andy Aman, Ryan Jiskra, Danielle Nagelberg, Holger Knaut, Melainia McClain, and Tatjana Piotrowski. Proliferation-independent regulation of organ size by fgf/notch signaling. *Elife*, 6:e21049, 2017.

[189] Linjia Jiang, Andres Romero-Carvajal, Jeff S Haug, Christopher W Seidel, and Tatjana Piotrowski. Gene-expression analysis of hair cell regeneration in the zebrafish lateral line. *Proceedings of the National Academy of Sciences*, 111(14):E1383–E1392, 2014.

[190] Nara Guisoni, Rosa Martinez-Corral, Jordi Garcia-Ojalvo, and Joaquín de Navascués. Diversity of fate outcomes in cell pairs under lateral inhibition. *Development*, 144(7):1177–1186, 2017.

[191] Natalia G Lavalle, Jerónimo Miranda-Rodríguez, Emanuel Cura Costa, Augusto Borges, Oriol Viader-Llargués, Hernán López-Schier, and Osvaldo Chara. Local control of cellular proliferation underlies neuromast regeneration in zebrafish. *bioRxiv*, pages 2024–10, 2024.

[192] Johannes Schindelin, Ignacio Arganda-Carreras, Erwin Frise, Verena Kaynig, Mark Longair, Tobias Pietzsch, Stephan Preibisch, Curtis Rueden, Stephan Saalfeld, Benjamin Schmid, et al. Fiji: an open-source platform for biological-image analysis. *Nature methods*, 9(7):676–682, 2012.

[193] Eliot Dow, Adrian Jacobo, Sajjad Hossain, Kimberly Siletti, and Albert J Hudspeth. Connectomics of the zebrafish's lateral-line neuromast reveals wiring and miswiring in a simple microcircuit. *Elife*, 7:e33988, 2018.

[194] Adrian Wolny, Lorenzo Cerrone, Athul Vijayan, Rachele Tofanelli, Amaya Vilches Barro, Marion Louveaux, Christian Wenzl, Sören Strauss, David Wilson-Sánchez, Rena Lymbouridou, et al. Accurate and versatile 3d segmentation of plant tissues at cellular resolution. *Elife*, 9:e57613, 2020.

[195] Carsen Stringer, Tim Wang, Michalis Michaelos, and Marius Pachitariu. Cellpose: a generalist algorithm for cellular segmentation. *Nature methods*, 18(1):100–106, 2021.

[196] Jean-Yves Tinevez, Nick Perry, Johannes Schindelin, Genevieve M Hoopes, Gregory D Reynolds, Emmanuel Laplantine, Sebastian Y Bednarek, Spencer L Shorte, and Kevin W Eliceiri. Trackmate: An open and extensible platform for single-particle tracking. *Methods*, 115:80–90, 2017.

[197] Jordão Bragantini, Merlin Lange, and Loïc Royer. Large-scale multi-hypotheses cell tracking using ultrametric contours maps. In *European Conference on Computer Vision*, pages 36–54. Springer, 2025.

[198] Madeleine N Hewitt, Iván A Cruz, and David W Raible. Spherical harmonics analysis reveals cell shape-fate relationships in zebrafish lateral line neuromasts. *Development*, 151(2), 2024.

[199] Bo Huang, Hazen Babcock, and Xiaowei Zhuang. Breaking the diffraction barrier: super-resolution imaging of cells. *Cell*, 143(7):1047–1058, 2010.

[200] Jingjing Zhao, Xiaoping Yu, Xuping Shentu, and Danting Li. The application and development of electron microscopy for three-dimensional reconstruction in life science: a review. *Cell and Tissue Research*, 396(1):1–18, 2024.

[201] Mark E Lush, Daniel C Diaz, Nina Koenecke, Sungmin Baek, Helena Boldt, Madeleine K St Peter, Tatiana Gaitan-Escudero, Andres Romero-Carvajal, Elisabeth M Busch-Nentwich, Anoja G Perera, et al. scrna-seq reveals distinct stem cell populations that drive hair cell regeneration after loss of fgf and notch signaling. *Elife*, 8:e44431, 2019.

[202] Filip Vujovic, Neil Hunter, and Ramin M Farahani. Notch pathway: a bistable inducer of biological noise? *Cell Communication and Signaling*, 17:1–13, 2019.

[203] Carsten Beta and Karsten Kruse. Intracellular oscillations and waves. *Annual Review of Condensed Matter Physics*, 8(1):239–264, 2017.

[204] Chong Chen, Song Liu, Xia-qing Shi, Hugues Chaté, and Yilin Wu. Weak synchronization and large-scale collective oscillation in dense bacterial suspensions. *Nature*, 542(7640):210–214, 2017.

[205] Fernanda Pérez-Verdugo, Samuel Banks, and Shiladitya Banerjee. Excitable dynamics driven by mechanical feedback in biological tissues. *Communications Physics*, 7(1):167, 2024.

[206] K Vijay Kumar, Justin S Bois, Frank Jülicher, and Stephan W Grill. Pulsatory patterns in active fluids. *Physical Review Letters*, 112(20):208101, 2014.

[207] Paul Baconnier, Dor Shohat, C Hernández López, Corentin Coulais, Vincent Démery, Gustavo Düring, and Olivier Dauchot. Selective and collective actuation in active solids. *Nature Physics*, 18(10):1234–1239, 2022.

[208] Philipp J Albert and Ulrich S Schwarz. Modeling cell shape and dynamics on micropatterns. *Cell adhesion & migration*, 10(5):516–528, 2016.

[209] Ron Milo and Rob Phillips. *Cell biology by the numbers*. Garland Science, 2015.

[210] Nicolas Dray, Laure Mancini, Udi Binshtok, Felix Cheysson, Willy Supatto, Pierre Mahou, Sébastien Bedu, Sara Ortica, Emmanuel Than-Trong, Monika Krecsmarik, et al. Dynamic spatiotemporal coordination of neural stem cell fate decisions occurs through local feedback in the adult vertebrate brain. *Cell Stem Cell*, 28(8):1457–1472, 2021.

[211] Wolfram Research, Inc. Mathematica, Version 13.0, 2021. Champaign, IL, 2021.

[212] Annick Dhooge, Willy Govaerts, Yu A Kuznetsov, Hil Gaétan Ellart Meijer, and Bart Sautois. New features of the software matcont for bifurcation analysis of dynamical systems. *Mathematical and Computer Modelling of Dynamical Systems*, 14(2):147–175, 2008.

[213] The MathWorks Inc. Matlab version: (r2021a), 2021.

[214] Pauli Virtanen, Ralf Gommers, Travis E Oliphant, Matt Haberland, Tyler Reddy, David Cournapeau, Evgeni Burovski, Pearu Peterson, Warren Weckesser, Jonathan Bright, et al. Scipy 1.0: fundamental algorithms for scientific computing in python. *Nature methods*, 17(3):261–272, 2020.

Acknowledgements

I am profoundly grateful to Dr. Anna Erzberger for her unwavering support, mentorship, and guidance throughout my doctoral journey. Your advice, encouragement, and dedication have been invaluable to me, and I deeply appreciate the stimulating research environment that you cultivated. To anyone looking for a great mentor, I can only emphasize how fortunate I have been to have her as my supervisor.

A special thanks to Prof. Ulrich Schwarz for his continuous support before and throughout my PhD. I am grateful for your advice, dedicated time, and effort as a member of my thesis advisory committee.
I would also like to express my deep appreciation to Prof. Christine Selhuber-Unkel and Prof. Peer Fischer for their role in my thesis examination committee. Your time, effort, and evaluation of my work are sincerely appreciated.

I would like to thank my amazing collaborator Adrian Jacobo and all his lab members. Adrian, I truly enjoyed my visits to New York and San Francisco, and working with you has always been a great experience. I am also grateful to Jim Hudspeth for hosting me in his group for three months; it was a truly stimulating visit.

I am grateful to Nicoletta Petridou and Camilla Autorino for starting a collaboration with me. Nicoletta and Camilla, working with you was incredibly fulfilling, and I appreciate that you gave me the opportunity to contribute.

A big thank you to Shahar Kasirer and David Sprinzak for the many inspiring discussions that have shaped my work. I'm excited to see where our collaboration will lead us next.

A heartfelt thank you to my colleague Roman Belousov for sharing his knowledge and experience. It has been a lot of fun to work and collaborate with you. I truly value the many discussions that helped shape this thesis—from statistical mechanics and inference techniques to all the specialties of the Italian cuisine.

I am deeply thankful to Jan Rombouts, Jenna Elliott, Pamela Guruciaga and all other members of the Erzberger group for their camaraderie, assistance, and the collaborative spirit that made working in the lab both productive and very enjoyable. Your feedback during breaks, retreats, and group meetings has been truly valuable for my PhD, and having you as colleagues has made my time at EMBL an absolute pleasure. Also, a special mention to Camilo Andino Cappagli. It was a great privilege to start our PhD journey together.

I would like to thank Ergin Cohen Sagner—it was a great pleasure to supervise him during his master's thesis. I thank you, Ergin, for your dedication, curiosity, and willingness to engage with new ideas. You have been a fantastic student to work with, and I wish you all the best for your future endeavors.

I am grateful to Aissam Ikmi and Alexander Aulehla for their guidance and feedback as part of my thesis advisory committee. A special thank you to the head of my committee, Alba Diz-Muñoz. Your boundless energy and enthusiasm for science are truly inspiring.

I am deeply grateful to everyone who has contributed to my academic and personal growth during this doctoral journey, including all my EMBL friends and predoc batch colleagues. A special thanks to Artur Hahn, who has been a great friend and true source of inspiration for many years—I really hope that one day we will find a suitable project to pursue together. I also cherish my MolMed friends, whose encouragement and friendship mean a lot to me. I will always be thankful for you guys.

Finally, I want to thank my family for their support throughout my studies and PhD, through both the highs and the challenges. And thank you, Verena, for all the ways in which you have been there for me. Marrying you will always be the most cherished highlight of these years.